Downloaded from orbit.dtu.dk on: May 05, 2023

DTU Library

Graphitic Layer Encapsulated Iron Based Nonprecious Catalysts for the Oxygen Reduction Reaction

Zhong, Lijie

Publication date:
2016

Document Version
Publisher's PDF, also known as Version of record

Link back to DTU Orbit

Citation (APA):
Zhong, L. (2016). *Graphitic Layer Encapsulated Iron Based Nonprecious Catalysts for the Oxygen Reduction Reaction*. Department of Energy Conversion and Storage, Technical University of Denmark.

General rights
Copyright and moral rights for the publications made accessible in the public portal are retained by the authors and/or other copyright owners and it is a condition of accessing publications that users recognise and abide by the legal requirements associated with these rights.

- Users may download and print one copy of any publication from the public portal for the purpose of private study or research.
- You may not further distribute the material or use it for any profit-making activity or commercial gain
- You may freely distribute the URL identifying the publication in the public portal

If you believe that this document breaches copyright please contact us providing details, and we will remove access to the work immediately and investigate your claim.

Graphitic Layer Encapsulated Iron Based Non-precious Catalysts for the Oxygen Reduction Reaction

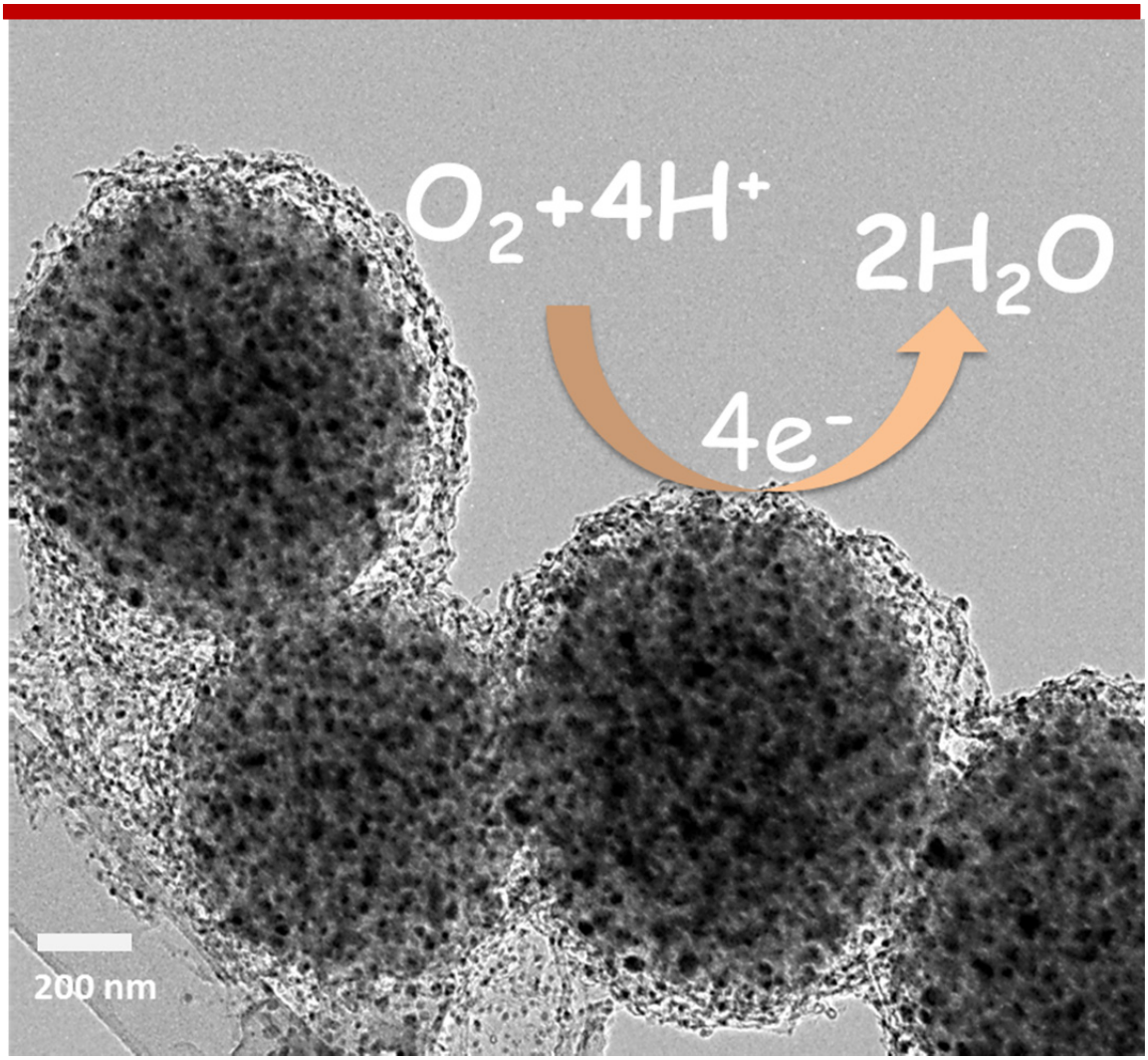

Lijie Zhong

December 2016

DTU Energy
Department of Energy Conversion and Storage

Graphitic Layer Encapsulated Iron Based Non-precious Catalysts for the Oxygen Reduction Reaction

A Ph.D thesis by

Lijie Zhong

Principal Supervisor:
Professor Qingfeng Li

Co-supervisors:
Professor Jens Oluf Jensen
Scientist Lars Nilausen Cleemann

Department of Energy Conversion and Storage

Technical University of Denmark

December 2016

Acknowledgments

This dissertation is submitted to the Technical University of Denmark (DTU) in partial fulfilment of the requirements for the degree of Ph.D. The work was carried out from January 2014 to December 2016 at Section of Proton Conductors, Department of Energy Conversion and Storage, DTU, with professor Qingfeng Li as the principal supervisor, professor Jens Oluf Jensen and Dr. Lars Nilausen Cleemann as co-supervisors, to whom my special thanks is first and foremost extended for giving me the opportunity for this Ph.D. study. It is their guidance, encouragement, and support that have paved the delighted way through this three-year project.

Professor Li has spent lots of his treasured hours in formal, as well as informal, discussions, from which I have learned the scientific disciplines and technical proficiencies of doing research. Professor Jensen has generously shared his critical yet instructive views to my ideas, plans, and results, always in a cheering way of his own style. Dr. Cleemann is always ready and available with his all-possible expertise for any help from experimental design to instrumental repairing. At the same time, I do enjoy a lot the plentiful freedom and trust my supervisors have given me even after many unsuccessful attempts.

My thanks is then going to the people I've been so privileged to work with in the proton conductor family – past and present, without whom my experience would never been so colorful and vibrant. In particular, I would like to thank our secretaries, Kirsten Munkgaard Thomsen and Lene Christensen, for helping me with all the administrative affairs, social activities in the group and nice chatting about cultures and lives in Denmark. Mikkel Rykær Kraglund, Andreas Kirkebæk, Arvind Kannan, Yang Hu, Hans Becker, Illia Shypunov, Benedikt Axel Brandes are thanked for sharing all kinds of sciences and the Ph.D. life together. I am very grateful to Tonny Søndergaard and Stine Søndergaard, who don't seem speaking much but always chatting wisely and helpfully. I will always remember the quiet and intense typing and reading hours we have spent together in room 042. I would like to thank Chao Pan, Claus Burke Mortensen, Steen Blichfeldt and Larisa Seerup for their help for all kinds of practical work in the laboratory. I am also very grateful to Jacob Sværke for his assistance with the synthesis of nitrogen free samples.

It has been my honor of working in a group with so many great scientists, Professor Niels J. Bjerrum, associate professor Irina Petrushina, Senior researcher Erik Christensen, Dr. Anton Vassiliev, Dr. David Aili and Dr. Aleksey Nikiforov. Thanks are due to them for their inspiration and help, in one way or another.

I am deeply indebted to Professor Cathrine Frandsen and Professor Steen Mørup, Department of Physics, DTU who have kindly introduced the Mössbauer spectroscopy to me and helped in doing

the measurements, graphs, calculations, and analysis, which provide the basis for the major findings of the present thesis research.

I am also grateful to Wilhelmus Huyzer, the Center for Electron Nanoscopy (CEN) at DTU, for his instruction during my training and use of transmission electron microscopy (TEM).

I thank my family and friends for being a part of my life, of whom I give my special appreciation to Shiyu Gan, who always believes in me and cheers me.

Finally, I would like to acknowledge Innovation Fund Denmark for the financial support within the framework of 4M center, which, after all, makes my thesis work possible.

Lijie Zhong

Kgs. Lyngby, Denmark

December 30th 2016

Abstract

Proton exchange membrane fuel cells (PEMFCs) are highly efficient energy conversion devices, which can be in combination with hydrogen fuel providing a clean energy technology to produce electricity. One crucial challenge for this technology is the large cathodic overpotential due to the sluggish oxygen reduction reaction (ORR) kinetics. Carbon supported platinum (Pt/C) is the state-of-the-art benchmarking catalyst for PEMFCs since it exhibits the highest activity. However, the high cost and low abundance of noble metals have limited large-scale commercialization of the technology. Current efforts are made to develop non-precious metal catalysts (NPMCs) as a replacement to the Pt/C electrocatalysts. In this thesis, a new type of NPMCs is synthesized by means of a dry autoclave with volatile ferrocene and cyanamide as precursors. The catalysts are morphologically featured by porous microspheres consisting of uniform metallic nanoparticles encapsulated in graphitic layers. The thesis work is conducted aiming at three major objectives: further optimization of the pyrolysis to achieve improved performance of catalysts, investigation of the complex Fe-containing components, and exploration of the possible active sites.

By systematic investigation of pyrolytic parameters i.e. temperature and duration, the best performance is achieved at 700 ^{o}C and 75 minutes, exhibiting a high catalytic activity in acid media (0.1 M $HClO_4$) with an onset potential of 0.85 V at 0.1 mA cm^{-2} and a mass specific kinetic current of 7.84 A g^{-1} at 0.7 V vs. RHE. A good stability with 25 mV potential losses after 10,000 cycles of potential scan between 0.6 and 1.0 V has also been demonstrated.

The featuring morphology of the catalysts, i.e. the porous microspheres consisting of the graphitic layer encapsulated metal-containing nanoparticles, is essentially maintained during the pyrolysis of varied durations and temperatures. The metal-containing nanoparticles showed changes in the iron phases and their contents, as characterized by ^{57}Fe Mössbauer spectroscopy. The iron containing components include reduced metals (α-Fe and γ-Fe), oxide (γ-Fe_2O_3), carbide (Fe_3C) as well as a minor paramagnetic component due to Fe^{3+} (high spin) and/or possibly Fe^{2+} (low spin), likely coordinated with nitrogen (FeN_x/C) as well identified for the Fe/N/C type catalysts in the literatures.

Quantitative determination of these metal containing components by low temperature ^{57}Mössbauer spectra shows that the content of the reduced metal component is steadily increasing with the pyrolytic time and temperature while the content of iron oxide is nearly constant. The most

interesting finding is that the Fe_3C content shows a peak in both the temperature-varying and the duration-varying series of samples. The possible FeN_x/C coordination phase, however, varies to a very limited extent for the studied samples.

The catalytic activities and mechanisms for ORR are evaluated by rotating disk electrode (RDE) and rotating ring-disk electrode (RRDE) voltammetry. In terms of the mass specific kinetic current density and half-wave potential, a strong correlation of the catalytic activity is established with the Fe_3C content within the entire composition range from 1.1 wt% to 4.5 wt% as well as with the FeN_x/C content in a narrow range from 0.5 wt% to 0.85 wt%. Other iron containing components, i.e. α-Fe, γ-Fe and Fe_2O_3, showed no association with the ORR activity. It is concluded that, for the present catalysts, the recognized encapsulated iron carbide is most likely contributing to the ORR catalysis, in addition to the well identified N-coordinated Fe species.

More evidences are found from the catalyst synthesized from nitrogen free precursors. This catalyst, consisting of only carbon encapsulated iron-based nanoparticles, shows some, though low, ORR activity, which is enhanced by the post heat treatment in an ammonia atmosphere, indicating the contribution of the nitrogen functionalities**.**

Two anions in the electrolyte are used to probe the iron containing active sites towards the ORR, cyanide (CN^-) in alkaline and thiocyanate (SCN^-) in acidic medium, which seem supporting the above conclusions. These findings provide new insights to the encapsulation structure of Fe based nanocatalysts and therefore options for further development of NPMCs.

Table of Contents

List of abbreviations

CV	Cyclic Voltammetry
CE	Counter Electrode
CNTs	Carbon Nanotubes
CoPc	Cobalt phthalocyanine
DFT	Density Functional Theory
DOE	Department of Energy, U.S
FePc	Iron phthalocyanine
GCE	Glassy Carbon Electrode
HR	High Resolution
MEA	Membrane Electrode Assembly
MOF	Metal Organic Framework
MN_x/C	Metal-nitrogen Carbon
NPMCs	Non-precious Metal Catalysts
NPs	Nanoparticles
OCP	Open Circuit Potential
ORR	Oxygen Reduction Reaction
LSV	Linear Sweep Voltammetry
PANI	Polyaniline
PEM	Proton Exchange Membrane
PEMFC	Proton Exchange Membrane Fuel Cell
RDE	Rotating Disk Electrode
RHE	Reversible Hydrogen Electrode
rpm	Revolutions Per Minute
RRDE	Rotating Ring Disk Electrode
RE	Reference Electrode
SEM	Scanning Electron Microscope
SCE	Saturated Calomel Electrode
TEM	Transmission Electron Microscopy
WE	Working Electrode
XRD	X-ray Diffraction
XPS	X-ray Photoelectron Spectroscopy

Chapter 1

Introduction

This chapter starts with a brief introduction to the principle and technology of fuel cells particularly proton exchange membrane fuel cells (PEMFCs). Catalysts for the oxygen reduction reaction (ORR) as the key materials are then discussed under categories of supported platinum and its alloys and non-precious metal catalysts (NPMCs). The NPMCs are the focus of the thesis and reviewed in details. An overview of this dissertation is given at the end of the chapter.

1.1. Fuel Cell Technology

One of the urgent problems the human being has to face today is the environmental challenge and the rapidly increasing demand for energy. Fossil fuels i.e. coal, oil, and natural gas, are the world primary energy source so far. Yet it is a type of finite resources and produces irreparably harm to the environment. Replacement of fossil fuels by clean energy resources such as biomass, wind, and solar energy would be the long-term solution. Hydrogen and its combination with electrochemical energy conversion devices i.e. fuel cells and electrolysers have the potential to provide a reliable, secure and clean energy technology.

Fuel cell is an electrochemical device that directly converts chemical energy from fuels (e.g. hydrogen) into electricity. It is an ideal device in views of the high energy conversion efficiency and little release of air pollutants other than the byproduct water, compared to the present fossil fuel based power technologies for both stationary power plants and automobile applications. It is also environmentally sustainable by assuming that hydrogen as an energy carrier is potentially produced from the renewable electricity.

1.1.1. A Brief History

Main historic events of the fuel cell development are shown in **Figure 1**. The electrochemical principle for the water electrolysis (a reverse process regarding to the fuel cell) was demonstrated in more than 200 years ago by Humphry Davy. The German-Swiss chemist Christian Friedrich Schönbein and the Welsh scientist William Robert Grove invented the first so called gas batteries in 1838 and 1839, which were formally named the fuel cell in 1889s by Charles Langer and Ludwig Mond. The early milestones are marked by General Electric´s invention of proton exchange membrane fuel cells (PEMFCs), Francis Bacon´s demonstration of alkaline stacks, and the application in the manned space vehicles by the US National Aeronautics and Space Administration (NASA) agency in 1930-60s. These remarkable activities have promoted the research, particularly during and after the first oil crisis in 1970s. In the last 20 years, great progress has been made and the technology is gradually transformed from military to various civil applications for both stationary and automobile areas.

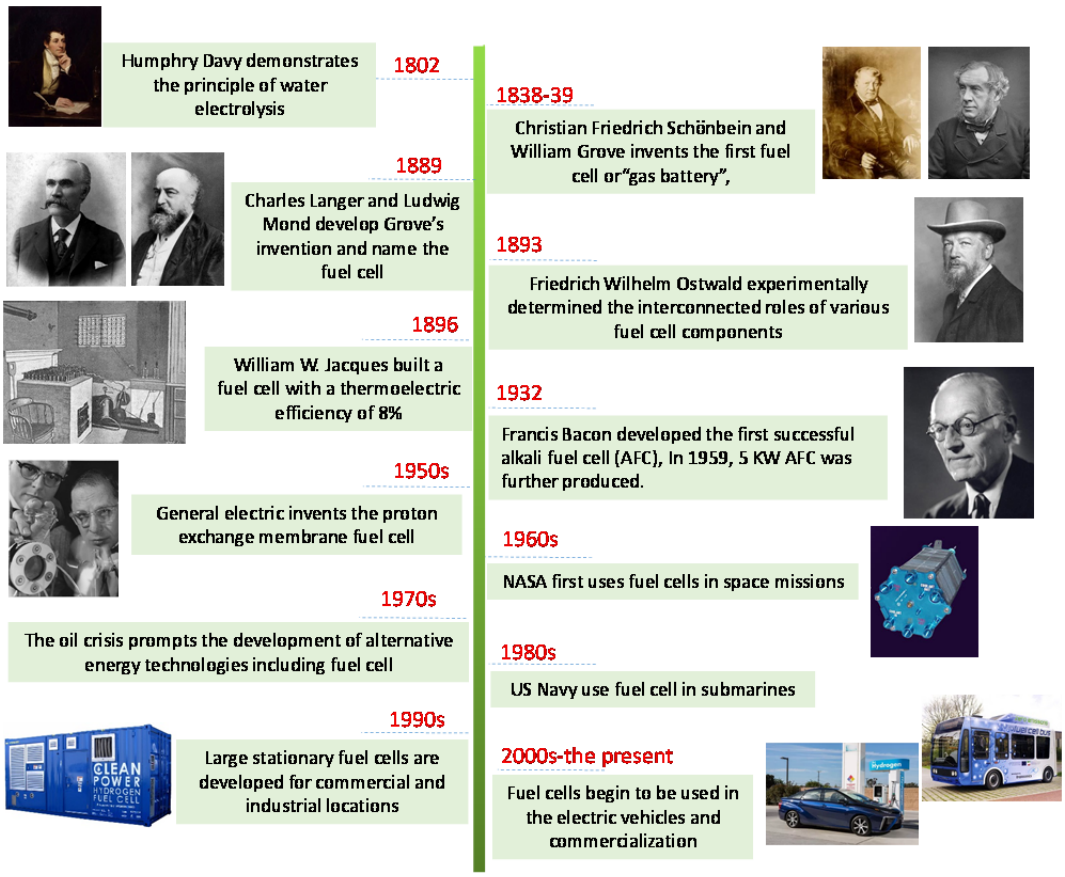

Figure 1. The historic events for the development of fuel cells.

To date, five major types of fuel cells have been developed classified according to the used electrolyte, i.e. PEMFCs, alkaline fuel cells (AFC), phosphoric acid fuel cells (PAFC), molten carbonate fuel cells (MCFC) and solid oxide fuel cells (SOFC), as summarized in **Table 1.**

Table 1. Types of fuel cells and their technical features of operation

Fuel cell types	**PEMFC**	**AFC**	**PAFC**	**MCFC**	**SOFC**
Electrolyte	Ion exchange membranes	Immobilized or mobilized KOH	Immobilized liquid H_3PO_4	Immobilized molten carbonates	Ceramics
Temperatures	80 °C	65-200 °C	190-200 °C	650 °C	800-1000 °C
Charge carrier	H_3O^+	OH^-	H^+	CO_3^{2-}	O^{2-}
External reforming	Yes	Yes	Yes	No	No
Cell construction	Carbon-based	Carbon-based	Carbon-based	Stainless steel	Ceramics
Catalysts	Pt	Ni, Ag, Pt	Pt	Ni/NiO	Perovskites/Ni
Heat management	Process gas; independent cooling	Process gas; electrolyte circulation	Process gas; independent cooling	Internal reforming; Process gas	Internal reforming; Process gas

1.1.2. Principle of Proton Exchange Membrane Fuel Cells (PEMFCs)

As the main focus of the present thesis, PEMFCs are briefly explained, as schematically shown in **Figure 2.** A proton exchange membrane is typically based on perfluorosulfonic acid for operation below 100 ^oC or phosphoric acid doped polybenzimidazole membranes for operation above 100 ^oC. The conducting charge carriers are protons either in hydrated (e.g. H_3O^+) or its bare (H^+) form. On each side of the electrolyte membrane are attached gas diffusion electrodes, one being anode and the other cathode. The electrodes consist of a porous substrate called gas diffusion layers, onto which a catalyst layer was applied. Between the gas diffusion layer and the catalyst layer, there is often a transition supporting layer called microporous layer (**Figure 2**b).

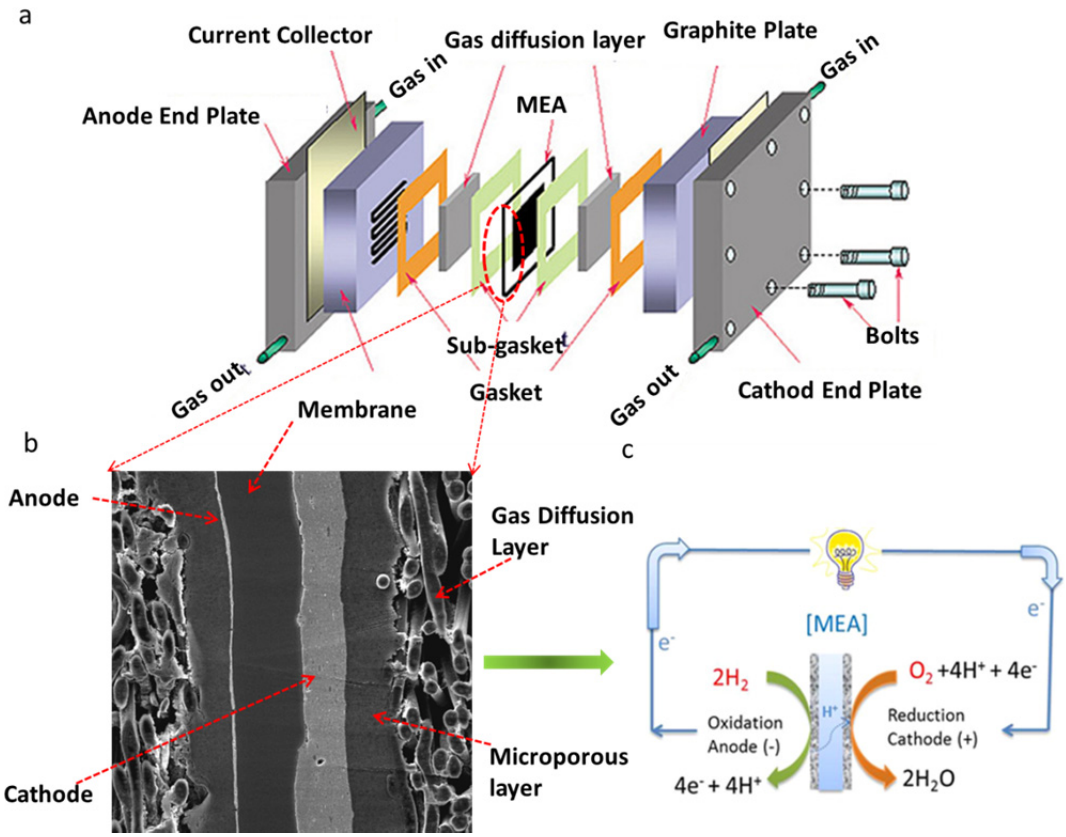

Figure 2. Schematic representation of the PEMFC. (a) An exploded view of a PEMFC with all components marked. (b) Scanning electron microscopy (SEM) images of a membrane-electrode-assembly (MEA) section. (c) Electrochemical reaction process of PEMFC at anode and cathode.

At the anode side hydrogen as fuel is supplied and the half-cell reaction is (shown as **Figure 2**c)

$$2H_2(g) \rightarrow 4H^+_{(anode)} + 4e^- \quad (1)$$

And at the cathode oxygen, often air instead, is supplied and the half-cell reaction is

$$O_2(g) + 4H^+_{(cathode)} + 4e^- \rightarrow 2H_2O\ (l) \quad (2)$$

Through the electrolyte, protons are transported from the anode to the cathode:

$$4H^+_{(anode)} \rightarrow 4H^+_{(cathode)} \quad (3)$$

While the electrons travel through an external circuit, the overall reaction is therefore

$$2H_2 + O_2 = 2H_2O + \text{heat} + \text{electricity} \quad (4)$$

1.2. The Oxygen Reduction Reaction (ORR)

Electrocatalytic oxygen reduction reaction (ORR) at the cathode is kinetically slow. As a comparison, the exchange current density of hydrogen oxidation on platinum is about 1 mA cm^{-2} (H_2) while that of oxygen reduction reaction is about 10^{-3} mA cm^{-2}, which can be translated into a polarization loss of ca. 10 mV at the anode and over 400 mV at the cathode under practical operating current densities[1].

As a primary reaction of PEMFCs, the overall ORR may proceed via two mechanistic paths, i.e. a direct $4e^-$ (four electron) pathway or a two-step $2e^-$ pathway in association with H_2O_2 production (**Figure 3**a). The mechanism for the ORR is very complex and the intermediates during are in fact dependent on different catalytic materials, electrolytes and applied potentials.

The first mechanism is the preferred dissociative pathway followed by a concerted 'four electron' transfer process leading to the direct formation of water (**Figure 3**b). First the molecular oxygen is adsorbed onto the metal surface and the O=O double bond breaks to give adsorbed oxygen atoms (O*, here * is a surface site of the catalyst):

$$O_2 + * \rightarrow 2O* \quad (5)$$

The single oxygen atoms are then reacting with protons and reduced to give surface bound hydroxyl (OH*) groups

$$2O* + 2H^+ + 2e^- \rightarrow 2OH* \quad (6)$$

The surface bound OH* is further reacting with protons and electrons to give water which then leaves the metal surface and release the catalyst surface site *

$$2OH* + 2H^+ + 2e^- \rightarrow 2H_2O + * \quad (7)$$

The overall reaction is then a direct $4e^-$ transfer process:

$$O_2 + 4H^+ + 4e^- \rightarrow 2H_2O \qquad E^0 = 1.23 \text{ V vs RHE} \quad (8)$$

The $2e^-$ transfer mechanism involves the formation of hydrogen peroxide, which prefers an associated pathway (**Figure 3c**). First of all, the adsorption of the molecular oxygen on the metal surface does not lead to breaking up the O=O double bond:

$$O_2 + * \rightarrow 2O_2* \quad (9)$$

The associative oxygen atoms are then reduced by two electrons with the formation of well identified hydrogen peroxide, which might be desorbed from the surface:

$$O_2* + 2H^+ + 2e^- \rightarrow H_2O_2* \rightarrow H_2O_2 + * \quad E^0 = 0.68 \text{ V vs RHE} \tag{10}$$

The formed hydrogen peroxide may be further reduced to water according to the following equation:

$$H_2O_2 + 2H^+ + 2e^- \rightarrow 2H_2O \qquad E^0 = 1.78 \text{ V vs RHE} \tag{11}$$

In brief, the direct $4e^-$ oxygen reduction path is much more efficient than the 2e- reduction pathway.

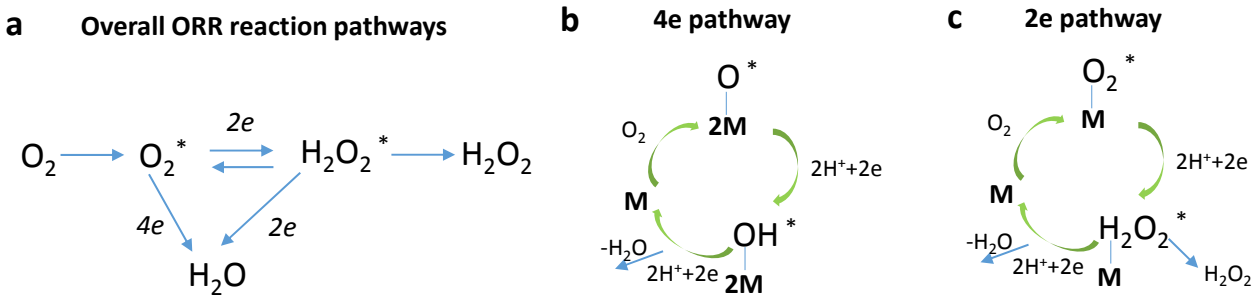

Figure 3. ORR reaction mechanisms. (a) Overall ORR reaction pathways. (b) One example of preferred dissociative 4e pathway ORR mechanism. (c) One example of preferred associative 2e pathway ORR mechanism.

1.3. ORR Catalysts Based on Precious Metals

The most effective way to improve the slow ORR kinetics is by using electrocatalysts. Numerous electrocatalysts have been developed for the ORR, which can be generally divided into two main categories, *precious metal based and non-precious metal based*[2]. The state-of-the-art PEMFC catalysts are carbon supported platinum nanoparticles, as shown in the TEM images in **Figure 4**.

1.3.1. State-of-the-art Pt/C Catalysts

Compared to the early year catalysts based on metal blacks, the carbon support is a key factor to achieving the high degree dispersion of nanoparticles and therefore a reduced metal loading and cost with an enhanced ORR activity. High surface area carbon blacks, e.g. Vulcan XC-72 (Cabot

Corporation) with a surface area of 250 $m^2 \cdot g^{-1}$ are the most widely used supports. Significant progress in developing catalyst supports has been achieved as well reviewed[3,4].

Commercial Pt/C catalyst products are available with the platinum content from 10 wt% to over 60 wt%. The size of platinum nanoparticles (PtNPs) is typically in the range of 2-5 nm (**Figure 4**). For a general operating PEMFC, the loading of platinum on the electrodes is about 0.4-0.8 $mg_{(Pt)}$ cm^{-2}. The Department of Energy (DOE), US, has set targets of 0.125 mg cm^{-2} for 2020. At this loading, the best PEMFC may achieve a power density of 0.75 W cm^{-2} e.g. a cell voltage of 0.75 V at a current density of 1 A cm^{-2}. Under these assumptions, the metal consumption can be estimated to about 0.19 g kW^{-1}. This counts for 53% MEA cost, 35% stack cost and 17% system cost[5].

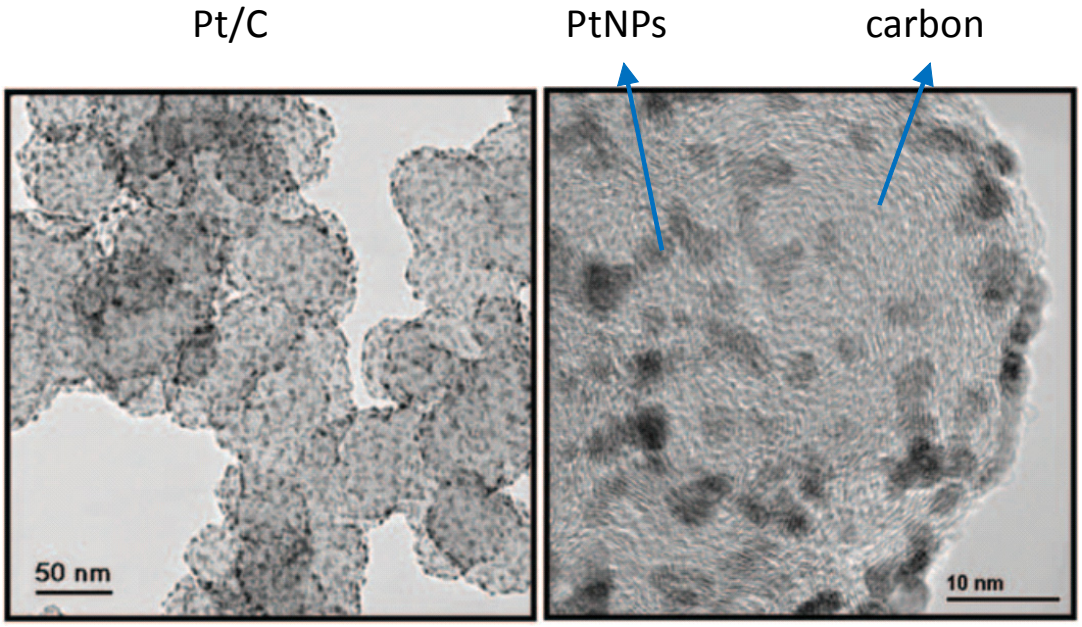

Figure 4. Representative TEM images of carbon supported platinum nanocatalysts[1] (Pt/C, 40%).

In addition to cost and performance, long-term stability of platinum-based catalysts is another issue. Towards the fuel cell lifetime targets of 5,000 h for automotive and 40,000 h for stationary applications, the catalyst degradation is a major challenge. Sintering of platinum particles, dissolution of platinum, and corrosion of the carbon support are the main mechanisms. The sintering of platinum particles on the carbon support decreases catalytically active surface areas. Small metal particles of the catalyst may dissolve into the acidic electrolyte, precipitating onto larger metal particles and thus leading to particle growth, the so-called Ostwald effect. The particles may also directly coalesce with each other due to movement on the carbon surface.

In brief, maximizing the mass specific activity and therefore lowering the Pt usage as well as improving the stability are the major issues for developing Pt-based materials.

1.3.2. Platinum Alloys with Late Transition Metals

In the early 1980s, researchers first invented that Pt-alloys are superior in catalysis for the ORR. Since then various late transition metals have been used for alloying Pt, as well summarized by Wang et al[6]. Among others, alloys of Co, Ni, and Fe exhibit superior activities. One concern is the instability of these alloying elements, which may be dissolved during fuel cell operation. With proper post treatment by e.g. acid washing, both better activity and durability of Pt alloy catalysts was achieved[7].

1.3.3. Platinum Alloys with Early Transition and Rare Earth Metals

In recent years, more research has been carried out to platinum alloys with early transition metals and rare earth metals. Based on the reported experimental results and theoretical calculations, a volcano plot has been proposed to predict the ORR activity of Pt-alloy materials[8] (**Figure 5**a).

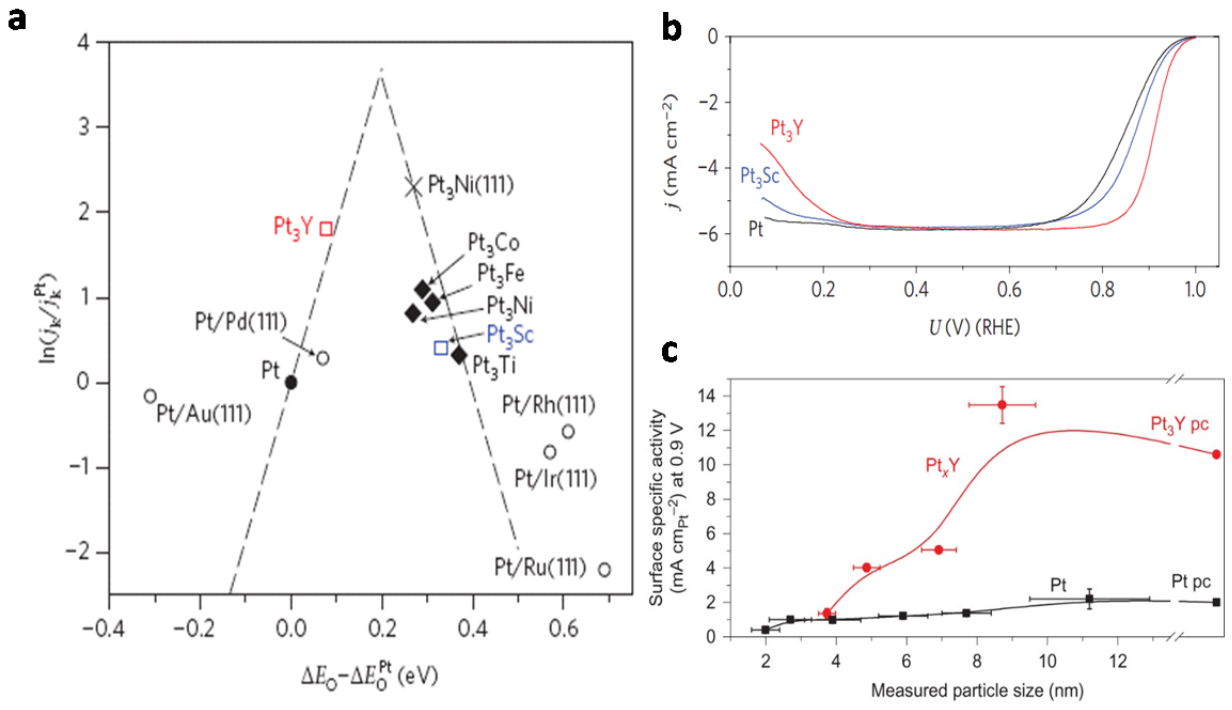

Figure 5. Pt-alloys with early transition metals. (a) A volcano plot for ORR on various Pt-based alloy catalysts[8]. The X-axis represents the oxygen binding energy on different catalysts vs that on Pt. The dashed line is the theoretical prediction. (b) Experimental ORR polarized curves for Pt_3Y, Pt_3Sc, and Pt synthesized by sputtering. (c) ORR performances of size-dependent Pt_3Y nanoparticles[9].

From the prediction, Pt_3Y on one side, and the single-crystal Pt_3Ni (111) on the other seem the best electrocatalysts in term of high activity. By physical sputtering, the prepared Pt_3Y indeed

exhibited very high activity (**Figure 5**b) and size dependence[9] (the optimized size is ca. 10 nm) (**Figure 5**c). Lim et. al. also used a complex high-pressure radio frequency magnetron co-sputtering technique to prepare nanostructured Pt_3Y nanoparticle (10-12 nm), which exhibited 16-times enhancement in specific activity compared with that of pure Pt thin film electrode[10].

Very recently, Chorkendorff's group prepared a series of rare earth metal–Pt alloys for the ORR studies[11] (**Figure 6**). Among eight rare earth metal elements, Pt_5Tb shows the highest activities (**Figure 6**a) and a scaling relationship between lattice parameter and activity was observed (**Figure 6**b). Although the catalytic activity is well demonstrated for these Pt alloys, the chemical synthesis of the supported catalysts for fuel cell evaluation has been a challenge. More simple and commercially suitable methods should be further developed for scale-up production of e.g. Pt_3Y and Pt_5Gd catalysts.

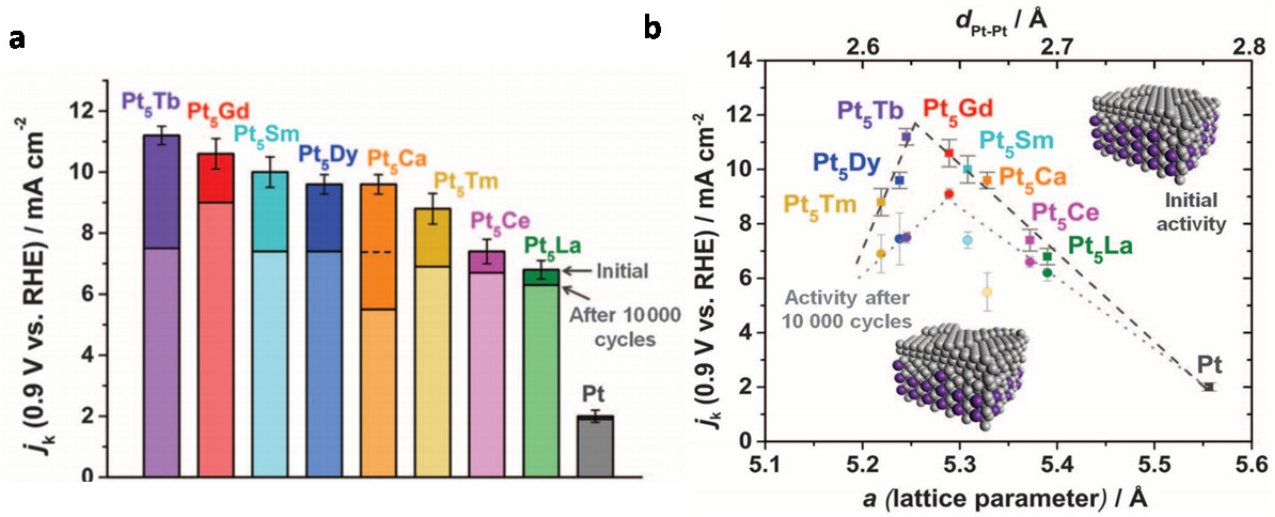

Figure 6. Pt-alloys with rare-earth transition metals[11]. (a) ORR kinetic current densities of various Pt-rare earth metal alloys in 0.1 M $HClO_4$. (b) Scaling relations between ORR activity of various Pt-rare earth metals and the lattice parameter (bottom)/bulk d_{Pt-Pt} (top).

1.3.4. Nanostructured Pt-M Catalysts

With the rapid development of nanotechnologies, various nanostructured Pt-alloys have been prepared with aims to improving both activity and stability of the Pt alloy catalysts. A few recent breakthroughs are briefly discussed here. Yang and co-workers reported a series of shape controlled Pt-M alloys (M = Co, Fe, Ni, Pd) through one-step reduction of Pt and transition metal salts by CO[12] (**Figure 7**). The resulting nano-catalysts possesses well-defined morphologies, typically in

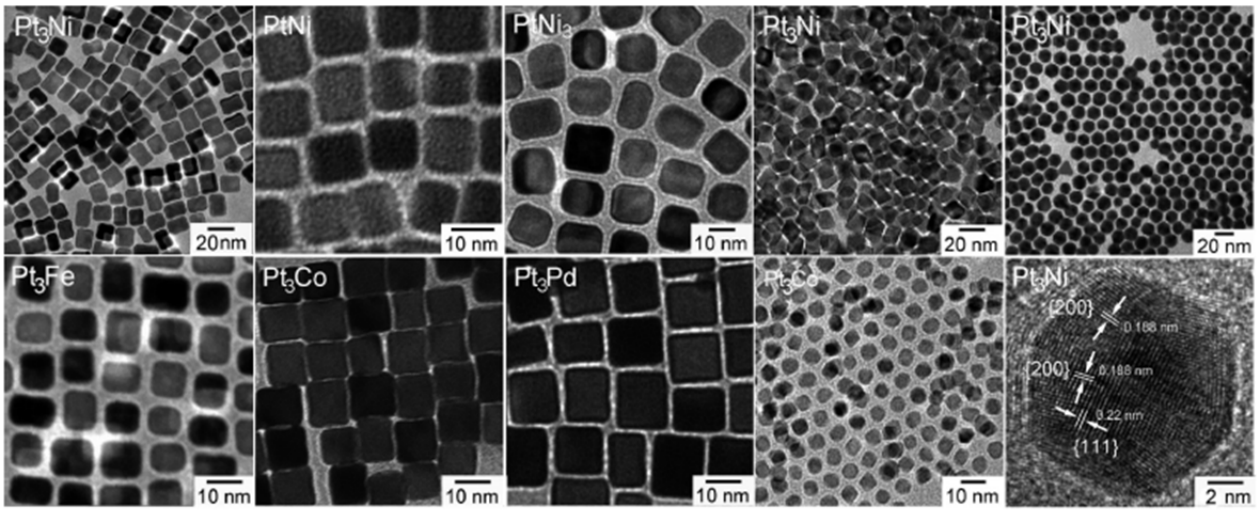

Figure 7. Nanostructured Pt-M alloys[12]. TEM images of various nanostructured Pt-M alloys.

cubic and octahedral shapes (**Figure 7**). The representative Pt_3Ni in both nanostructures disclosed the mass and specific activities higher than those of the conventionally prepared Pt/C.

In 2014, Stamenkovic and Yang et. al. prepared a nano-frame structure of Pt_3Ni (**Figure 8**a) by chemical synthesis[13]. This Pt_3Ni catalyst exhibited 5.7 A $mg^{-1}_{(Pt)}$ in mass activity (0.9 V, **Table 2**) and extremely good stability for more than 10, 000 cycles. This high activity was attributed to the unique open-framework nanostructure and the existence of highly-active crystalline Pt_3Ni (111). Further, Mueller and Huang et. al. in 2015 reported the transition metal-doped Pt_3Ni octahedral [14] in which Mo-Pt_3Ni, broken the ORR activity records with an area specific activity of up to 10.3 mA cm^{-2} and a mass activity of 6.98 A $mg^{-1}_{(Pt)}$ (**Figure 8**b and **Table 2**).

Very recently, the Pt activity was remarkably improved by preparation of the jagged Pt nanowires[15] (**Figure 8**c), which exhibited the currently best performances with a specific activity of 11.5 mA cm^{-2} and a mass activity of 13.6 A $mg^{-1}_{(Pt)}$. It is suggested that this twisted structure produces high stress in the nanowires, resulting in rich under-coordinated active Pt surface as the origin of such a high activity.

Table 2 summarizes the performances of these three record-keeping catalysts compared with the typical performance of conventionally prepared carbon supported platinum nanoparticle catalysts and the DOE 2017/2020 target (0.44 A mg^{-1} Pt).

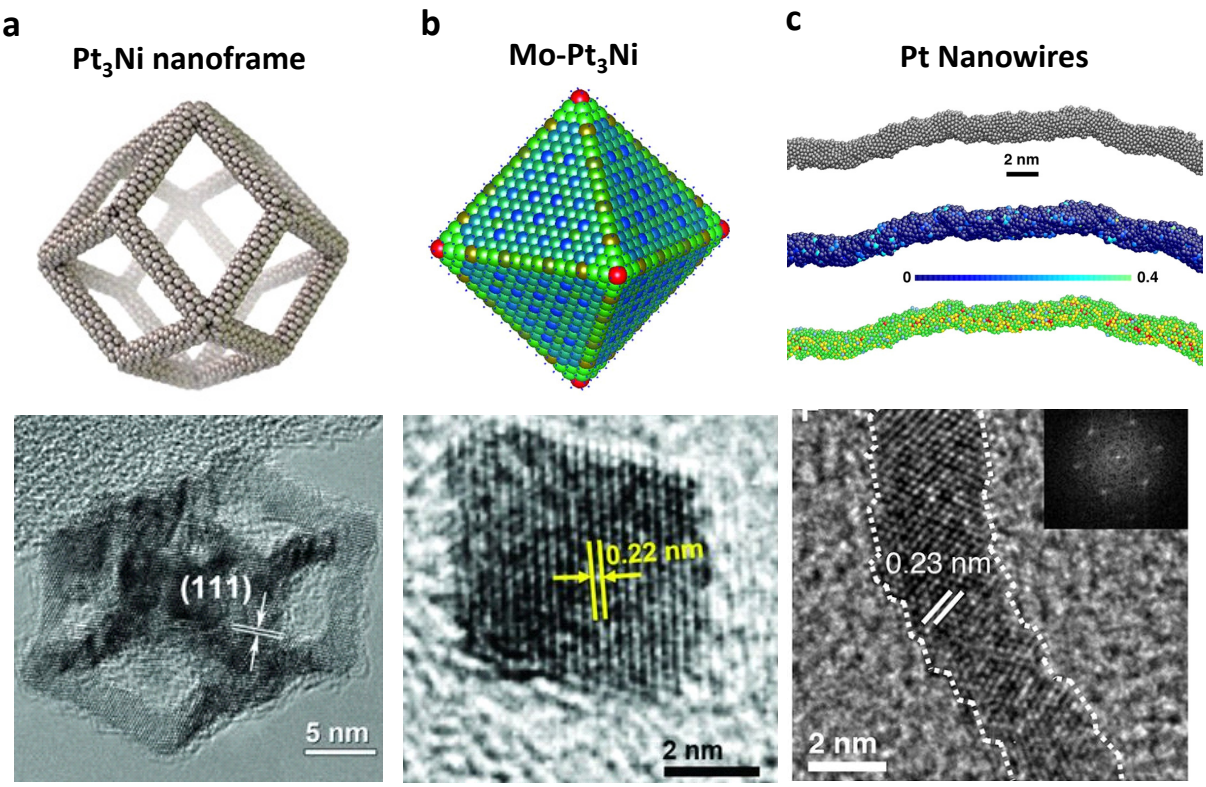

Figure 8. Novel nanostructures Pt-based ORR catalysts that are showing the best performance (a) Pt_3Ni nanoframes[13], (b) Mo doped Pt_3Ni[14] and (c) Jagged Pt nanowires[15].

Table 2. The record-keeping performances of Pt-based catalysts as shown in Figure 8.

Catalysts	Specific activity ($mA\ cm^{-2}$) at 0.9 V	Mass activity ($A\ mg^{-1}_{Pt}$) at 0.9 V	Ref.
Pt/C	0.35	0.26	[15]
Nanoframe Pt_3Ni/C	NA	5.7	[13]
Mo-Pt_3Ni/C	10.3	6.98	[14]
Jagges Pt nanowires/C	11.5	13.6	[15]
DOE target (2017)	NA	0.44	[5]

1.4. Non-precious Metals and Metal-free ORR Catalysts

1.4.1. Overall Status

Extensive efforts have been made to develop non-precious metal catalysts (NPMCs)[16-22] and even metal-free catalysts[23-28] for PEMFCs. The most promising materials investigated thus far are transition metal-nitrogen-carbon composites MN_x/C (M = Co, Fe, Ni, etc.) formed by the pyrolysis

of a variety of metal, nitrogen and carbon precursors. Other interesting materials include metal-free such as nitrogen-doped carbon materials, metal oxides/carbides, metal chalcogenides and so on. Among these candidate materials, the MN_x/C catalysts are of most interest. The state of the art performance based on MN_x/C catalysts matches that of Pt/C at cell voltages above 0.9 V, though the NPMCs loading is higher than that of Pt/C. At high current densities or lower cell voltages (0.8 V), the reported microporous carbon-supported iron based catalysts[29] by Dodelet et. al., in 2009 was up to a volumetric current density of 99 A cm^{-3} **(Table 3),** which is close to meet the U.S. DOE 2010 target of 130 A cm^{-3} (**Table 3**). In 2011, this group further increased the value up to 230 A cm^{-3} by replacement of BP2000 carbon with ZIF-8 for producing carbon supported Fe-based catalysts[30]. The recent breakthrough for FeN_x/C sites on carbon nanotube/porphyrin carbon (Fe/PC/CNT) catalysts[31] shows the performance of 320 A cm^{-3} **(Table 3)**, which exceeds the newly updated 2017/2020 target of 300 A cm^{-3} corresponding to 23% of the reference Pt/C performance[7]. Several representative works will be further described in the following section.

Table 3. State-of-the-art NPMCs for ORR and PEMFC.

Catalysts	Specific activity (mA cm^{-2}) at 0.8 V	Volume *j* (PEMFC) (A cm^{-3}) at 0.8 V	Ref.
Fe/Phen/BP	NA	99	[29]
PANI/Fe/C	4.2	NA	[32]
Fe/Phen/ZIF-8	NA	230	[30]
Fe/PC/CNT	4.5	320	[31]
DOE target (2017)	NA	300	[5]

1.4.2. MNx/C Type Catalysts

Among non-precious metal ORR catalysts, the most promising class is carbon-supported transition metal/nitrogen (MN_x/C) materials (M = Co, Fe, Ni). Since the thesis is based on this type of the ORR catalysts, more detailed discussion is made as followed.

1.4.2.1. Early Year Work

In 1964 Jasinski first discovered that cobalt phthalocyanine (CoPc)[33] could catalyze ORR in alkaline media (**Figure** 9a). This historical finding opens an avenue for the development of NPMCs.

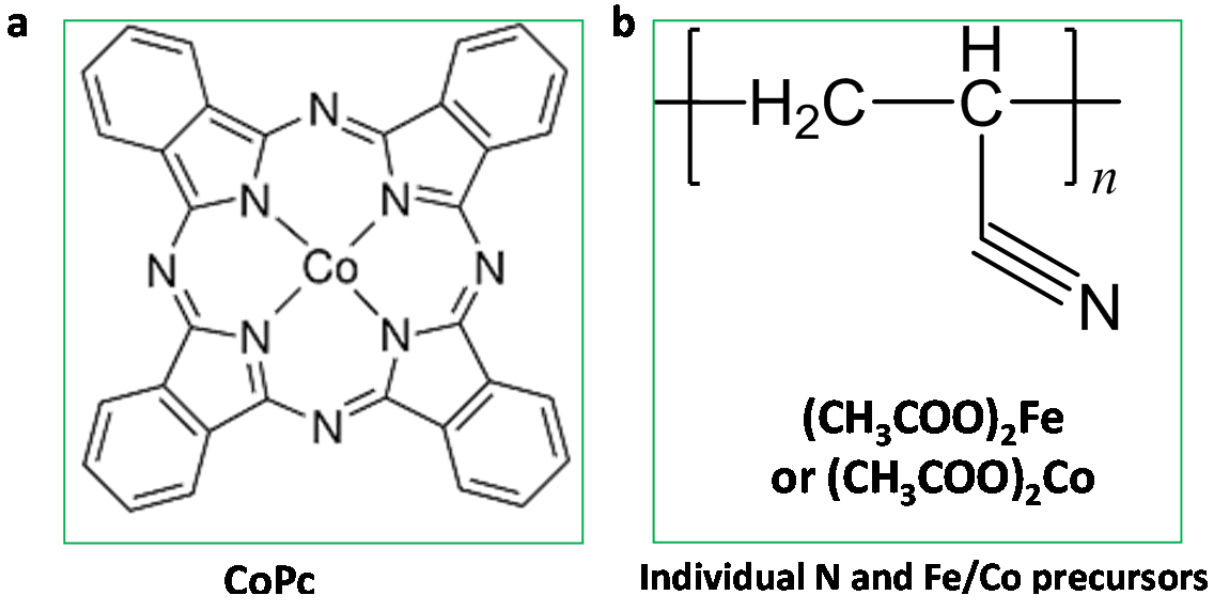

Figure 9. (a) Molecular structure of CoPc (the first NPMC)[33]. (b) MN_x/C catalyst was produced by pyrolysis of individual mixed N/C and Fe or Co resources[36].

A critical concern of the early-year research is the stability of the macrocyclic molecules, especially in the acidic electrolyte. A large portion of the ORR activity was found to be lost after the first cycle of the cycle voltammetric measurement[34]. An early breakthrough was achieved by using the high-temperature treatment. The resulted catalysts were found to have remarkable improvements on the stability as well as the activity[35]. One of the possible explanations is that some new active sites are created during the high-temperature pyrolysis.

Another valuable finding was that the expensive transition metal macrocycles are shown not necessary. The catalytically active $M–N_x/C$ moieties could, in fact, be formed from a great variety of different precursor materials that are containing metal, nitrogen, and carbon, as verified by Yearger and coworkers in 1989 when they prepared active catalysts from polyacrylonitrile, Fe salts, and VulcanXC-72 carbon as the carbon black support (**Figure 9**b)[36]. Since then, different types of coordinated transition metal catalysts have been investigated[37,38]. We will highlight a few recent breakthroughs in the following section.

1.4.2.2. Breakthroughs of MNx/C Type Catalysts

There are a few milestones in recent years about the development of MN_x/C catalysts. Dodelet and coworkers in 2009 reported a remarkable progress with microporous carbon supported Fe-based catalyst[29] (**Figure 10**a, and the schematic structure shown in the inset of **Figure 10**c). On the basis of their previous work, the authors identified four crucial factors for Fe-N-C catalysts: (i) disordered

carbon content in the catalyst precursor; (ii) iron; (iii) surface nitrogen, and (iv) micropores. Considering these four factors, the author proposed a two-step pyrolysis strategy including micropore produced on the carbon surface in the first step and pore filled by N and Fe in the second step. The final resulted catalyst was expected to form a similar Fe-N_4 active structure (the inset of **Figure 10**c).

Cobalt or iron phthalocyanine (FePc or CoPc) as we discussed in the beginning of this section is highly ORR active organic materials but shows poor stability owing to the metal oxidation or loss by produced small content of H_2O_2. This paper provides a good idea of synthesizing FeN_4 structure-like FeN_x/C catalyst through pore production and filtration. Unfortunately, the stability remained a challenge with ca. 56% reduced after 100 h-running (the initial current of 0.75 A cm^{-2} at 0.5 V was decreased to 0.33 A cm^{-2}).

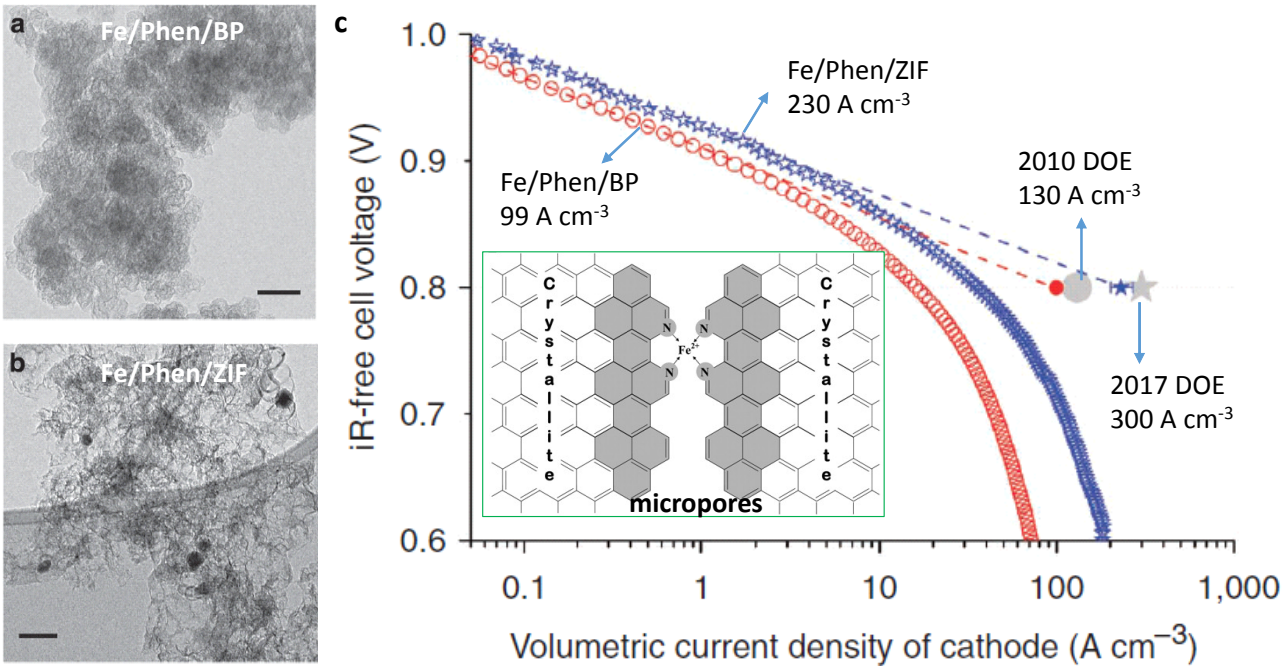

Figure 10. Fe-based catalysts supported on microporous carbon (Fe/MC) for PEMFC[29,30]. (a, b) TEM images of two types of Fe/MC including (a) Fe/Phen/BP (by pyrolysis of Fe precursor, Phen pore filter, and microporous carbon support of heat-treated BP2000) and (b) Fe/Phen/ZIF (by pyrolysis of Fe precursor, Phen pore filter, and ZIF8 carbon support). Scale bars: 50 nm. (b) PEMFC tests (H_2-O_2) and comparison with DOE targets.

The group in 2011 further optimized this type of catalysts to obtain a more porous Fe based catalyst (Fe/Phen/ZIF)[30] by using the MOF carbon support of ZIF8 instead of the previously used BP2000(**Figure 10**b). This catalyst exhibited the estimated volumetric current density as high as

230 A cm^{-3} at 0.8 V. (**Figure 10**c, blue circle). The long-term stability has also been improved with only 15% degradation observed during the 100h H_2-air fuel cell test but still requires more efforts for satisfying the commercial applications.

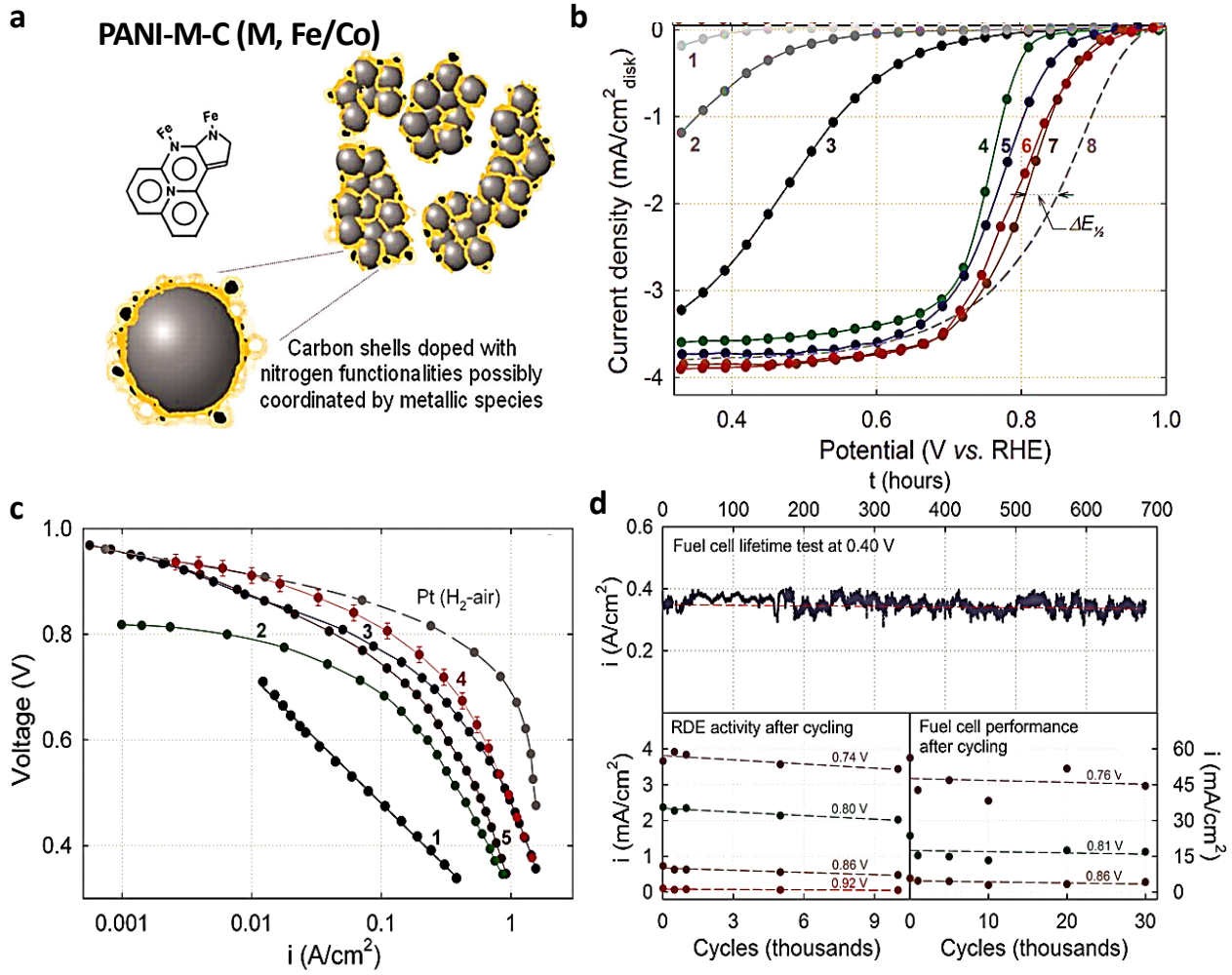

Figure 11. PANI-M-C catalyst[32]. (a) A schematic illustration of the preparation of PANI-M-C catalyst including four steps: mixing carbon, aniline oligomers and metal precursors, oxidation polymerization, heat treatment in N_2 and acid leaching. (b) ORR polarization curves in 0.5 M H_2SO_4 (0.1 M $HClO_4$ for Pt/C reference) at various samples, (1) carbon black, (2) heated-carbon black, (3) heated PANI-C, (4) PANI-Co-C, (5) PANI-FeCo-C1 (Mixing of Fe/Co precursor simultaneously), (6) PANI-FeCo-C2 (Fe/Co deposition separately) (7) PANI-Fe-C, (8) Pt/C (20 µg Pt cm^{-2}). (c) H_2-O_2 fuel cell polarization curves, (1) PANI-C, (2) PANI-Co-C, (3) PANI-FeCo-C1, (4) PANI-FeCo-C2, (5) PANI-Fe-C and reference Pt/C. (d) Durability test of PANI-FeCo-C catalyst at 0.4 V and corresponding RDE and fuel cell tests after cycling.

Another breakthrough was achieved by Zelenay and coworkers in the same year of 2011. They developed a high-performance PANI-M-C (M, Fe and/or Co) catalysts derived from polyaniline, iron and cobalt salt [32]. Four rationally designed steps were proposed to prepare this catalyst including aniline oligomer modification of carbon, oxidation polymerization, twice heat treatments and acid leaching (**Figure 11**a). The ORR performances represent the best values at present with the onset potential of 0.93 V and the half-wave potential of 0.81 V, only ca. 40 mV lower than that of Pt/C. (**Figure 11**b). The performance of assembled H_2-O_2 fuel cell is also very close to that for the Pt/C with a current density of ~1 A cm^{-2} at 0.5 V. Meanwhile, the durability is also satisfactory for the testing period of more than 700 h at 0.4 V (**Figure 11**d). It is noted that, in their work, carbon was pre-modified by the aniline oligomer. This process is believed to improve the dispersion of carbon particles and therefore promote the next step of oxidation polymerization between carbon nanoparticles.

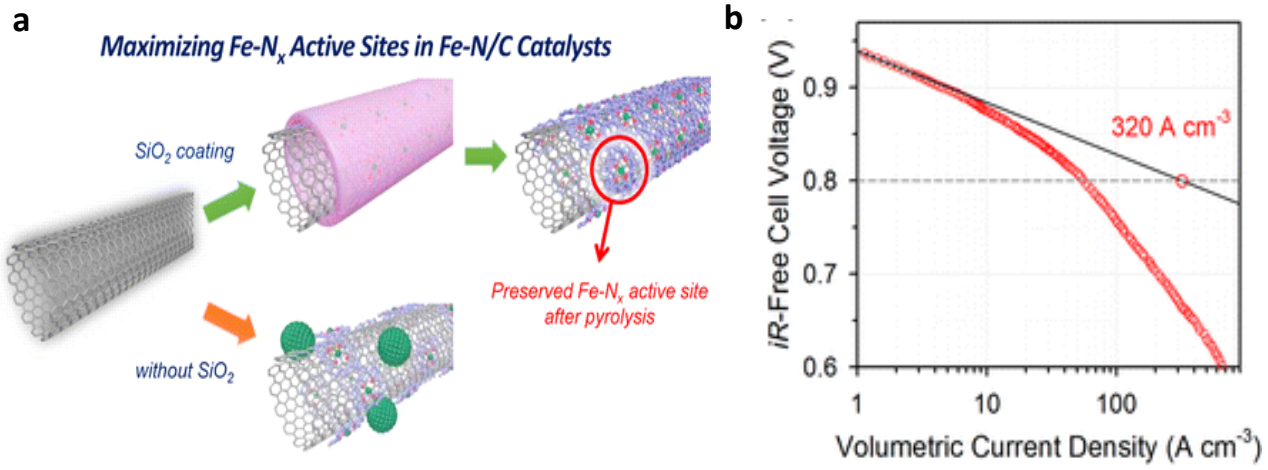

Figure 12. Porphyrin carbon layer/CNT supported Fe catalyst (Fe/PC/CNT)[31]. (a) The synthesis of Fe/PC/CNT with maximizing FeN_x/C sites on the outer layers. (b) PEMFC tests of Fe/PC/CNT.

Very recently, another breakthrough has been achieved with maximized Fe-N_x/C sites[31] by Joo et. al (**Figure 12**). They first mixed CNT with an Fe precursor (a type of Fe porphyrin with FeN_x sites) and then coated with a layer of SiO_2 by hydrolysis of tetraethyl orthosilicate. The coating is the crucial step which can preserve the FeN_x sites in the following pyrolysis (**Figure 12**a). The SiO_2 protection layer is then removed by chemical etching. The final structure of the produced catalyst is a thin layer of porphyrin carbon with maximum FeN_x sites on CNT support (Fe/PC/CNT). Without the SiO_2 protection layer, the Fe porphyrin decomposed resulting in formation of Fe nanoparticles and the prolylized catalysts lost many FeN_x sites. This work provides an ingenious approach to

prevent the FeN_x loss during pyrolysis. This catalyst also shows very high ORR activity with the half-wave potential of 0.79 V comparable to PANI-Fe-C (0.8 V) and even higher kinetic current density (4.5 mA cm^{-2}) at 0.8 V. The PEMFC test disclosed the record performance of 320 A cm^{-3} (**Figure 12**b), which exceeds the 2017/2020 DOE target of 300 A cm^{-3}. However, there is no stability test reported for this kind of highly active materials.

1.4.3. Encapsulated Non-precious Metal-based Catalysts (NPMCs)

High temperature pyrolysis of transition metal containing precursors, in fact, involves formation of carbon around metal nanoparticles, since the amorphous carbon dissolves in the metal phase and then assembles into graphitic carbon by atomic diffusion to the surface. A new type of ORR electrocatalysts, namely encapsulated or confined NPMCs have recently attracted growing interest since it discloses prominently improved stability by virtue of encapsulation of metal active sites by a carbon film[39-52].

The first reported encapsulated NPMC is a pod-like metallic Fe or Co confined in CNT by Bao et. al. [40] (**Figure 13**). The typical structural feature is that the metal core is encapsulated in a few graphitic layers (**Figure 13**a). The composition is suggested to contain amorphous carbon, Fe and/or trace oxidized FeO_x (**Figure 13**b). Electrochemistry tests exhibited significant ORR activity for these CNT encapsulated Fe (CNT@Fe) or FeCo (CNT@FeCo) containing nanoparticles (**Figure 13**c). Although the activity is lower than that of the MN_x/C type catalysts, this type of catalysts discloses remarkably improved stability without visible activity loss during a 200 h PEMFC test (**Figure 13**d), attributable to the encapsulation structure. The encapsulation structure of the catalysts apparently challenges the general viewpoint that the active-sites should be exposed and accessible for reactants. To hypothesize the possible mechanism, the authors performed DFT calculation and suggested that the activity arises from lowered work function of the carbon surface by the electron transfer interaction between Fe nanoparticles (FeNPs) and CNTs. Based on the free energy analysis, pure CNT has high barrier energy of oxygen absorption of up to 1.43 eV. While after incorporation of Fe, it decreases to 0.04 eV. Upon further introduced doping, the oxygen absorption becomes a spontaneous process (-0.44 eV). Although the ORR activity for this type of encapsulated catalysts needs to be further enhanced, this work first demonstrated that the encapsulated Fe catalysts exhibited the ORR activity.

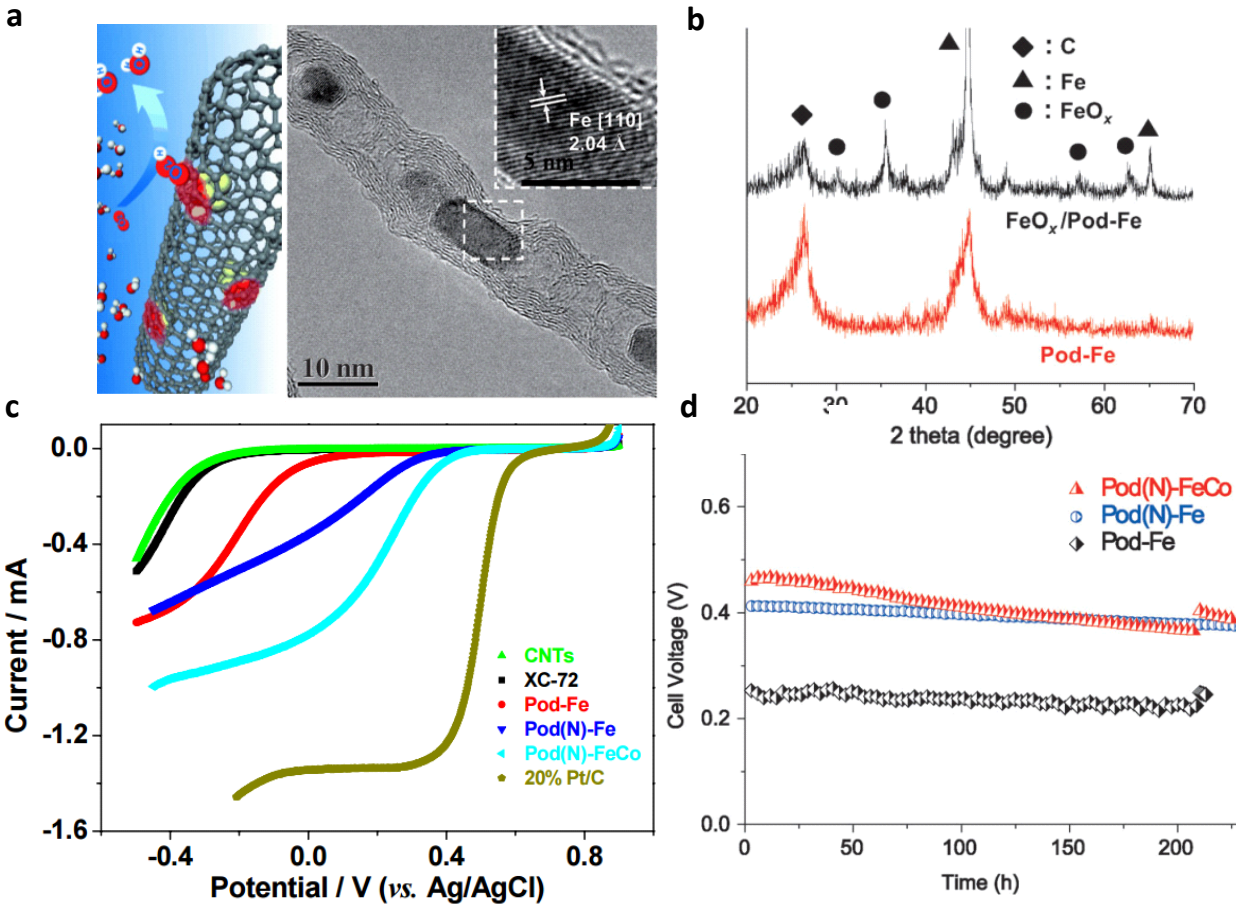

Figure 13. CNT Encapsulated Fe catalysts (CNT@Fe)[40] by pyrolysis of $(NH_4)_4Fe(CN)_6$. (a) TEM images of Pod-Fe with Fe encapsulated within CNTs. The left schematic image illustrates the ORR on CNT@Fe where the encapsulated Fe actives the surface carbon layer. (b) The structural compositions of this CNT@Fe by XRD. (c) ORR polarization curves in 0.1 M H_2SO_4. (d) H_2-O_2 PEMFC durability tests of various samples.

Another interesting piece of work was made by Zelenay et. al. who reported CNT encapsulated Fe by pyrolyzing iron acetate and cyanamide[39] (**Figure 14**). The morphology shows a similar pod-like CNT@Fe nanostructure (**Figure 14a-c**). This catalyst exhibits excellent activity in alkaline media even better than Pt/C when the loading is up to ca.1.0 mg cm^{-2} (**Figure 14**d). Good stability was also observed for this type of catalysts whose half-wave potential even shifted positively after 1000-10,000 potential cycles (**Figure 14**e). Compared to the first Pod-like CNT@Fe[40] by pyrolysis of inorganic Fe salts, this work used organic Fe and C/N supports, which might promote the formation of well-defined CNT@Fe, the origin of the high ORR activity. Unfortunately, the ORR activity in acid media has not been reported and the composition, particularly for the interior Fe components, is unclear.

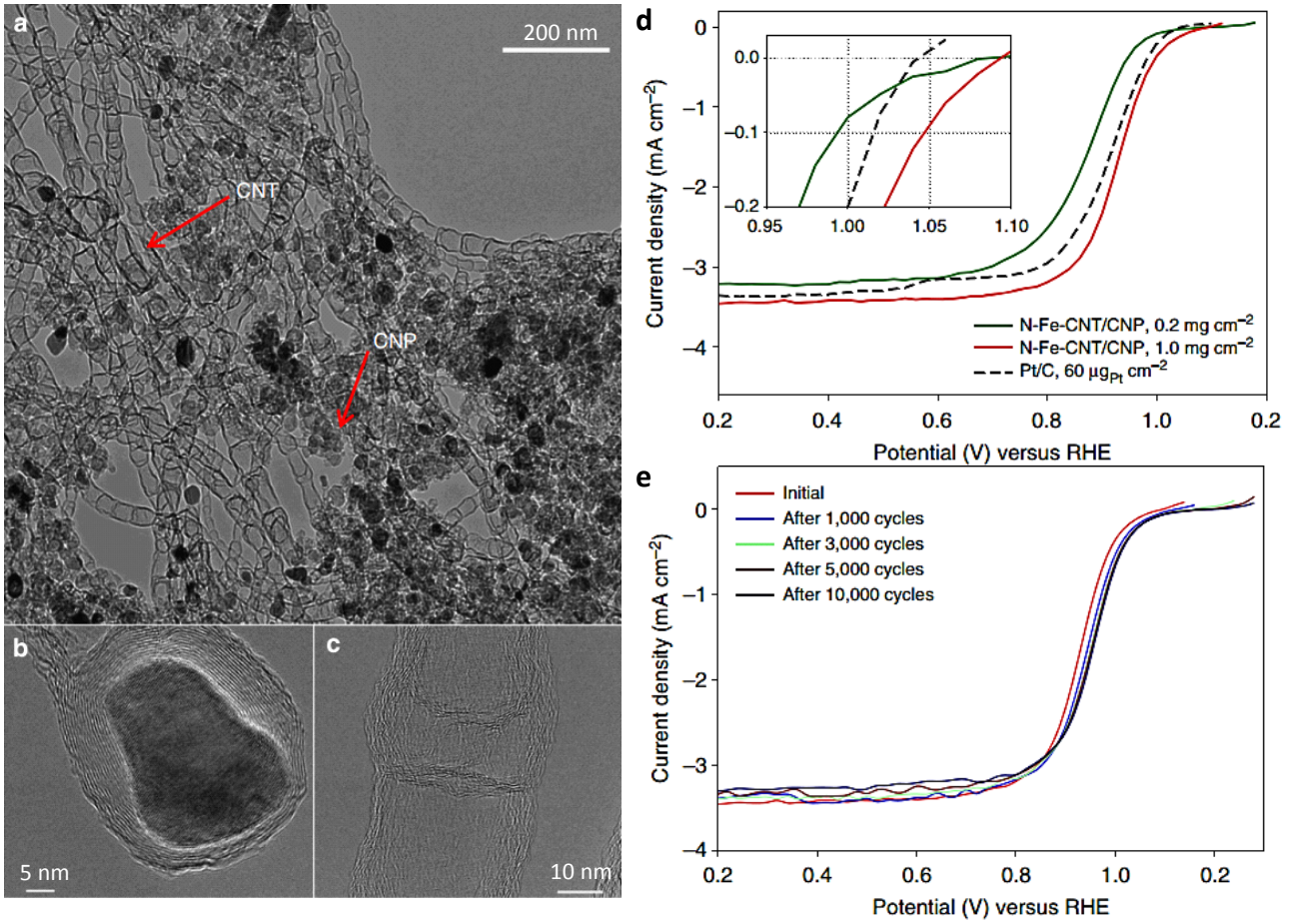

Figure 14. CNT@Fe by pyrolysis of iron acetate and cyanamide[39]. (a-c) TEM images for the CNT@Fe. (d) Electrochemical ORR polarization curves of the synthesized catalysts with low and high loading amounts (0.2 and 1.0 mg cm^{-2}) in alkaline media (0.1 M NaOH). (e) ORR stability examination of ORR polarization curves after 1000-10,000 cycle tests.

Very recently, a highly-active encapsulated Fe based catalyst was proposed by Mukerjee et.al.[46] (**Figure 15**) They used metal-organic-framework (MOF) (ZIF8) as the template and pyrolyzed with FePhen organic precursor (Fe acetate mixed with 1,10-phenanthroline (phen)) in Ar and then NH_3 environment. The resulted FePhen@MOF catalysts exhibit a well-defined encapsulated structure with ca. 2 nm carbon thin film (**Figure 15**a). The structural composition by Mössbauer spectroscopy indicates only inorganic Fe involved in the catalysts including α-Fe, γ-Fe, Fe_3C and Fe_xN without any Fe-N_x coordinated component (**Figure 15**b). ORR tests demonstrated that this FePhen@MOF catalyst discloses high activity: better than Pt/C in alkaline media and close to Pt/C with an onset potential of 0.93 V in acidic media (**Figure 15**). Further PEMFC test showed an open circuit voltage of ca. 0.9 V and very good stability with little activity loss after 10,000 cycles of

potential scans (**Figure 15**d). Overall, this type of FePhen@MOF seems to represent the state-of-the-art performance for the encapsulated NPMCs.

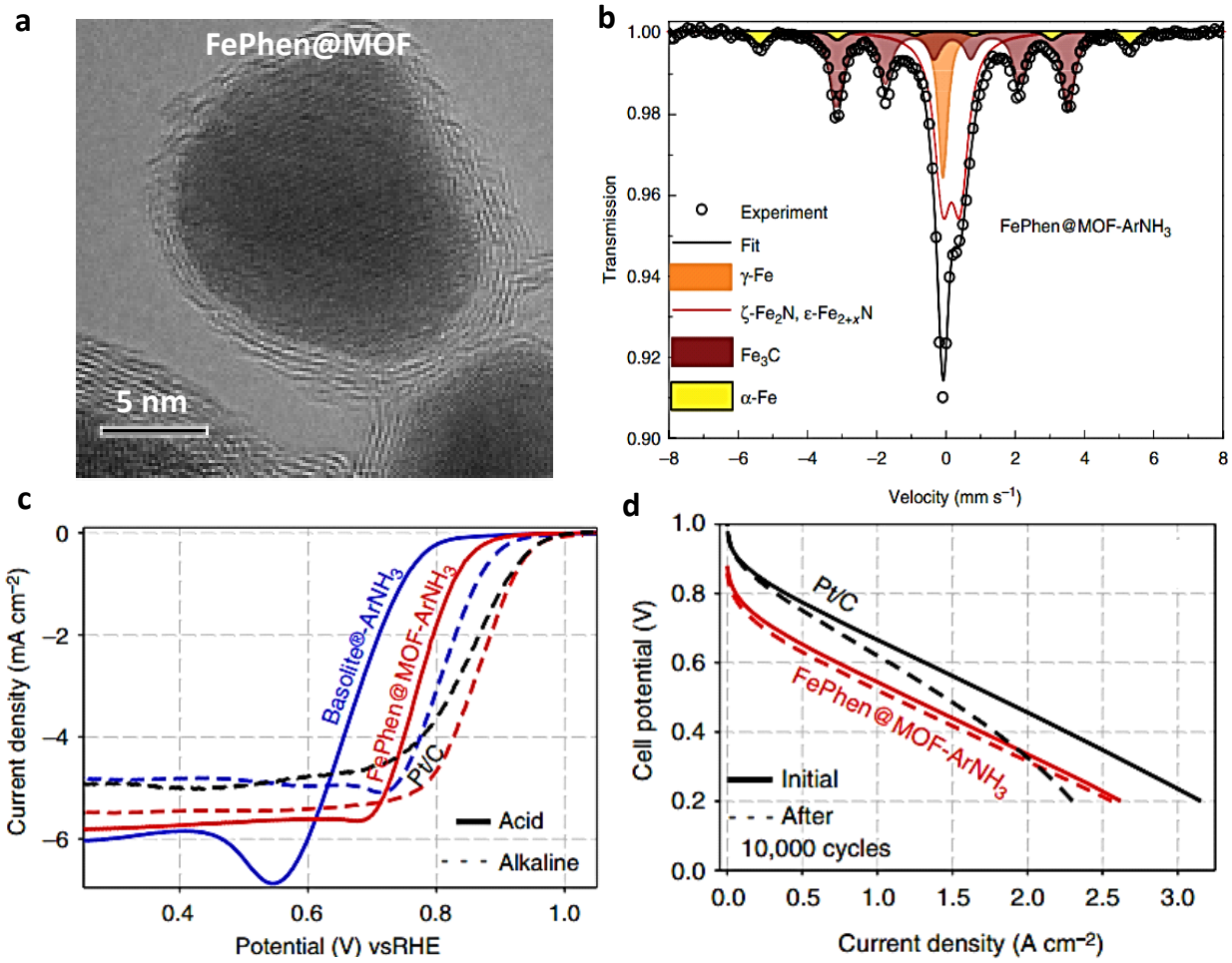

Figure 15. Encapsulated Fe catalysts by pyrolysis of FePhen and MOF (FePhen@MOF)[46]. (a) TEM images of FePhen@MOF in which Fe was encapsulated in a few graphitic layers. (b) The structural compositions of this FePhen@MOF by Mossbauer spectrscopy. (c) ORR polarization curves in both alkaline and acid media. (d) H_2-O_2 PEMFC and durability tests in comparison with Pt/C.

A number of works on this new type of encapsulated catalysts have been published recently, as listed in **Table 3** with information of precursors, pyrolytic temperatures, structures and characterization. The typical examples of this type of catalysts are prepared by pyrolysis of precursors containing carbon, metal, and nitrogen under conditions similar to those for the synthesis of the FeN_x/C catalysts. The catalysts are in general comprised of structures of metal particles confined within thin graphitic layers. These materials exhibited rather high catalytic activities. Most of pyrolysis have been performed in an open system for synthesis of the NPMCs. High-pressure

pyrolysis by autoclave[53-55] might be another effective approach to produce more active sites. Hu et al. recently proposed a new approach of high-pressure pyrolysis to prepare iron-based encapsulated catalysts in a porous hollow carbon sphere structure[41-42]. Based on this approach, this thesis further optimizes the pyrolysis parameters to enhance the ORR activity and explores the active sites.

Table 3. Synthetic conditions and characterization of carbon encapsulated catalysts (the sign @ is used to indicate the encapsulating structure)

Year	Precursors	Pyrolytic temp. ^{o}C	Structure	Characterization
2013	Cyanamide(CH_2N_2), iron acetate ($Fe(CO_2CH_3)_2$), Black Pearls 2000	950	CNT/CNP(N)Fe	ORR-alkaline [39]
2013	Ferrocene, sodium azide(NaN_3), ammonium hexacyanoferrate(II) hydrate ($(NH_4)_4Fe(CN)_6 \cdot xH_2O$)	350, 600	CNT@Fe; CNT(N)@Fe	ORR-acid [40]
2014	Ferrocene ($C_{10}H_{10}Fe$), cyanamide (CH_2N_2); Ferrocene, durene($C_{10}H_{14}$)	700, 800	C@ Fe_3C	ORR – acid&alkaline[41-42]
2014	$FeCl_2$/$FeCl_3$/Resol/F127/PS/g-C_3N_4	900	CNT@Fe-N	ORR-alkaline[43]
2014	$C_6H_{11}FeNO_7$	500-800	NC@Fe/Fe_3C	ORR-alkaline[44]
2014	$FeCl_3$/phenylenediamine, Ketjenblack EC 300J	900	C@FeS(FeN_x)	ORR – acid[45]
2015	ZIF8, 1,10-phenanthroline monohydrate ($C_{12}H_8N_2 \cdot H_2O$), Iron(II) acetate ($Fe(CO_2CH_3)_2$)	1050	CN_x@Fe-Fe_xC	ORR-acid & alkaline[46]
2015	Pluronic P123, melamine($C_3H_6N_6$), $Fe(NO_3)_3$	800	CNT@Fe_3C	ORR - alkaline&acid[47]
2015	Dicyandiamide, $C_6H_{11}FeNO_7$	600-900	NC@Fe	ORR – alkaline[48]
2016	Graphene oxide/Cyanamide/$FeCl_3$	800	Graphene@Fe_2O_3	ORR-acid[49]
2016	Tannic acid ($C_{76}H_{52}O_{46}$), $Fe(NO_3)_3 \cdot 9H_2O$, filter paper, dicyandiamide ($C_2H_4N_4$)	800 ~ 950	C-FeN_x@Fe_3C	ORR – alkaline&acid[50]
2016	$Fe(NO_3)_3.9H_2O$, SBA-15, CH_3CN	700	NC@Fe	OER-alkaline[51]
2016	$FeCl_3$, ammonium peroxydisulfate, Ketjenblack EC 300J	900	C@Fe	ORR-acid[52]

1.4.4. Other Types of NPMCs

In addition to the above two representative NPMCs, there are some other types, such as metal oxides, nitrides and oxynitrides of Groups IV and V with good stability in acidic electrolytes[56].

These compounds, in general have low electric conductivity due to their inherently large band gap and are difficult to adsorb oxygen on the surface. As a result they have exhibited poor catalytic activities. Ota and his coworkers have made great efforts to develop this type of ORR catalysts based on these materials primarily by four methods[56]: 1) formation of a complex oxide layer containing active sites; 2) substitutional doping of nitrogen; 3) introduction of surface oxygen defect and 4) partial oxidation of carbonatites. These modifications were effective to improve the catalytic activity to the oxides with a high stability. The onset potential has been steadily improved through years reaching approximately 0.9 V.

Metal chalcogenides have long been recognized as a potential type of electrocatalysts[57,58]. For instance, widely attracted two-dimensional MoS_2 was demonstrated to be active not only to the hydrogen evolution reaction (HER) catalysts but also to the ORR[59]. Another type is metal phosphides, for example, FeP was recently reported to be active towards the ORR[60]. Moreover, some other potential candidates like MOF itself [60] and single-atom catalysts (e.g., Nb/C)[61] have also been investigated. Overall, these catalysts exhibit somewhat ORR activity (most in alkaline media) but should be further enhanced.

1.4.5. Metal-free Catalysts

Doped carbon without metal deposition is another important type of ORR catalytic materials[23-28]. In fact, carbon is generally used as a substrate for loading the above mentioned metal active materials and itself shows negligible activity toward ORR. Since Dai et. al. first reported that nitrogen-doped carbon nanotube exhibited strong ORR activity[62], doped carbon materials have increasingly gained broad interests.

In the pioneering work by Dai and coworkers[62], they reported vertical aligned N-doped CNTs (N-CNTs) through pyrolysis of iron (II) phthalocyanine in the presence of NH_3 vapor and Fe was then removed by the following electrochemical purification (**Figure 16**a). ORR measurements demonstrated that the N-doped CNTs showed much higher activity than that of un-doped CNTs and even better than Pt/C in alkaline media in terms of onset and half-wave potentials (**Figure 16**b). Through theoretical calculations, the enhanced ORR activity after N-doping was interpreted as the produced positive charges of carbon atoms adjunct N atoms owing to their electronegativity difference. These positively charged carbon atoms might absorb O_2 molecules in a lateral way, which is different from the vertical direction at un-doped CNTs. Such conversion of absorption ways can efficiently lower the ORR activation energy.

The significance of the above mentioned work is a new concept, i.e., atom-doping carbon can prominently promote the ORR activity. It should be noted that this material was prepared by in-situ pyrolysis of iron phthalocyanine (FePc) in the presence of precursors of doping atoms, while not directly prepared through doping CNTs. A controversial question is whether the residue Fe can be removed by the electrochemical etching, as reviewed by Masa et al. [63].

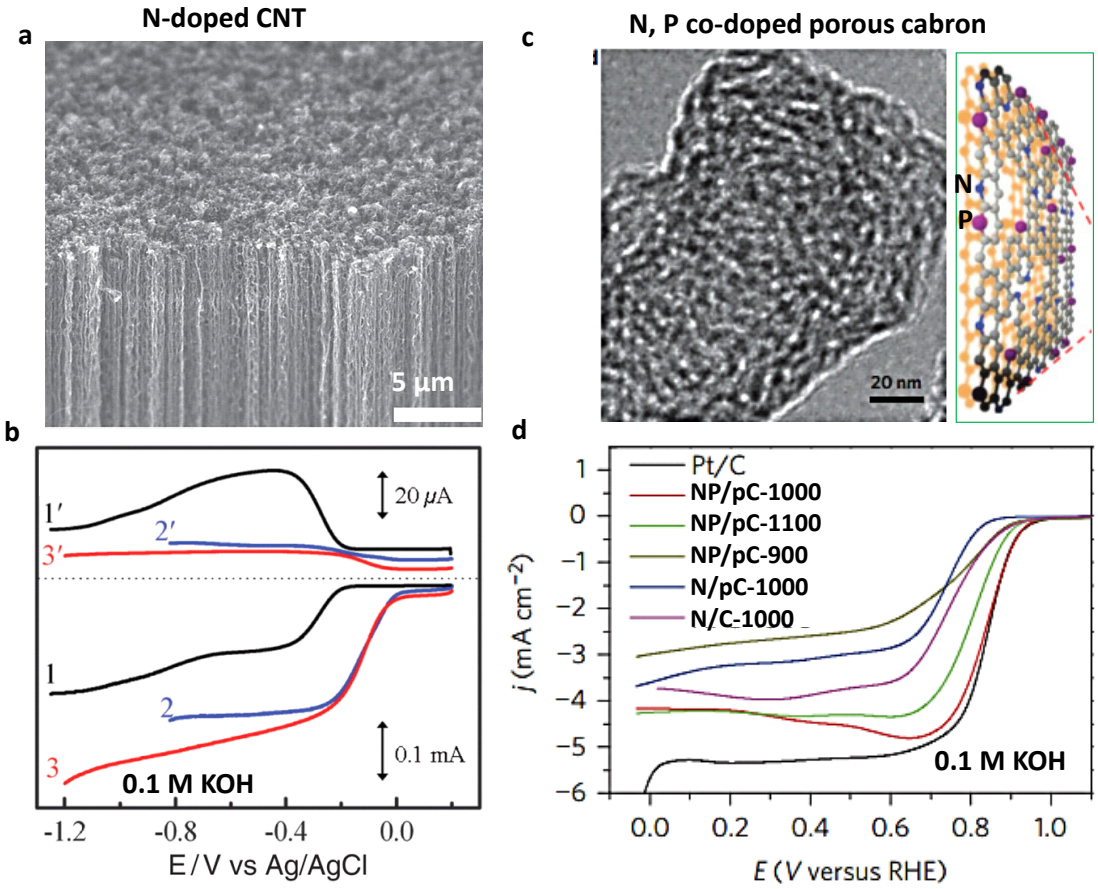

Figure 16. Representative metal-free ORR catalysts. (a) Vertical aligned N-doped CNTs (N-CNTs)[62]. (b) ORR RRDE curves of CNTs (curve 1), Pt/C (curve 3), and N-CNTs (curve 3) in 0.1 M KOH. (c) N,P co-doped porous carbon ORR catalysts (NP/pC)[64]. (d) ORR polarization curves of N,P-doped microporous carbon in 0.1 M KOH.

In recent years, the graphene was also introduced as the metal-free nanomaterial due to its high surface area[65]. Doping atoms except for N have also been expanded to B, S, P, Se and I[66-69]. Meanwhile, binary element co-doping was found to further enhance the activity. For instance, N and P co-doped porous carbon (NP/pC) [64] exhibits higher activity than the only N-doped carbon (**Figure 16**c and d). Overall, state-of-the-art metal-free carbon based catalysts reveal Pt/C comparable ORR activity in alkaline media.

1.4.6. Active Site Exploration

Understanding the active site in the complex heterogeneous catalysts remains a daunting challenge, particularly for NPMCs. For the FeN_x/C type NPMCs, the general understanding of the active sites is that the FeN_4/C structure similar to FePc is a major contributor. In the real catalysts, FeN_4/C sites have numerous configurations such as FePc-like FeN_4/C, FeN_{2+2}/C and N-FeN_{2+2}/C, [70] as shown in **Figure 17**a. Dodelet et.al. have made great efforts to explore the active sites of this type of catalysts[70-73]. They used Mössbauer spectroscopy and have recognized various Fe components. By investigating the correlation between ORR kinetic current density and the content of these metal containing components, they suggested that the FeN_4/C (low spin) and N-FeN_{2+2}/C (protonated N) sites be catalytically active (**Figure 17**a)[70].

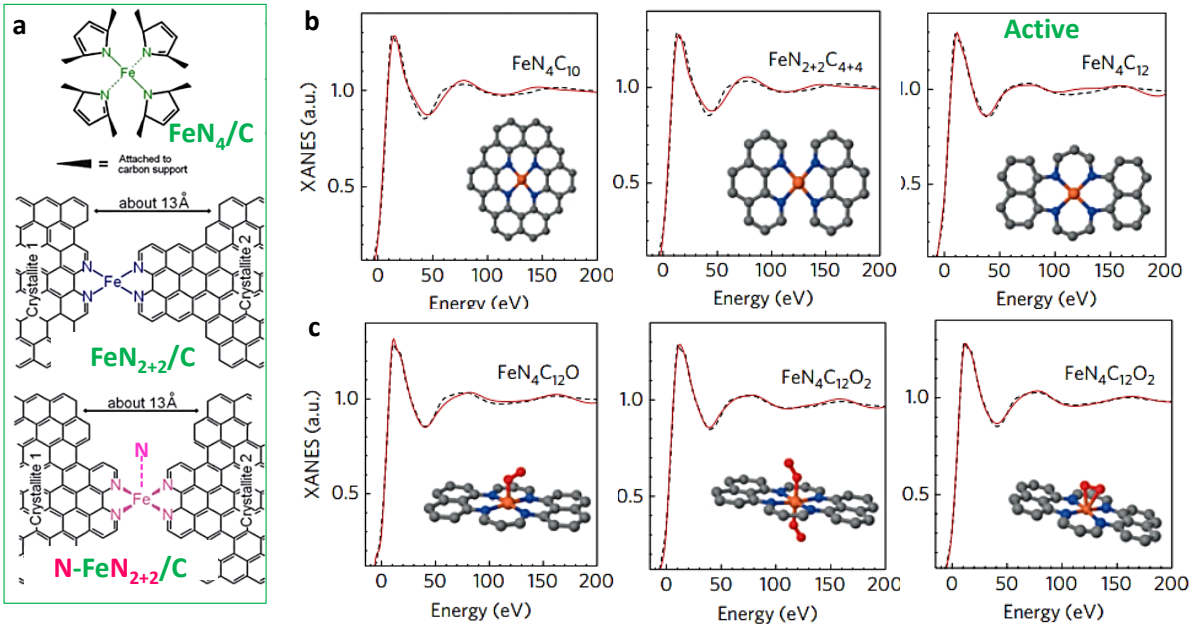

Figure 17. Active sites of FeN_x/C catalysts. (a) Three typical FeN_x/C sites[70]. The top and the bottom configuration were identified as the active sites. (b, c) XANES spectra for identification of active site[74]. Comparison between experimental K-edge XANES spectrum of Fe (black dashed lines) and the theoretical spectrum (solid red lines) with various FeN_x/C configurations.

Very recently, Andrea and Jaouen et. al. used X-ray absorption near-edge spectroscopy (XANES) further confirmed the FeN_x/C structures in details[74] (**Figure 17**b and c). In combination with theoretical simulation, they concluded that the FeN_4C_{12} structure was the active site. This structure is similar to the FeN_4/C **(Figure 17**a) identified by Dodelet group. After determining the active FeN_4C_{12} sites the authors further examined the O_2 absorption models, as shown in Figure 17c,

including one O_2 in end-on (left), two O_2 in end-on (middle) and one O_2 in side-on modes (right). The latter two modes are relatively consistent with the simulation results. These two modes are similar to the two types of ORR mechanisms (i.e., dissociative and associative mechanism) which may both exist. These results represent the current understanding of the active sites of FeN_x/C type catalysts, which should be beneficial to the future rational design of this type of NPMCs.

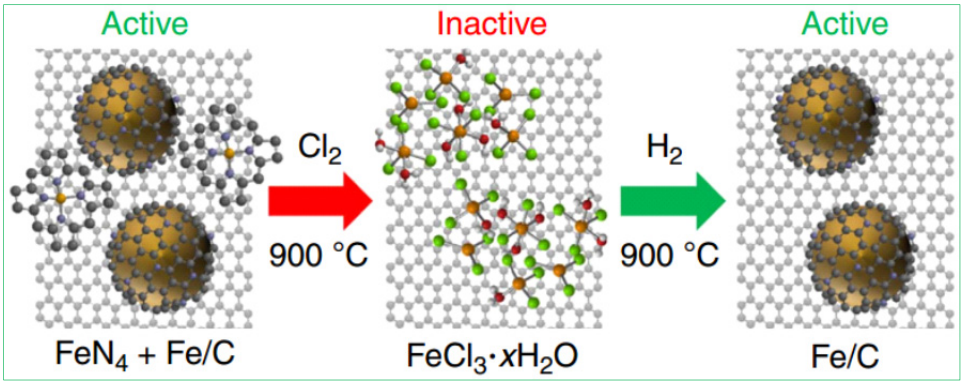

Figure 18. Active sites of encapsulated Fe based catalysts. The active site explored by a Cl_2-etching/H_2-restoring method[52]. This result demonstrates that the encapsulated Fe shows the main active sites.

For the encapsulated NPMCs, the catalytic contribution of those encapsulated metal containing phases is currently still much debated. On one hand, the interaction of the FeN_x/C sites with encapsulated metal containing particles was emphasized[75,76], which is believed to boost the ORR activity. On the other hand, high activity was also observed in no direct iron-nitrogen coordination catalysts[45], for which the catalytic activity was attributed to the encapsulated structure. As recently reported, removal of the inorganic metal species from the FeN_4/C catalyst was found to enhance the ORR activity. A novel approach by Cl_2 etching and H_2-restoring provides encouraging results for understanding the active site[52] (**Figure 18**). The authors prepared encapsulated Fe based catalysts that may contain FeN_x/C and confined Fe species. They first used Cl_2 to etch all Fe species. Through this treatment, both FeN_x/C and confined Fe species were converted into $FeCl_3$ and the ORR activity was lost. Further, this treated sample was undergone the H_2 reduction. Due to N-containing species removed in Cl_2 etching, the $FeCl_3$ can only be converted into Fe species, which excludes the existence of FeN_x. The recovery of ORR activity after H_2 reduction demonstrates the active sites of encapsulated Fe species. This encouring result first clearly indicates the active contribution of the inner Fe phases. Further identification of the Fe (α-Fe, γ-Fe or Fe_3C) phases and correlations of the iron components with the electrochemical activity should be very informative.

For the metal-free carbon based materials, a well-known fact is that the doping (e.g. N-doping) remarkably enhanced the activity. Five N sites are often observed in many N-doped materials by XPS measurements, including pyridinc N, pyrollic N, pyridonic N, graphitic N and oxidized N (**Figure 19**a). The debate on the active sties is currently concentrated on the pyridinc N and graphitic N[65,77-86]. An ideal case is establishing the correlation between the ORR activity and the content of each N-containing sites or synthesis of single N-type doped carbon materials. The latter option is experimentally challenging. Very recently, Kondo and Nakamura et al. characterized the active sites by using a model carbon of highly oriented pyrolytic graphite (HOPG) and well controlled doping of N species[87]. Their rigorous results demonstrated that the carbon on the adjacent pyridinc N was the active sites (**Figure 19**b). This carbon atom discloses the Lewis basicity, which can efficiently absorb O_2 molecules. It seems that creating more pyridinc N (edge N-doped carbon) could be a key to better metal-free catalysts.

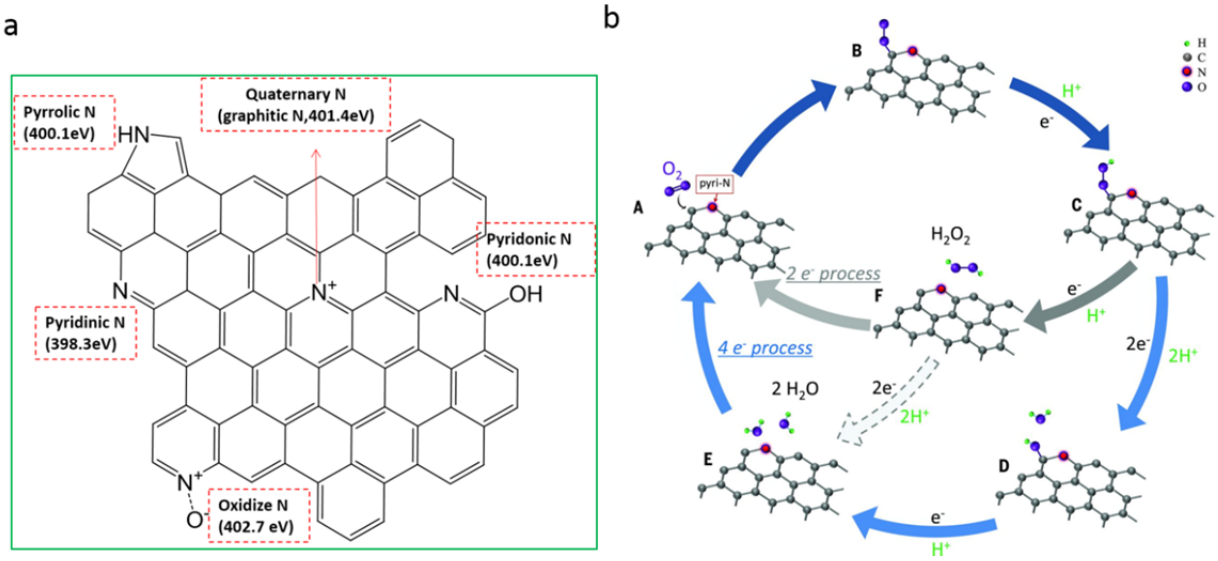

Figure 19. Active sites of N-doped carbon based metal-free materials. (a) Potential five types of doped N on carbon and corresponding binding energy. (b) Recent rigorous results demonstrated that the carbon adjacent pyridinc N is the active site[87].

In brief, the above-discussed active sites may all exist in the real catalysts. How to selective optimize a main type of active sites is synthetically challenging. For example, the N-C sites show good activity in alkaline media but weak activity in acid media. Therefore, FeN_x/C and confined Fe species should be the mainly developed active sites.

1.5. Focus of the Present Work and Structure of the Thesis

This thesis is devoted to investigations of the encapsulated NPMCs for the ORR. For this type of catalysts, there remain a few key issues: (**a**) the ORR performances need to be further enhanced, particularly in acidic media; (**b**) the iron components of the encapsulated particles of the catalysts are not clearly recognized; (**c**) the active site is either poorly understood and much debated. In this thesis, a high-pressure pyrolysis method is proposed to prepare this type of encapsulated catalysts with varied temperatures, durations, and precursors. Morphological, structural, composition and electrochemical characterizations of these prepared samples are systematically carried out. An attempt is made to correlate the catalytic activity and the catalyst components. In addition, electrochemical probes are also used to further clarify the active sites. The thesis is divided into six chapters:

Chapter 1 introduces briefly fundamental aspects of PEMFCs, ORR and its catalysts, followed by a detailed review of NPMCs and selected focus of the thesis work.

Chapter 2 gives principles, instruments and experimental procedures used in the thesis for physical and electrochemical characterization of the synthesized NPMC samples.

Chapter 3 describes the autoclave method and an overview of the synthesized catalyst samples under varied temperatures, durations, and precursors. Results of physical characterization of these catalysts are presented including TEM, HRTEM and elemental mapping, XRD, solid yields, bulk CHN and ICP-MS analysis, and surface XPS.

Chapter 4 is devoted to further identification and quantification of the iron containing components by Mössbauer spectroscopy. Systematic evaluation of electrochemical activities of these catalysts is carried out by RDE and RRDR. Final efforts are made to correlate the ORR activities and contents of iron containing components for exploration of possible active sites.

Chapter 5 reports electrochemical probing of the active sites by anion adsorption and poisoning.

Chapter 6 is a summary of the thesis work based on which perspectives of the subject are outlined.

Chapter 2

Experimental Techniques

This chapter is devoted to a description of basic techniques that have been used in this thesis. Details are given to electrochemical techniques including rotating disk electrode (RDE), rotating-ring-disk electrode (RRDE) voltammetry as well as physical techniques i.e. transmission electron microscopy (TEM), X-ray diffraction (XRD), X-ray photoelectron spectroscopy (XPS) and Mössbauer spectroscopy. Other elemental analysis techniques are briefly described including inductively coupled plasma mass spectrometry (ICP-MS) and elemental CHN analysis. Experimental procedures for the catalysts synthesis, however, will be given together with the result chapters

2.1. Electrochemical Techniques

2.1.1. An Overview of Electrochemical Setup

Electrochemical techniques are general and fundamental methodologies to characterize the electrochemical behaviors and evaluate the electrocatalytic ability of the catalysts. The often used instrument and setup are schematically shown in **Figure 20**. Typically, all electrochemical measurements are performed by a potentiostat (or called electrochemical workstation). It focuses on the study of chemical changes caused by the passage of electric current and the generated energy by chemical reactions. The electrochemical setup in this thesis is based on a general three-electrode system which typically consists of a working electrode (WE), a counter electrode (CE) and a reference electrode (RE).

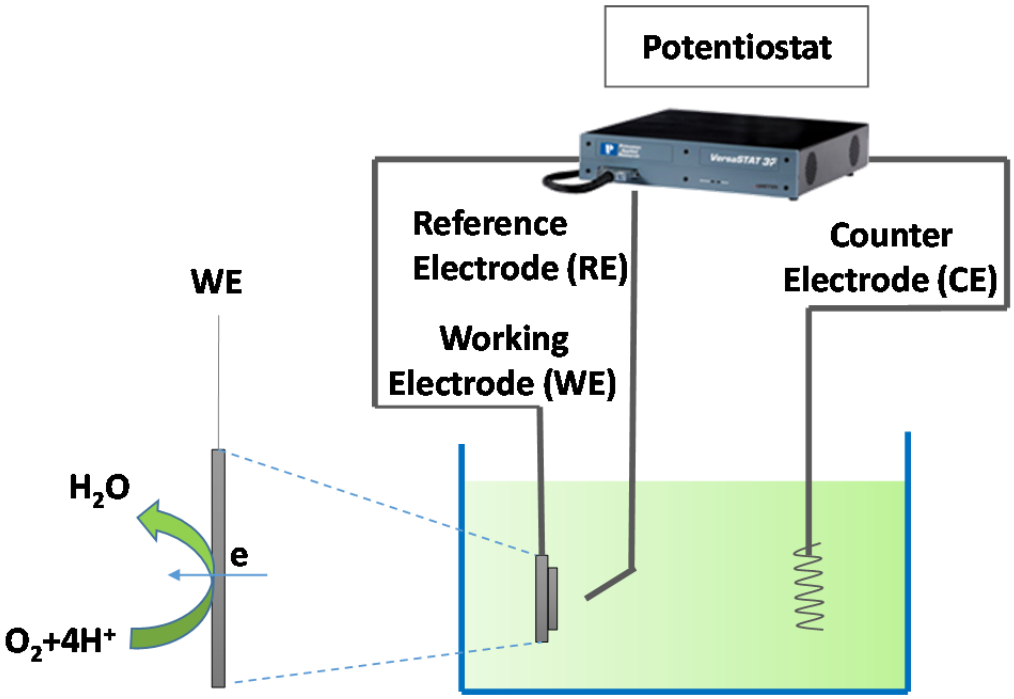

Figure 20. Schematic diagram of a three-electrode setup. The current is recorded between working and counter electrodes and the voltage is measured between the reference and the working electrode.

(a) Working electrode (WE): A glass carbon rod (GC, d = 5 mm) is employed as the WE substrate. Before using, the GC surface is firstly cleaned by polishing and then loaded with the catalyst ink following the procedure as described below:

- Clean procedure:
  1) the GC surface is first polished using of the alumina suspension step by step from 1 μm, 0.3 μm to 0.05 μm on the polishing cloths;
  2) the polished surface is then washed with DI-water and ethanol at least 3 times (each time 5 min);
  3) the GC substrate is finally dried under a gentle N_2 flow.
- Catalyst loading on GCE:
  1) a catalyst ink is first prepared by dispersing the catalyst powder in a solvent, as to be described in Chapter 4.
  2) a certain amount of the ink is applied on the clean surface of the GC.
  3) the applied catalyst layer is then dried in air at room temperature to make sure a uniform film formation.

(b) **Counter electrode (CE):** A platinum wire is usually used as the CE. During the stability measurements, the platinum wire is replaced by a graphite rod in order to avoid any Pt contamination of the electrolyte.

(c) **Reference electrode (RE):** The RE is used to measure and control the potential of the WE. Thus, the RE should possess a stable and fixed potential. The often used reference electrodes are $Hg/Hg_2Cl_2/KCl$ (SCE), Ag/AgCl/KCl, Hg/HgO/KOH and $Hg/Hg_2SO_4/K_2SO_4$. In this thesis, SCE is employed as the RE. Its potential is translated to a value against the reversible hydrogen electrode (RHE) by the equation,

$$E_{\mathrm{RHE}} = E_{\mathrm{SCE}} + 0.059\,pH \tag{12}$$

The reference electrode is frequently calibrated against the RHE, which consists of a flame-cleaned platinum wire immersed in a H_2 de-aerated electrolyte solution. In the case of 0.1 M $HClO_4$, the potential difference between SCE and RHE is typically measured to be 0.303 V. This value is used for the conversion of the RHE value in this thesis.

2.1.2. Rotating Disk Electrode (RDE) Voltammetry

In order to investigate the ORR mechanisms and kinetics, it is important to control the transport of reactants near the surface of the electrode. The RDE voltammetry is the most commonly used technique in the ORR electrochemistry. It can be used for determining the main ORR electrochemical parameters such as the onset potential, half-wave potential, Tafel slope and limiting current density.

The process of reactant transport in the electrolyte at the electrode surface is influenced by three major processes: diffusion, convection, and electrical migration. The effect of electrical migration is essentially electrostatic and can be minimized by using a concentrated electrolyte (e.g., 0.1 M $HClO_4$ electrolyte). RDE is a convection controlled system for measuring an electrochemical reaction under kinetic control. The RDE setup used in this thesis is shown in Figure 21a. Figure 21b schematically shows the effects of diffusion and convection of mass transfer process near the RDE.

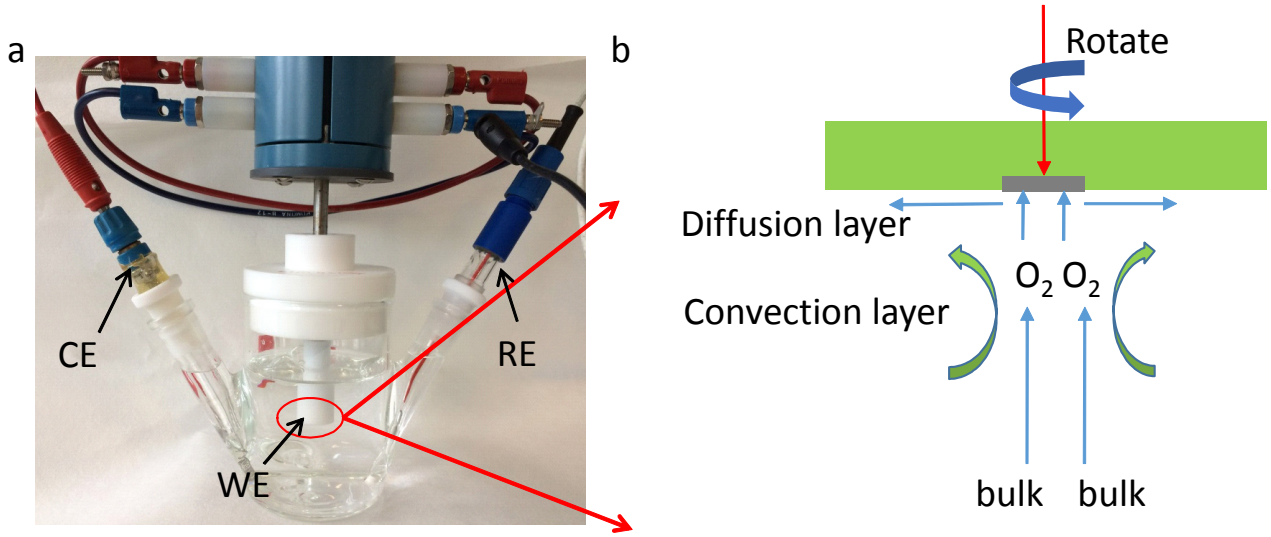

Figure 21. (a) A photo of the RDE setup; (b) The illustration of mass transfer process in RDE system.

If there is no convection in the electrolyte solution, the thickness of diffusion layer will gradually increase, limiting the reaction and resulting in a non-steady-state current density. The central part of the RDE technique is the ability to control the convection rate of the electrolyte solution, and thereby also the reactants in solution as they move together with the electrolyte at the same transport rate. This guarantees that the reactants in the electrolyte solution are constantly transported to the electrode surface and as a result, the diffusion layer will be fixed, though it is possible to exclude mass transfer influence and get kinetic currents for reliable activity measurements. The diffusion layer develops when the reactions happen on the surface of electrode and electrolyte, with the thickness δ being defined by

$$\delta = 1.61 D^{1/3} \upsilon^{1/6} w^{-1/2} \tag{13}$$

$$w = 2\pi f \tag{14}$$

Where D is the reactant diffusion coefficient; ν is the electrolyte kinematic viscosity; ω is the rotation speed of the disk; f is the rotation frequency in Hertz;

If the reaction rate at the electrode is very fast, it will reach a point where all the reactant that can be supplied is consumed immediately, creating a surface concentration of reactant which is virtually zero. In this way, it is possible to obtain the kinetic current by measuring the current in both kinetic limited and the mixed kinetic/diffusion limited region.

In an RDE setup, the thickness of this layer can be controlled by the convection (rotation rate). By increasing the rotation, the thickness of the diffusion layer is lowered and thus the diffusion

limited current is increased. In fact, the diffusion limiting current density (j_L) is proportional to the square root of the rotation rate and can be described by the Levich equation:

$$j_L = nFC\frac{D}{\delta} = 0.62nFCD^{2/3}\upsilon^{-1/6}w^{1/2} \quad (15)$$

Where n is the number of electrons transferred in the reaction, F is the Faraday constant, D is the diffusion constant of O_2 in the electrolyte, C is the concentration of the oxygen, v is the kinematic viscosity of the electrolyte and ω is the rotation speed of the rotating disk electrode.

The activity of the catalyst, one of the key parameters when evaluating ORR catalyst, is defined as the rate of the electrochemical reaction taking place at the surface at a given potential. However, the electrochemical process measurable by the current density on the electrode is not the real kinetic current density of the catalyst. In order to determine the activity accurately, limitation arising from the mass transport of reactant (oxygen in the case of ORR) must be taken into account. The relationship between the measured current density j, the diffusion limited current density j_L and the kinetic current density j_K is described by the Koutecky-Levich equation:

$$\frac{1}{j} = \frac{1}{j_K} + \frac{1}{j_L} = \frac{1}{j_K} + \frac{1}{0.62nFCD^{2/3}\upsilon^{-1/6}w^{1/2}} \quad (16)$$

The Koutecky-Levich equation can be rearranged to isolate the kinetic current

$$j_K = \frac{j \times j_L}{j_L - j} \quad (17)$$

2.1.3. An Example of RDE Voltammetry

Herein, we show an example of RDE voltammetry of commercial Pt/C catalysts for ORR. In order to obtain the ORR faradaic current, the test first runs in N_2 saturated electrolyte and then switches to the O_2 saturated electrolyte. Typical RDE CVs of the Pt/C catalyst are shown in **Figure 22**. Under saturation of N_2, the Pt/C shows typical voltammetric feature of H_2 absorption/desorption in the H-region and Pt oxidation in the oxidation region (Figure 22a). Upon switching to the O_2 saturated condition, a catalytic wave of ORR is observed from the reduction of PtO_x (**Figure 22**b).

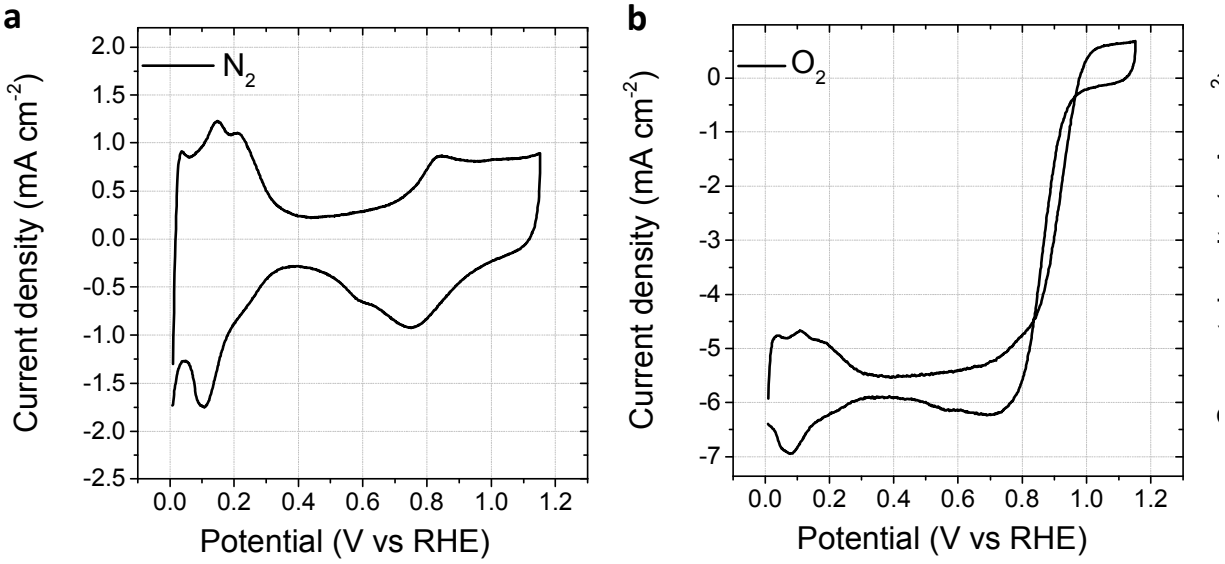

Figure 22. RDE cyclic voltammetric curves of Pt/C catalysts in a) N_2-saturated, (b) O_2-saturated 0.1 M $HClO_4$. Scan rate 10 mV s^{-1}, rotation speed: 1600 rpm.

After extracting the background current, the typical ORR polarization curve is shown in **Figure 23**. The S-type RDE voltammetric curve can be roughly divided into three regions:

(i) the ORR kinetic controlled region (> 0.9 V). In this region, the mass-transport can maintain the requirement of O_2 reaction at the surface of RDE. This kinetically controlled region can be used to evaluate the kinetic current density (the current density at 0.9 V is often used as a reference kinetic current density to evaluate the ORR activity for Pt-based materials) and Tafel slope;

(ii) the diffusion limited region below ~0.8 V. In this region, the concentration of reactants at the electrode surface is very close to zero since the reactants are immediately consumed as they are reaching the catalyst surface and as a result, the mass transport controls the whole reaction.

(iii) a mixed kinetic/diffusion limited region in between. In this region, both kinetic and mass-transport control the reaction.

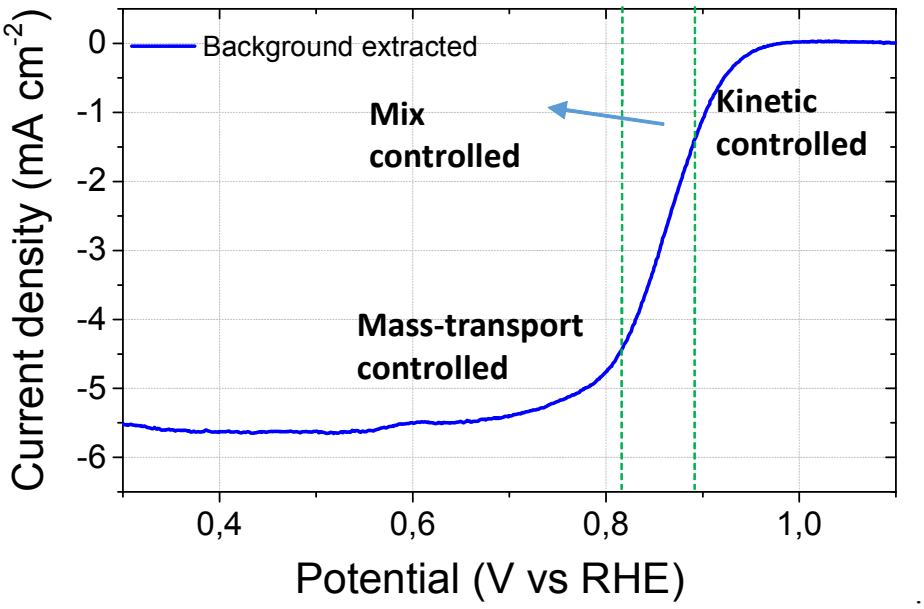

Figure 23. Background extracted RDE voltammetry curves of ORR in O_2-saturated 0.1 M $HClO_4$. Scan rate 10 mV s^{-1}, rotation speed: 1600 rpm.

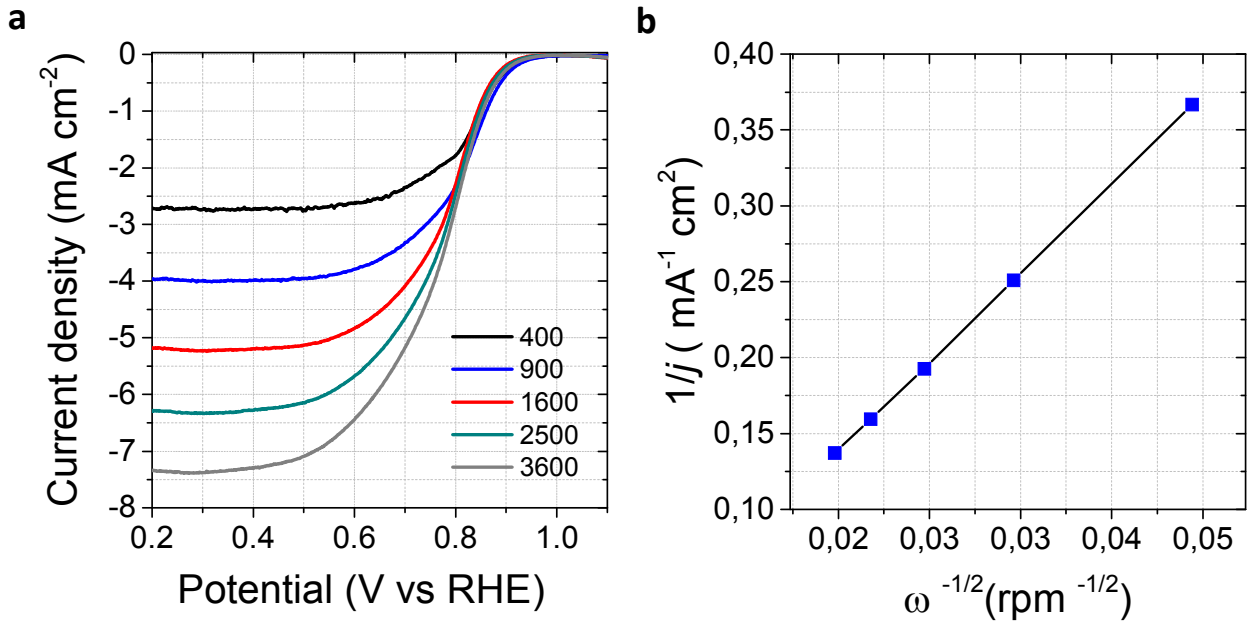

Figure 24. (a) Rotating speed-dependent RDE voltammetry of Pt/C catalyst in O_2-saturated 0.1 M $HClO_4$. The rotation speed is from 400 to 3600 rpm as indicated in the figure. Scan rate: 10 mV s^{-1}. (b) The correlation between limiting current density and rotation speed for determination of the electron transfer (ET) number. The *j* is the current density taken at 0.4 V.

The rotation speed-dependent RDE voltammogram of 20% Pt/C catalysts for the ORR is shown in **Figure 24**. As known, the RDE voltammetry is very useful to determine the number of electron

transfer of the ORR, which can be used to examine the ORR mechanism. According to the K-L equation (eq.16), the limiting current increases with the rotating speed due to the increased mass-transport ability. After mathematic transformation of the current density and speed, a linear correlation between the $1/j$ and $1/w^{1/2}$ is resulted (**Figure 24**b). From the slope, the electron transfer (ET) number is determined to be 3.95 for the used 20% Pt/C catalyst, which corresponds to the $4e^-$ ORR pathway for the common used Pt/C catalysts.

2.1.4. Rotating Ring-disk Electrode (RRDE) Voltammetry

RRDE has two working electrodes (WE), which are separated by a Teflon ring (**Figure 25**a). **Figure 25**b shows the working principle of RRDE. When the oxygen is reduced on the disk electrode, the by-product H_2O_2 can be detected by the oxidation on the ring (the potential of the ring electrode is about 1.1-1.2 V). From the reaction on the ring electrode, one can obtain very useful information which is beneficial to the exploration of the ORR mechanism.

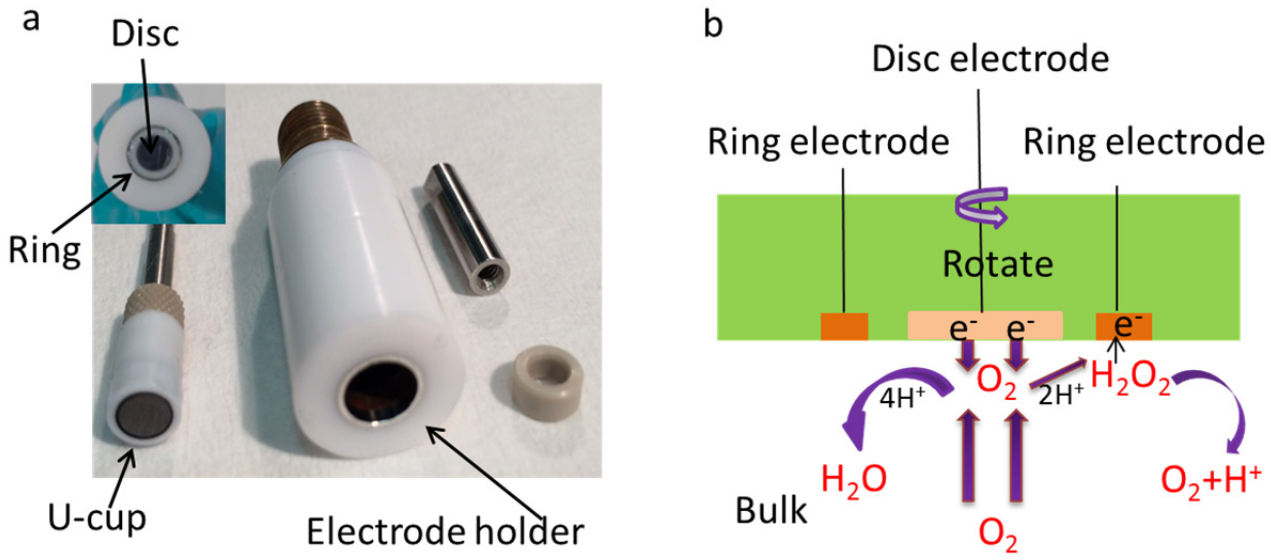

Figure 25. (a) Photos of RRDE composed of a GC disk and a Pt ring electrodes. (b) Schematic representation of work principle of a rotating ring-disk electrode for the oxygen reduction reaction.

2.1.5. An Example of RRDE Voltammetry

Compared to the RDE, the RRDE can quantitatively detect the possible intermediate of H_2O_2 involved in the ORR mechanism. During ORR experiments, the potential of the ring electrode is set to be 1.1-1.2 V. At this potential, there is no current contribution from oxygen reduction or oxygen

evolution and all current measured will be from H_2O_2 oxidation. The fraction of peroxide can be calculated by the following equations:

$$H_2O_2\% = 200\ \frac{I_r / N}{I_d + I_r / N} \tag{18}$$

$$n = 4\frac{I_d}{I_d + I_r / N} \tag{19}$$

Where N is the collection efficiency, which is estimated to be 0.37 by using the ferriferrocyanide redox couple; I_r is the ring current and I_d is the disk current. A typical RRDE voltammetry of the Pt/C catalyst is shown in **Figure 26**. It can be seen that the H_2O_2 is produced at around 0.8 V, which is attributed to the $2e^-$ outer sphere reaction due to the hydroxyl immediate absorbed on the Pt/C catalysts. Another peak of the ring current is detected around 0.4 V, which is due to the $2e^-$ reduction of ORR by the quinone moiety on the carbon supports. From the calculation, it is seen that the produced H_2O_2 is very low, around 1%, and the electron transfer number of ORR is 3.92, which corresponds to an essential $4e^-$ pathway dominated ORR mechanism on Pt/C.

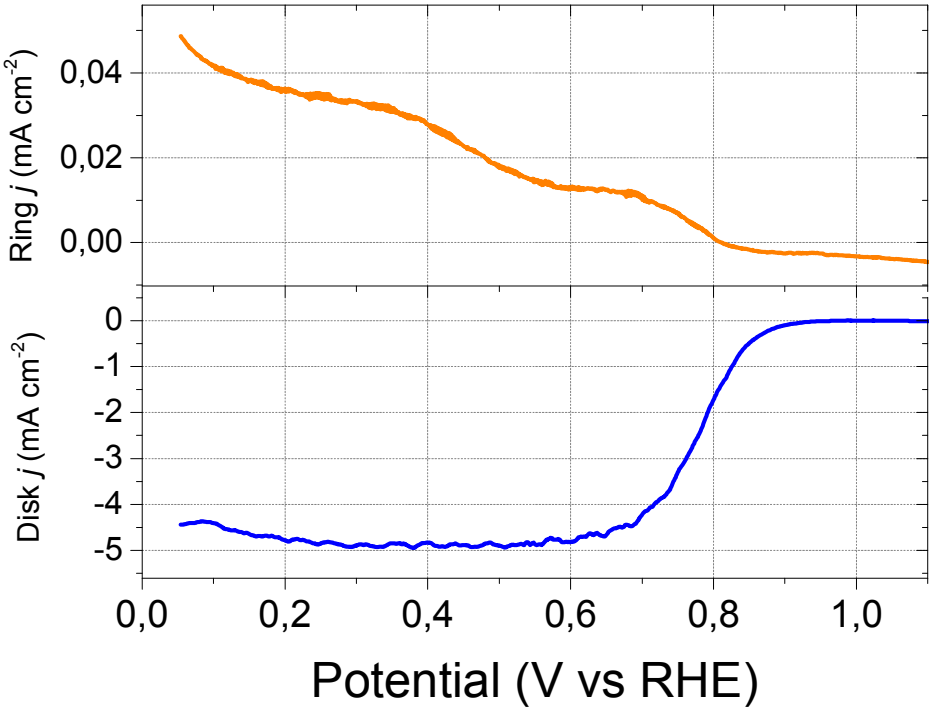

Figure 26. RRDE voltammograms with the disk current ring current and corresponding current to hydrogen peroxide, obtained from the ring current. Measurement was taken at 900 rpm in O_2-saturated 0.1 M $HClO_4$ and 10 mV s^{-1}.

2.2. Transmission Electron Microscopy (TEM)

The development of electron microscopy improves the resolution to the nanoscale and also widens the function of microscopy to morphological observation, crystal structure and composition analysis. In contrast to optical microscopy, transmission electron microscopy (TEM) uses a beam of electrons instead of light, exploiting the wave-particle duality of electrons. TEM allows to magnifying images of very thin samples down to atomic resolution. It is one of the most useful tools for the investigation of nanomaterials. **Figure 27**a is the picture of TEM which has been used in this work. From top to bottom, there are electron gun, condenser, sample room, lens, objective lens, screen, image-forming systems. According to the different functionality, TEM can be divided into four main parts, which are a lighting system (including electron emission source and electromagnetic lenses), sample room, imaging systems (an electron detector) and image observation and recording system (screen and CCD camera).

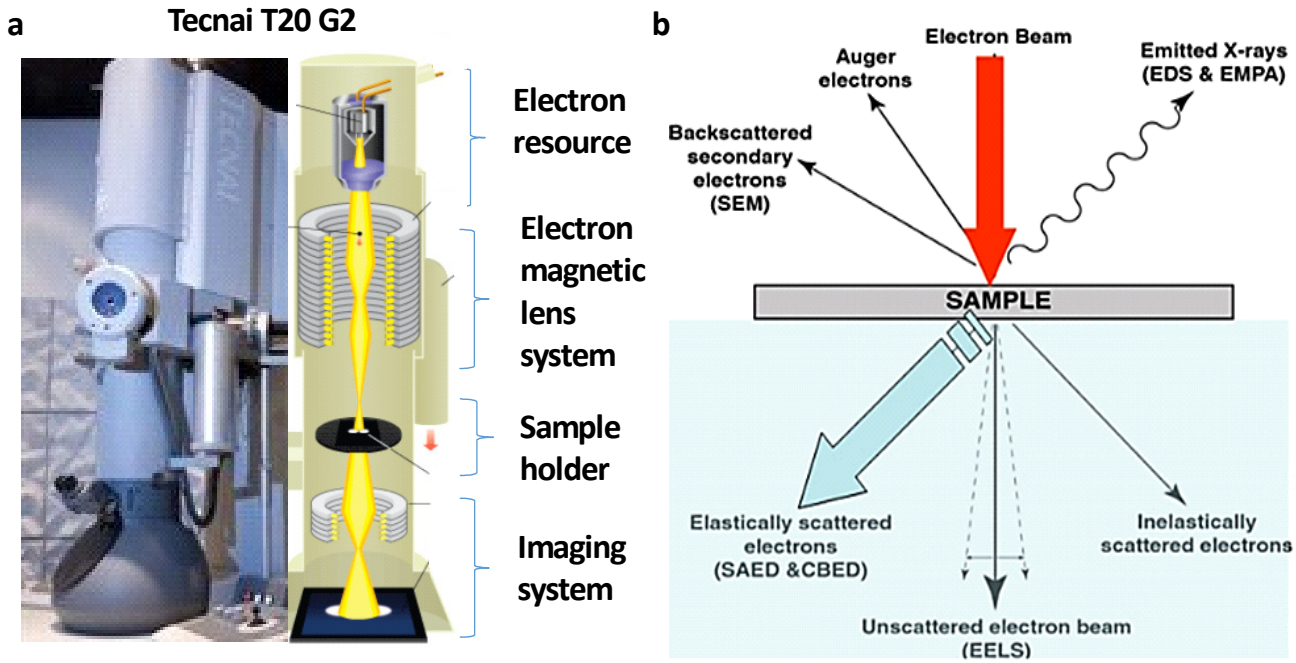

Figure 27. (a) A general cut-away diagram of the internal fine structures of TEM instrument and (b) the possible reactions when the electron beams irradiate on the sample.

Normally, a very thin sample is positioned along the electron beam. The electron beam is produced, accelerated and then focused on the sample by the lenses. The beam passes through the sample which modifies it and imprints its images. The beam is then magnified by other lenses and

detected, for example using fluorescence. One thing that needs to be very careful in the analysis of results is to ensure the morphology images not only on a particular location but the whole sample.

As shown in **Figure 27**b, there are different types of electrons produced when the electron beam contacts the samples. For TEM, the electron passing through of the grids is detected. The sample stops or deflects electrons which depend on the material morphology. In the regions where electrons do not pass through the sample, the image is dark. Where electrons are unscattered, the image is brighter. This is the basic principle for TEM imaging. Owing to the atomic-scale resolution, TEM has been widely used in many fields including physics, chemistry, biology, medicine, and materials science. In my thesis, TEM in combination with EDS was used to investigate the morphology and element composition of the catalyst samples. All TEM measurements were performed on Tecnai T20 G2 from DTU CEN/Danchip.

2.3. X-ray Photoelectron Spectroscopy (XPS)

X-ray photoelectron spectroscopy (XPS) is a surface sensitive technique used to detect the chemical composition of the sample at up to 5 nm of depth. It works by irradiating a sample with x-ray beam and quantify the kinetic energy and the number of electron ejected from the sample. This method is a non-destructive technique that offers quantitative analysis and provides information about the chemical bonds between the element as well as the electronic structures. The principle of XPS is based on the photoelectric effect, as shown in **Figure 28**. A beam of x-ray contacts the sample and excites electron in inner core levels of the atoms with a kinetic energy of:

$$E_k = h\nu - E_b - \Phi \tag{20}$$

Where $h\nu$ is the energy of the incident radiation; E_b the binding energy of the excited electron and Φ is the work function of the analyzer. The incident radiation can be externally controlled. The binding energy and the work function are element-specific dependents. The emitted photoelectrons are collected and then their energy permits are detected which reflects the valence information of the sample

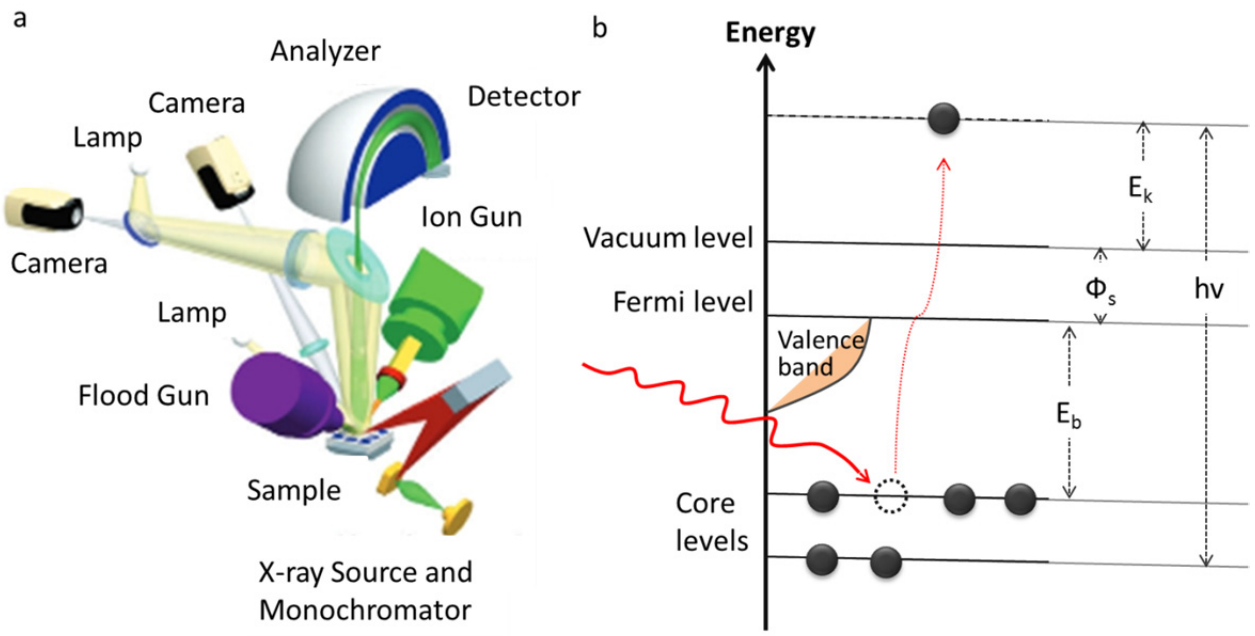

Figure 28. (a) Schematic views of the XPS instrument parts as well as imaging/source/detection system. (b) The fundamental principle of XPS based on the photoelectric effect. The black spheres represent electrons where one of them is exited from a core level to vacuum by the X-ray.

Irradiating the sample with x-ray releases electrons bounded in the sample atoms, which results in photoelectron formation with a specific energy which correlates with the electronic states. The elemental compositions in the sample are thus determined. In the thesis, the XPS-Thermo Scientific instrument is used to perform all the XPS measurements. A schematic view of the XPS equipment was shown in **Figure 28**a. The method probes the most loosely bonded electrons in the sample atoms. As these electrons are the ones participating in chemical bonding with other atoms, their binding energy varies slightly as a result of the chemical environment. This chemical shift is measured by the XPS and thus serves as a powerful characterization tool.

2.4. X-ray Diffraction (XRD)

X-Ray diffraction (XRD) is a powerful technique that can determine the crystalline structures of solid materials. XRD is based on the Rayleigh scattering, the interaction between incoming electromagnetic radiation and the valence electrons of an atom. X-rays are elastically scattered by these electrons, and therefore if there is long range periodicity in the atomic arrangement a constructive interference pattern will occur at certain angles. If no constructive interference occurs, for instance in amorphous samples, the emitted radiation will be inexistent. By measuring the

intensity of the scattered X-rays as a function of the detector angle it is possible to know the crystalline structure of a material, including phase, space group, lattice parameters etc. **Figure 29** shows a schematic diagram of XRD. In particular, Bragg's law gives the conditions for constructive interference:

$$n\lambda = 2d \sin\theta \tag{21}$$

Where d is the distance between planes, λ the radiation wavelength and θ the angle of incidence of the radiation. Typically it is possible to get insight from a measurement by comparing it to a database or to similar materials. In my thesis, XRD will be used for determing the crystal structure and components for the as-prepared catalysts. In the thesis, XRD is used to probe into the compositions and crystal structures of the as prepared catalysts in this thesis.

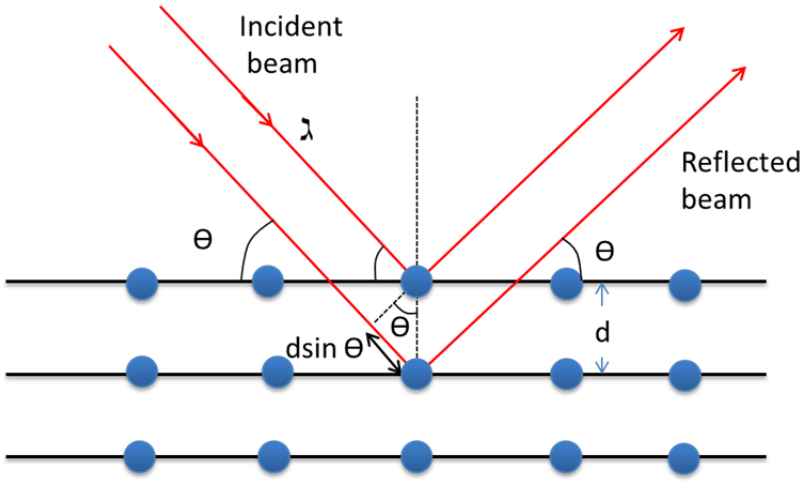

Figure 29. Schematic presentation of the XRD principle. X-Ray is shown as red lines. Atoms in the crystalline planes for constructive interference are shown in bule.

2.5. ^{57}Fe-Mössbauer Spectroscopy

Since the Mössbauer effect[88], i.e., recoilless emission and resonance absorption of γ-radiation was discovered by Rudolf L. Mössbauer in 1958, Mössbauer spectroscopy has rapidly become an advanced technique to probe into the solid materials in multi-disciplines. Mössbauer spectroscopy offers the atomic nuclear information that is very sensitive to the local electronic environmental, structural and magnetic properties of the materials. Owing to this advantage, Mössbauer spectroscopy has been widely used in the catalytic science to explore the catalytic sites and even the reaction process[89] (e.g., *in-situ* Mössbauer spectroscopy). There are ca. 45 identified elements that

can produce Mössbauer effect[90]. The most used is ^{57}Fe since it has both a very low energy γ-ray and long-lived excited state. Herein, we briefly illustrate the basic principle of ^{57}Fe Mössbauer spectroscopy as shown in **Figure 30**. The commonly used radioactive substance is ^{57}Co embedded in a rhodium matrix, which decays to ^{57}Fe and produces γ-ray by further decaying. A modulated minimum energy by moving the resource (called oscillation velocity) is further coupled on the produced γ-ray and then passes through the sample (or absorber). The sample selectively absorbs the energy depending on the Fe nuclear states in the sample (called resonant absorption), which finally exhibits an absorption band in the spectra (**Figure 30**).

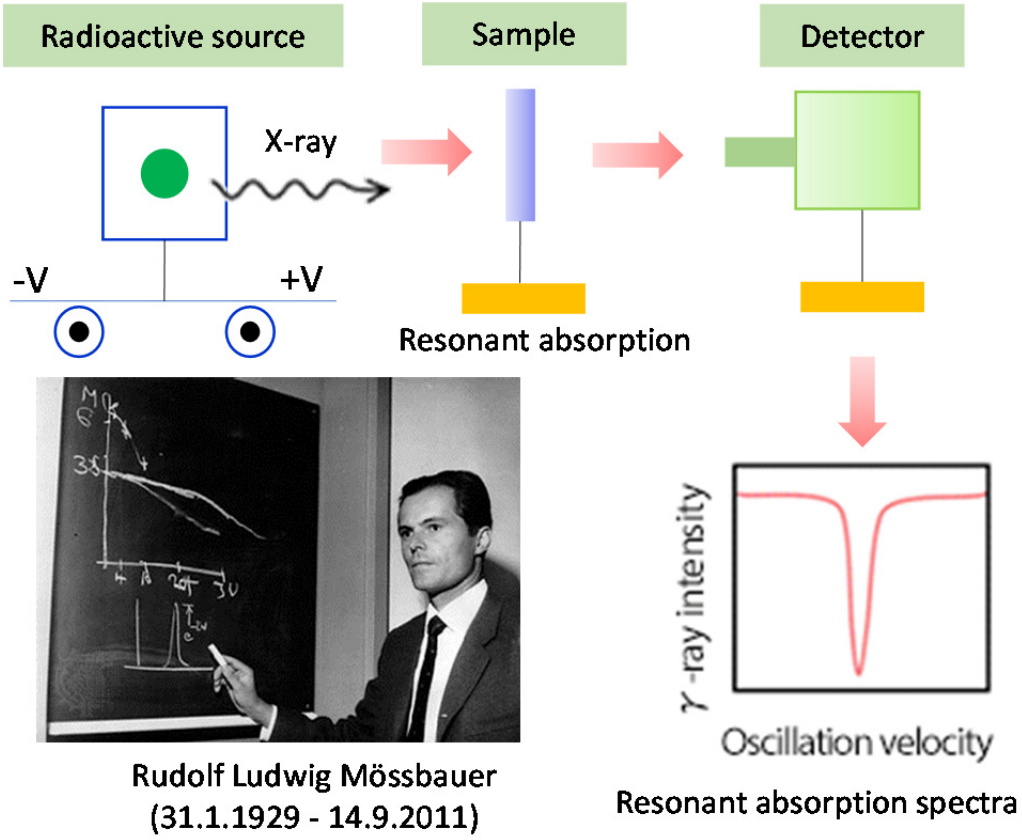

Figure 30. Schematic illustration of the Mössbauer effect and spectroscopy including typical γ-ray resource, sample and detector[88,90].

There are three typical parameters to describe the ^{57}Fe Mössbauer spectroscopy (**Figure 31**). The absorption band position (specific oscillation velocity) is called the isomer shift (IS or δ) (**Figure 31**a), which reflects the difference of *s* electron density, i.e., the difference of transition of Fe nuclear grounded state (1/2) to excited state (3/2) between the source and sample. The neighbor electrons produce an electric field gradient resulting in a splitting of nuclear energy level, which

calls quadrupole splitting (Q_S or ΔE_Q) (**Figure 31**b). If the material owns the magnetism, the band will be further split under magnetic fields (called hyperfine splitting, HS) (**Figure 31**c).

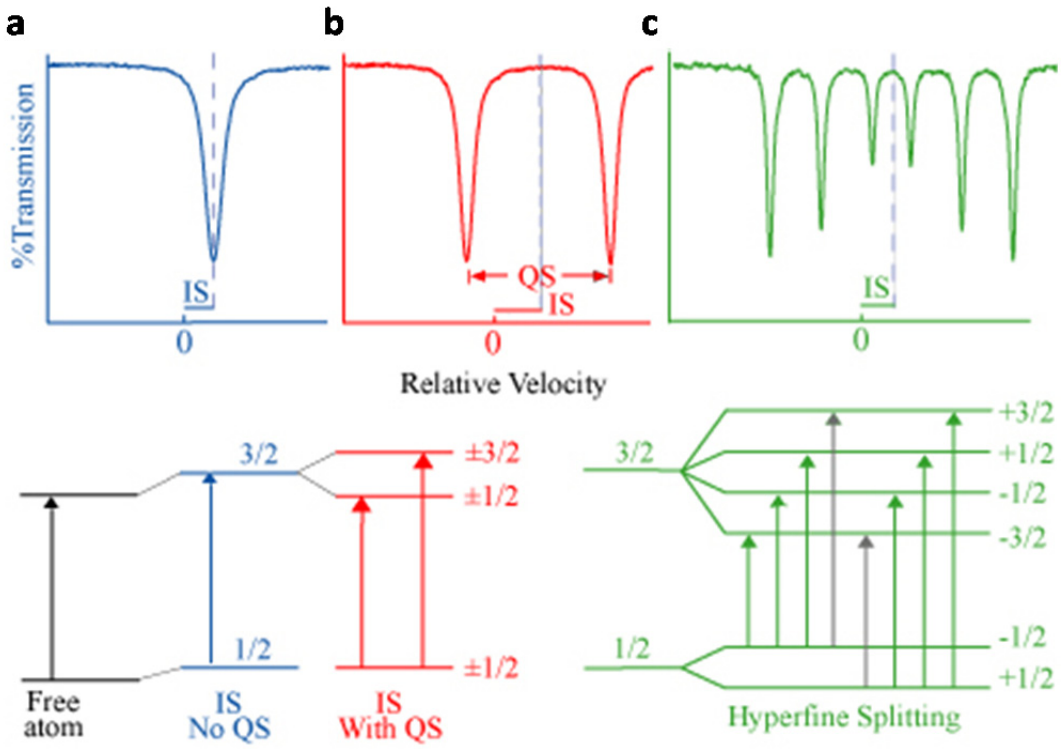

Figure 31. Typical features of ^{57}Fe Mössbauer spectroscopy[91] including (a) the isomer shift (IS or δ), (b) quadrupole splitting (QS or ΔE_Q) and (c) hyperfine splitting (HS).

^{57}Fe-Mössbauer spectroscopy has been widely used to identification of Fe phases in the catalysts, such as different crystals, oxidation states and coordination environmental by the combination of isomer shift and quadrupole splitting as well as the hyperfine field in the case of magnetic phases (**Figure 32**). In the thesis, we use the ^{57}Fe-Mössbauer spectroscopy to recognize various Fe phases in the G@Fe catalysts and further identify the catalytic sites.

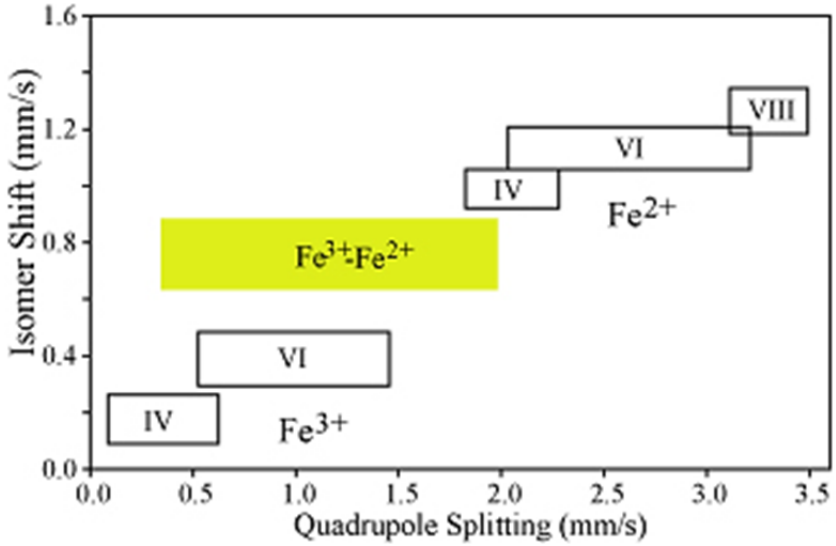

Figure 32. Typical isomer shifts and quadrupole splitting for Fe with different oxidation state and coordination numbers[91].

2.6. Elemental Analysis Techniques

2.6.1. Inductively Coupled Plasma Mass Spectrometry (ICP-MS)

ICP-MS is an analytical technique used for elemental determinations. It combines a high-temperature ICP source with a mass spectrometer. The ICP source converts the atoms of the elements in the sample to ions. These ions are then separated and detected by the mass spectrometer. The MS principle consists of ionizing chemical compounds to generate charged molecules or molecule fragments and measuring their mas-to-charge ratios.

2.6.2. CHN Analysis

CHN analysis is a scientific instrument which can determine the carbon (C), hydrogen (H), and nitrogen (N) elemental concentrations in a given sample. In this technique, a sample is burned in an excess of oxygen and various traps, collecting the combustion products: carbon dioxide, water, and nitric oxide. The masses of these combustion products can be used to calculate the composition of the unknown sample.

Chapter 3

Synthesis and Physical Characterization of the Catalysts

In this Chapter, the dry autoclaving approach to the synthesis of graphitic layer encapsulated iron (G@Fe) based catalysts is described. The synthesis is explored by varying pyrolytic temperatures from 600 to 850 ^{o}C, durations from 15 to 240 mins as well as the precursors from N-containing to N-free compounds. The catalysts are morphologically featured by porous microspheres consisting of uniform iron-containing nanoparticles encased by the graphitic layers. Crystalline structures and the bulk and surface compositions of the catalysts are characterized with respects to the pyrolytic temperatures and durations. Catalysts synthesized from nitrogen-free precursors and the post N-doping are briefly discussed as a comparison.

3.1. Synthesis and Characterization of G@Fe Catalysts

3.1.1. Dry Autoclave Technique

As reviewed in Chapter 1, most NPMCs in literatures have been prepared by pyrolysis in the open systems under ambient pressure. A higher-pressure process is anticipated to be an interesting attempt to synthesize high-performance NPMCs.

General approaches to achieving high pressures are a closed system process in the presence of a solvent, either aqueous or non-aqueous type, at temperatures above the boiling point of the solvent in order to create high pressures. The most popular method is the hydrothermal process, which, as the name indicates, involves water in the synthesis at elevated temperatures above 100 °C and pressures of a few atmospheres. Such a high-temperature and high-pressure apparatus is called autoclave. Gedanken and his co-workers at Bar-Ilan University first suggested a “dry autoclaving”

approach[53-55], where the reactions of precursors were carried out without any solvents. When the temperature was higher than the dissociation temperatures of the precursors, some supercritical phases i.e. solid-liquid, solid-gas or gas-gas were believed to form to create autogenic pressure[54]. These phases go through the nucleation and growth of individual components based on thermodynamic and kinetic stabilities, usually yielding products in nanodimensions[55]. This technique has been well demonstrated for the synthesis of nanostructured carbides, oxides borides, nitrides, phosphides, sulfides, and selenides[53].

Hu et al. seemed the first to employ this method to synthesize NPMCs[41,42,92]. A variety of precursors as nitrogen and metal sources have been screened and eventually a few highly volatile compounds were selected. For doing this, a homemade autoclave of 3.3 mL inner volume was assembled from stainless steel parts. A quartz cup was placed inside the autoclave, which contained the precursors (**Figure 33)**.

3.1.2. Synthesis of the Three Series of Catalysts

This chapter is devoted to a systematic investigation of the process. The precursors of cyanamide (99%), durene (98.5%) and ferrocene (98%) were purchased from Sigma-Aldrich and used as received. Three series of catalysts were synthesized under varied pyrolysis temperatures, pyrolysis times and precursors.

For the *first* series of synthesis of G@Fe at varied pyrolysis temperatures, cyanamide and ferrocene, in a mass ratio of 9 to 1, were pre-mixed and charged into the quartz cup and then seal in the autoclave. To exclude oxygen, the operation was conducted in an argon filled glove box. The autoclave was then closed tightly and placed in a specially designed furnace, which by preheating under a nitrogen atmosphere allowed for a fast heating rate of ca. 140 ^{o}C min^{-1} and easy transfer of the autoclave for immediate cooling after the pyrolysis (**Figure 33**). Pyrolysis was performed at temperatures from 600 to 850 ^{o}C and for a fixed duration of 35 minutes. After pyrolysis, the reactor was taken out of the furnace and cooled to room temperature in air. The solid powder was then collected and the yield was recorded.

For the *second* series of synthesis of G@Fe at varied pyrolysis duration at 700 ^{o}C, all the synthesis processes were the same as the first series of G@Fe.

For the *third* series of synthesis, a nitrogen-free precursor, durene ($C_{10}H_{14}$), was used instead of cyanamide, which was premixed with ferrocene and charged into the autoclave as described above.

For each synthesis, approximate 0.4 g of mixed precursors (durene and ferrocene) was used. A portion of the prepared catalysts was further treated under an NH_3 atmosphere at 850 ^oC for 1 hour and thus obtained samples are called the post N-doped G@Fe.

These samples are through the thesis named after the temperature (in ^oC) and pyrolytic duration (in min). For example, sample 600-35 refers to the catalyst pyrolyzed at 600 ^oC for 35 minutes or sample 700-115 to the catalyst pyrolyzed at 700 ^oC for 115 minutes.

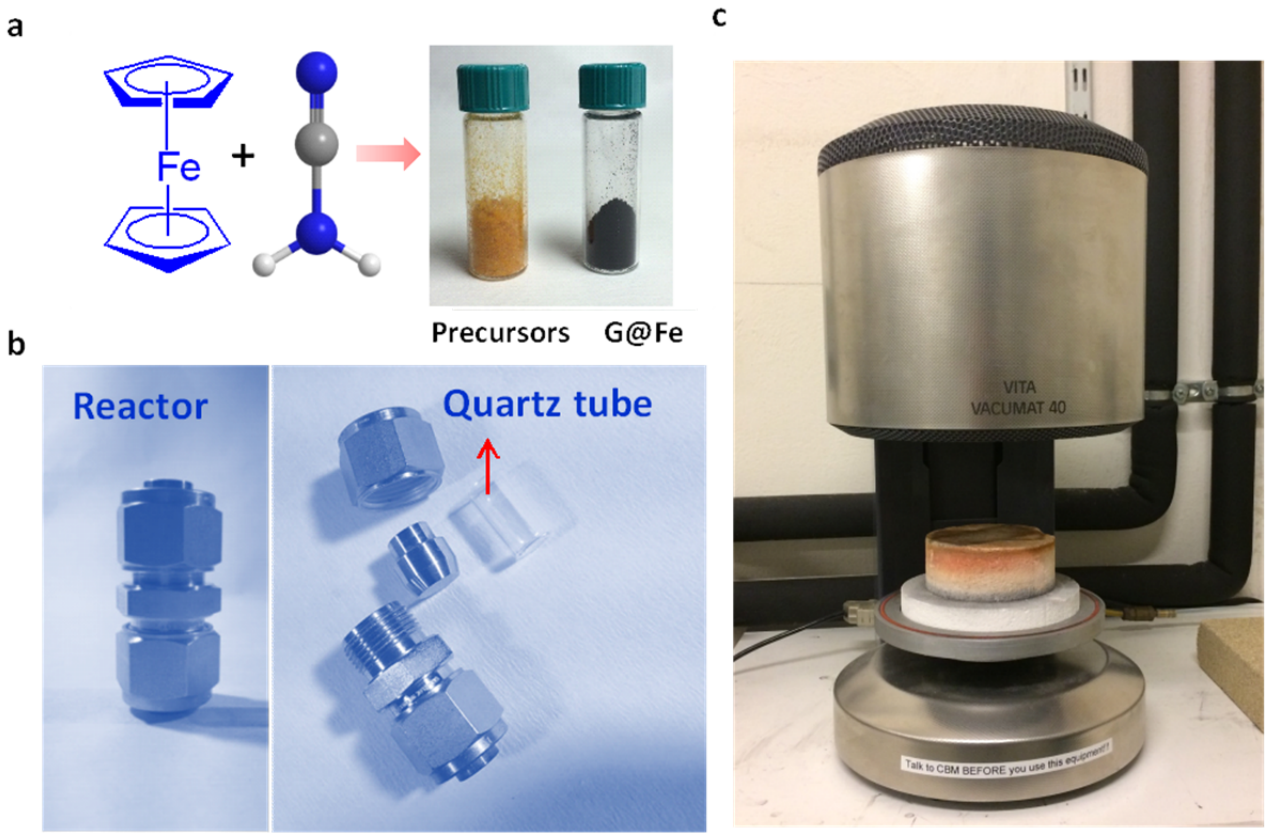

Figure 33. A schematic illustration of the synthesis of G@Fe. (a) A representative synthesis process of G@Fe by one-step pyrolysis of ferrocene and cyanamide. It is the same process for N-free G@Fe by using durene and ferrocene. (b) The used autoclave reactor for pyrolysis made of Swagelog stainless steel fittings and inner quartz tube. (c) The used furnace for pyrolysis.

3.1.3. Characterization of the catalysts

The characterization results of the prepared catalysts are presented in two parts. This chapter is focusing on the yields, bulk elemental compositions, morphologies, metallic phases and surface elemental analysis to the catalysts. Chapter 4 covers the ^{57}Mössbauer spectra and electrochemical

performance evaluation while Chapter 5 presents the further exploration of the active sites by the electro-catalytic poisoning experiment.

3.2. Morphologies by TEM

3.2.1. Effect of Pyrolytic Temperatures

The used precursors of ferrocene and cyanamide are relatively volatile compounds. Under the ambient pressure, ferrocene has a boiling point of 249 ^{o}C and is decomposed at more than 500 ^{o}C, which forms metallic clusters and a series of hydrogen carbon molecules[93]. The cyanamide in a polymeric form, i.e. melamine, has a melting/decomposition temperature of 345 ^{o}C. The pyrolysis of G@Fe catalysts was thus examined from 600-850 ^{o}C. The morphologies of G@Fe prepared at different temperatures are shown in **Figure 34**.

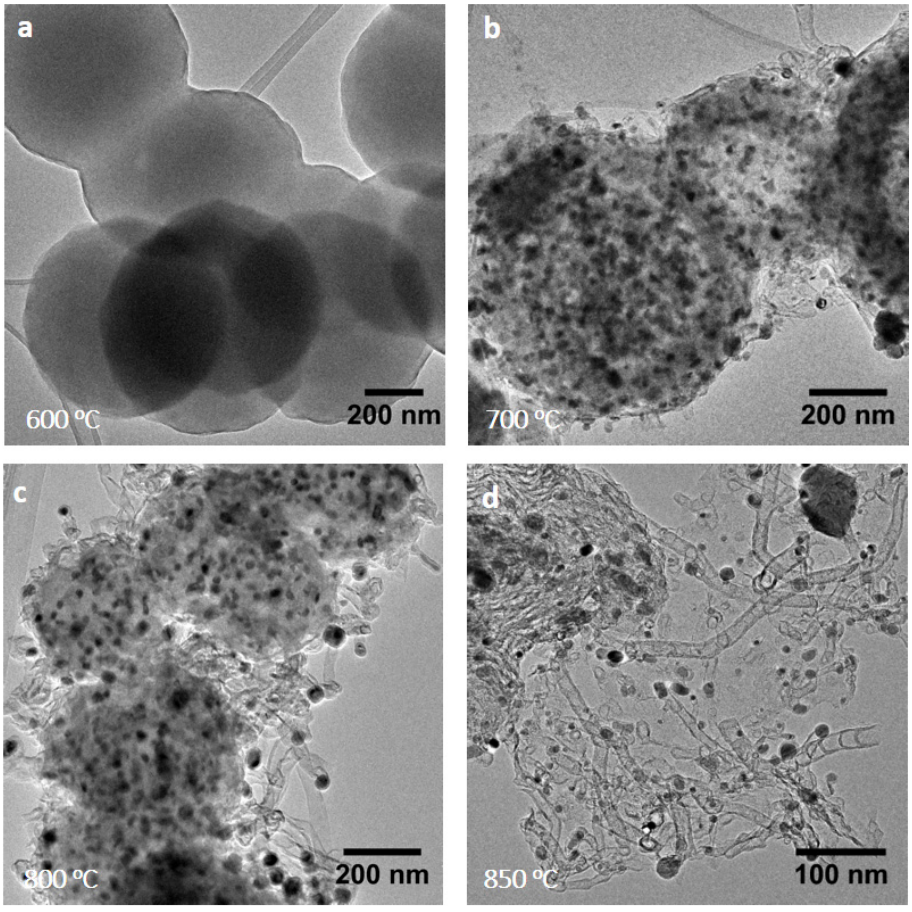

Figure 34. TEM images of the G@Fe catalysts prepared from pyrolysis of cyanamide and ferrocene at (a) 600 ^{o}C, (b) 700 ^{o}C, (c) 800 ^{o}C and (d) 850 ^{o}C. The pyrolysis time is 35 min for all the samples.

At the temperature of 600^{o}C in the autoclave, the polymeric cyanimide i.e. melamine was first formed[92]. In the presence of ferrocene, the polymeric melamine is formed in shape of microspheres around of 500-700 nm diameters, as shown in **Figure 34**a. Ferrocene seemed to play a crucial role in the microsphere formation since the spherical structure cannot be developed when ferrocene was replaced by cobaltocene or nickelocene as the metal precursor. The G@Fe obtained at 700 ^{o}C showed the same micro-spherical structure but becomes porous with the formation of numerous metallic nanoparticles (**Figure 34**b). Meanwhile, a small amount of CNTs around the porous structure was formed. When the temperature was increased to 800 ^{o}C, the microspheres were found to slightly decrease in size and became less regular in shape. Meanwhile, CNTs appeared like branched or interwoven throughout the spheres (**Figure 34**c). Further increasing the temperature up to 850 ^{o}C, the spherical morphology of the catalysts seemed crumpled largely with loose CNTs encapsulating dark nanoparticles (**Figure 34**d), which were the metal containing phases as to be further discussed below. Overall, according to the temperature-dependent pyrolysis, the cutting-off temperature for the formation of well-defined Fe nanoparticle was determined to be ca.700 ^{o}C. The morphologies of G@Fe catalysts remained through the temperatures of up to 800 ^{o}C, above which the morphologies underwent a change from spherical to CNT nanostructures.

3.2.2. Effect of Pyrolytic Duration

For the second series of G@Fe at a fixed temperature of 700 ^{o}C, the cutting-off temperature according to **Figure 34,** the duration was varied from 15 to 240 mins. The morphologies of the obtained samples are shown in **Figure 35**. For a short pyrolysis of 15 min (sample 700-15), the TEM image reveals the formation of metal containing nanoparticles of ca. 10 nm in size within porous spheres and part of the initially formed melamine (containing) spheres still remains. It indicates that 15 min is not sufficient for the development of the catalysts (**Figure 35**a), which will be further discussed in connection with the XRD and XPS results.

The pyrolysis time was then increased to 240 min gradually. From the TEM images, it is seen that the sphere size is slightly decreased from ca. 600-700 nm at 15 minutes to ca. 400-450 nm at 75 minutes. For prolonged pyrolysis more than 75 minutes, no significant morphological changes are observed (**Figure 35**). The feature of this porous spherical morphology of the catalysts is of special interest as it offers an opportunity to study the composition effect on the ORR activity (to be discussed in the next Chapter).

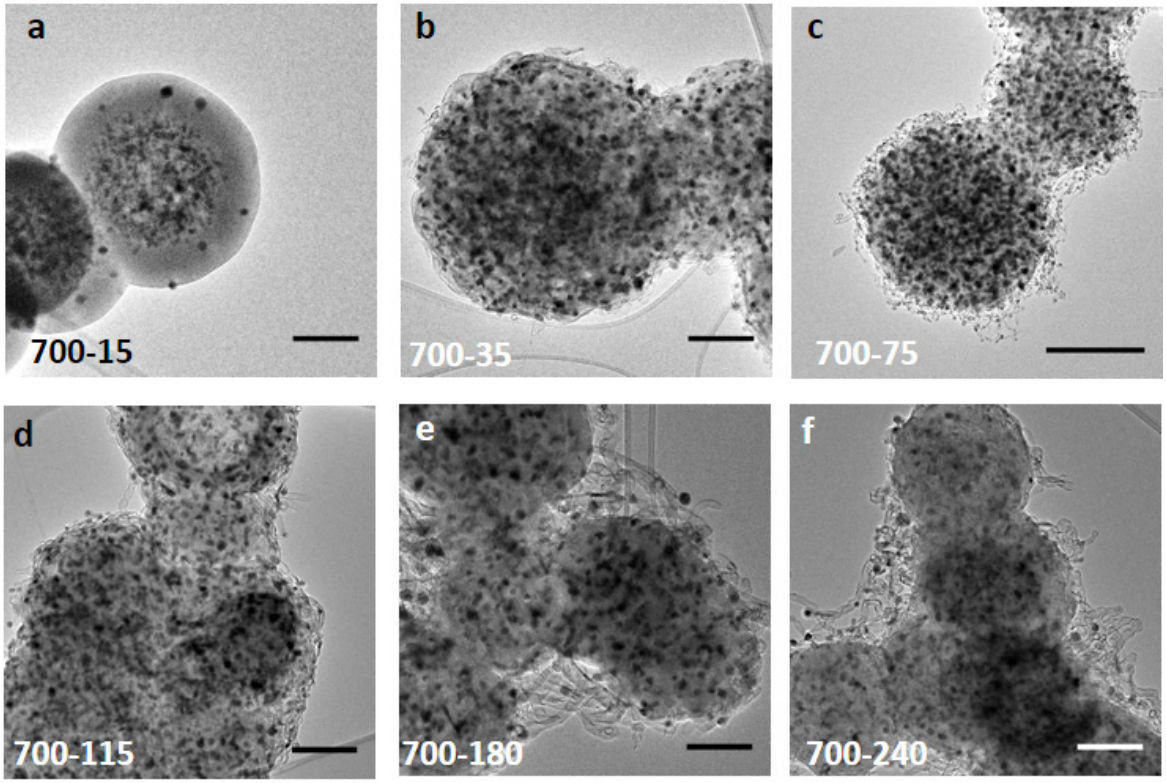

Figure 35. (a-f) TEM images for various G@Fe catalysts at varied pyrolysis times (15-240 mins) at 700 ^{o}C. Scale bars: 200 nm.

3.2.3. Element Distribution and High-resolution Structure

Based on the above featuring morphologies of G@Fe catalysts, further element mapping and high-resolution structures were then examined, as shown in **Figure 36**. Focusing on one typical sphere of the catalyst (700-75), the mapping of C, Fe and N elements revealed their uniform distributions through the sphere (**Figure 36**a). HRTEM images disclose the encapsulated structures of the nanoparticles by carbon layers, which were partially consisting of CNTs (**Figure 36**b-f). The thickness of the carbon layers was ca. 2-4 nm, which is relatively thinner compared with previously reported encapsulated Fe nanomaterials[40,94].

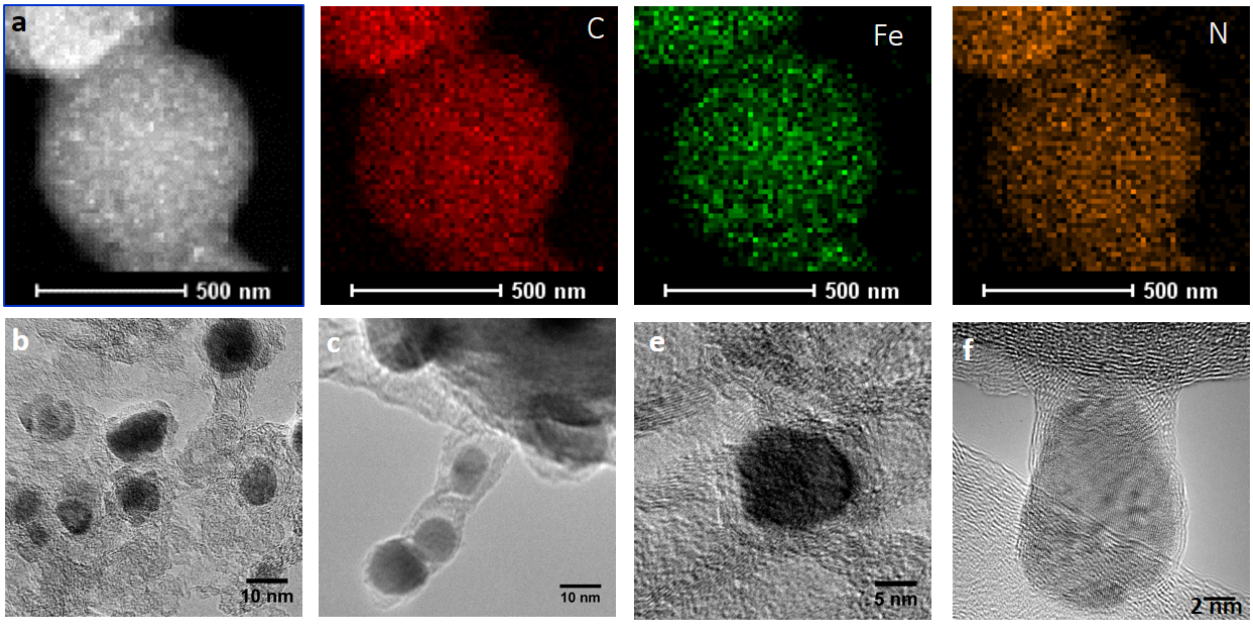

Figure 36. Element mapping and HRTEM for the catalyst sample. (a) The distributions of C, Fe and N of a representative spherical G@Fe (700-75). (b-f) HRTEM images of selected metallic nanoparticles encapsulated by carbon layers. More TEM images for 700-75 are shown in Appendix Figure 1.

The CNT structure seemed to be more dominating at elevated pyrolysis temperatures e.g. 850 ^{o}C. The 850-35 sample was then further examined by HRTEM and element mapping, as shown in **Figure 37.** The overall structural appeared a bamboo-like shape encapsulating Fe nanoparticles in the core (**Figure 37**c). This morphology is similar to the first reported encapsulated structure of pod-like Fe.[40] Element mapping results demonstrated the uniform distribution of C and N (**Figure 37**d & e), however, only the local Fe element was detected in the center of the nanoparticle inside the CNTs (**Figure 37**f).

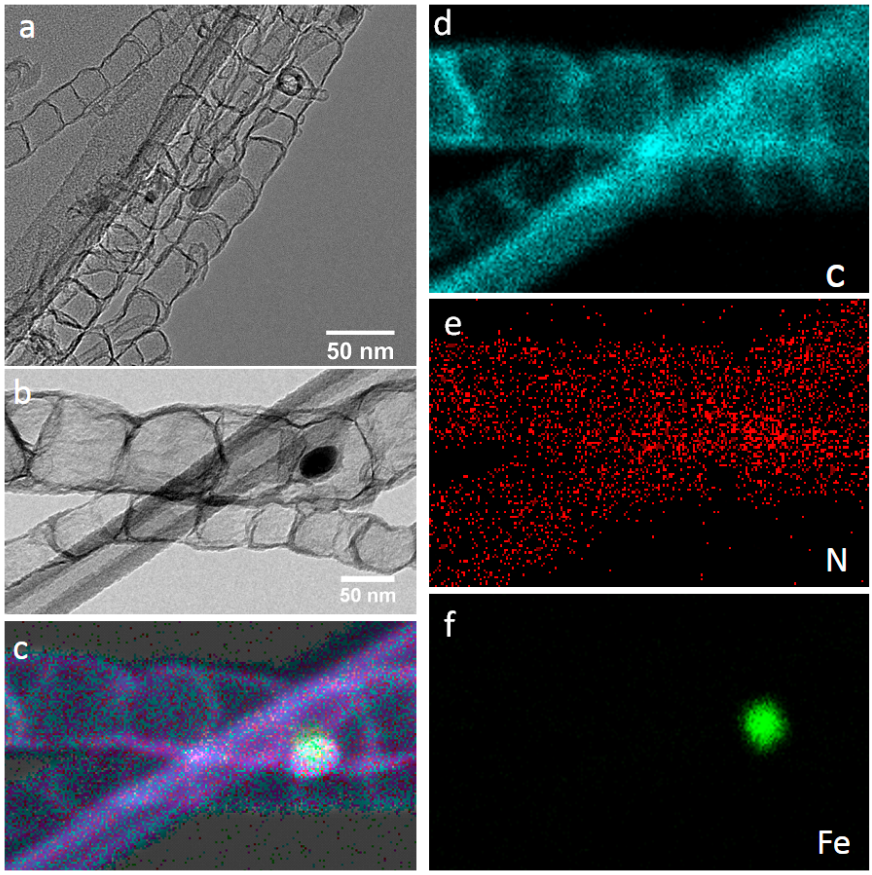

Figure 37. HRTEM images and element mapping of CNT encapsulated G@Fe catalyst (850-35). (a) the typical bamboo-like CNTs with encapsulated Fe containing nanoparticles. (b) the HRTEM image for element mapping of C (d), N (e), Fe (f) and their overlapping (c).

3.3. Crystalline Phases by XRD

The compositions of the crystalline phases of the catalysts were further probed by XRD. XRD patterns of the samples categorized in temperature- and time-dependent groups are shown **in Figure 38** a&b. The first series of samples include those obtained at pyrolysis temperatures of 600, 700, 800 and 850 ^{o}C for a fixed pyrolytic duration of 35 minutes.

The XRD of 600-35 showed only one dominated pattern centered at $2\theta = 27.2^{o}$, which is most likely the newly formed melamine with high crystallinity or/and partially formed graphitic carbon. In addition, no crystalline Fe species were observed in the 600-35 sample, indicating that little or no decomposition of ferrocene at this temperature. This result is consistent with the TEM observation of 600-35 (**Figure 34**a). For the 700-35, a remarkable difference was seen as multi-Fe species were detected including α-Fe, γ-Fe and Fe_3C (red line in **Figure 38a**). Formation of graphitic carbon phase is indexed at $2\theta = 26.3^{o}$ by XRD. Compared with the often claimed Fe, Fe_3C or $Fe@Fe_3C$

phases in literatures[39,41-43,46,48], this result clearly showed the presence of three metallic phases. Upon further increasing temperatures to 800 ^{o}C (sample 800-35) and 850 ^{o}C (sample 850-35), no significant change of the crystalline metal phases was observed.

For the second series of time-dependent G@Fe samples, the XRD patterns are shown in **Figure 38**b. For the 700-15, the previous TEM (**Figure 34**b) exhibited that the Fe nanoparticles started to be formed at this temperature. The XRD further confirms this result as Fe containing phases were detected already by a very short time (15 minutes) of pyrolysis (red line in **Figure 38**b). It seems that the primary metal-containing phase contains inorganic Fe_3N. As the pyrolysis time is increased to 35 minutes (700-35), the crystalline Fe_3N phase vanished while the Fe_3C and other iron components such as α-Fe and γ-Fe phases appeared (**Figure 38**b). Upon further increasing the pyrolytic duration to 75-240 minutes, XRD showed no significant changes in terms of the main XRD peaks for components of α-Fe, γ-Fe and Fe_3C.

Overall, through the XRD characterization, the cutting-off temperature of 700 ^{o}C for the Fe containing nanoparticle formation is further confirmed. The intermediate Fe_3N phase as detected for 700-15 samples is interesting since it has not been previously reported in the literature, though it is decomposing during the following prolong pyrolysis. The finally produced G@Fe catalysts are found to contain main crystalline components of α-Fe, γ-Fe and Fe_3C. The contents of these components, as well as the non-crystalline Fe species, will be further explored by the ^{57}Fe Mössbauer spectroscopy in the next Chapter.

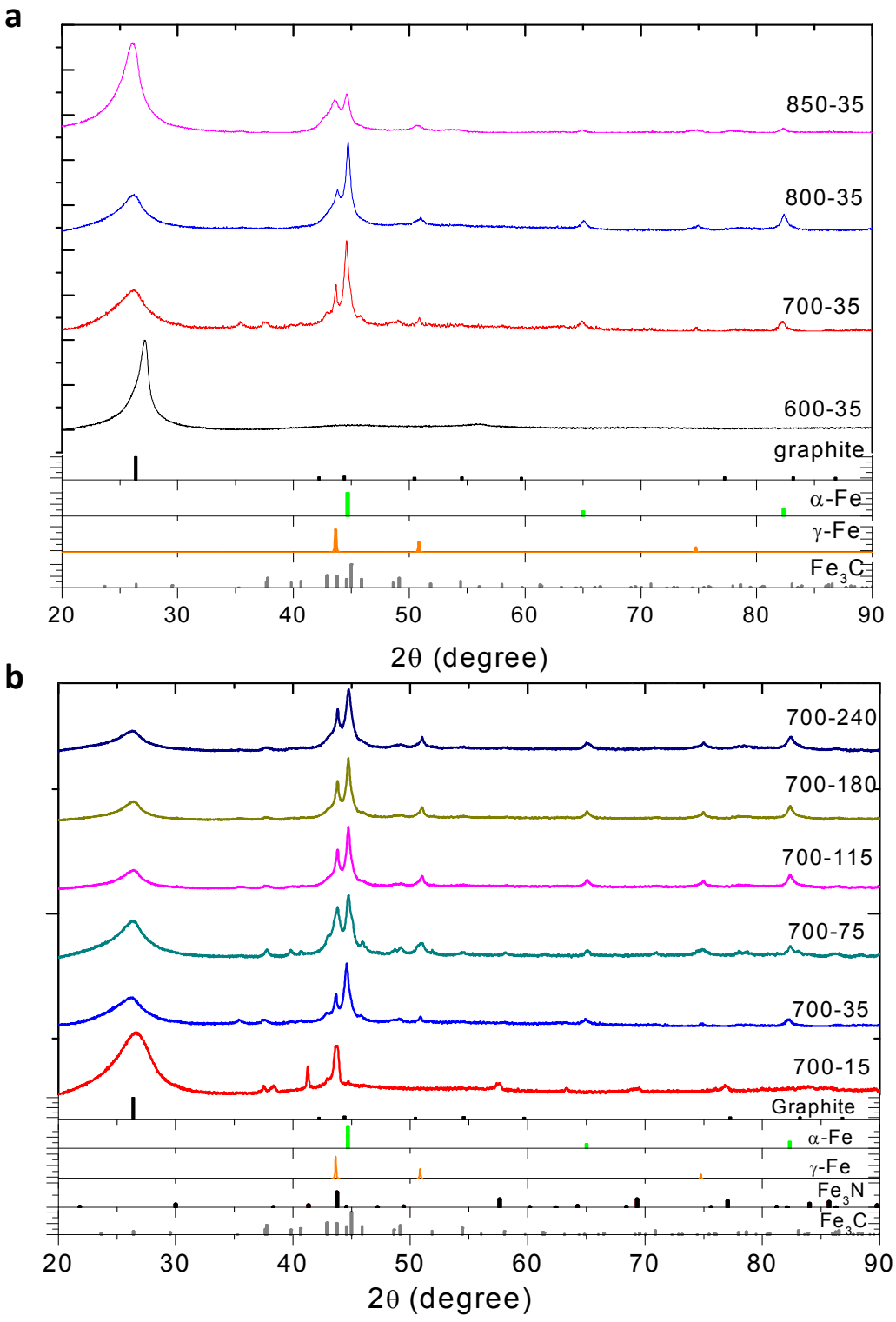

Figure 38. XRD patterns of the catalysts obtain at varied temperatures from 600 to 850 ^{o}C for a fixed pyrolysis duration 35 minutes (a) and varied durations from 15 to 240 mins at a fixed temperature of 700 ^{o}C (b). (Graphite: PDF#41-1487, α-Fe: PDF#06-06969, γ-Fe: (Fm-3m) (CODID-9008469), Fe_3N: (PDF#49-1664) and Fe_3C: PDF#65-2411).

3.4. Solid Yield and Bulk Element Analysis

The solid yield for each synthesis was obtained by collecting the catalyst powders after the pyrolysis and calculated on basis of the initial precursor mass, which provides the information about the practical batch size of the synthesis and conversion of the precursors to the final product. The obtained solid yields as functions of pyrolytic temperature (a) and duration (b) are shown in Figure 39a&b. Also in the Figure are shown the bulk contents of carbon and nitrogen from the CHN analysis as well as the bulk contents of iron from the ICP-MS analysis, also as functions of pyrolytic temperature (c) and duration (d).

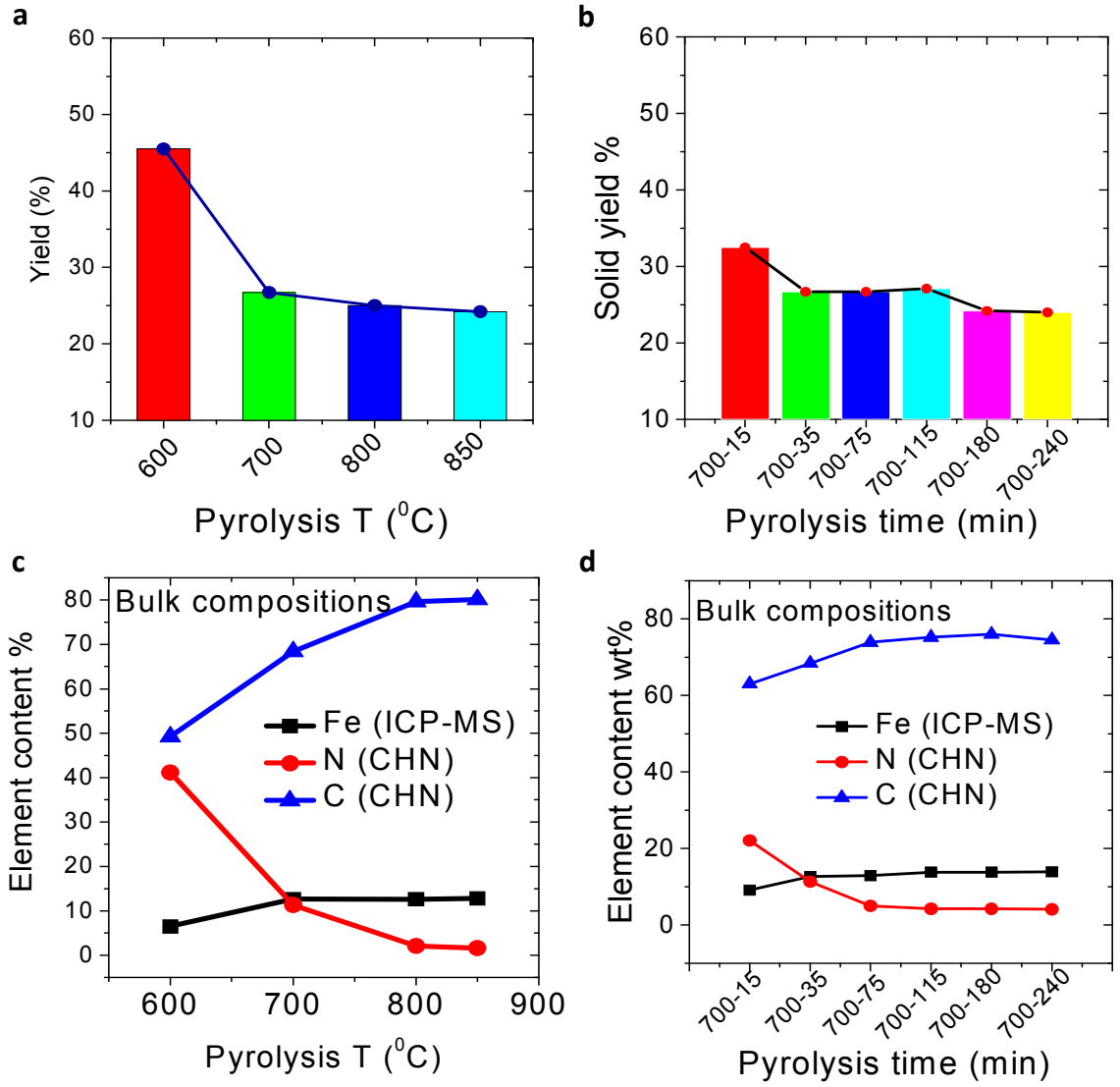

Figure 39. Solid yields of G@Fe catalysts as functions of pyrolytic temperature (a) duration (b) bulk contents of N and C by CHN analysis and of iron by ICP-MS as functions of pyrolysis temperature (c) and duration (d).

At 600 ^{o}C, a significant amount of precursors should remain in the final powder as indicated by the above TEM and XRD and the yield was measured to be as high as 45 wt% of the initial precursors (**Figure 39**a). At the same time, the bulk nitrogen content was also higher than 40 mass% as showed by the CHN elemental analysis (**Figure 39**c).

It seems that a minimum temperature of 700 ^{o}C was indeed needed to achieve a nearly complete decomposition of the precursors, which gave a nearly constant solid yields of about 25 wt% from 700 to 850 ^{o}C (**Figure 39**a) and from 35 to 240 minutes at 700 ^{o}C (**Figure 39b**). A slight decrease in the solid yield was observed for sample 700-35, 800-35 and 850-35 due to release of some nitrogen (see XPS and ICP-MS results)

Of remarks are the samples of 700-180 and 700-240, which showed a slightly lower solid yield of 24% and 24.2%, respectively. Consulting the bulk composition of C, N and Fe for these two samples, which were almost identical to that of samples 700-35, 700-75 and 700-115, a suggestion was made that the collection of the solid powder was not complete. This could happen when the autoclave was opened the high pressure was released with a small portion of the solid powder carried away. In general, these results are consistent with the above TEM and XRD characterization for complete pyrolysis temperature of 700 ^{o}C and duration of 35 min.

Close look at the bulk element contents of Fe, N and C in **Figures 39c** and **39**d reveals that samples of 600-35, 700-15 and 700-35 were apparently suffering from incomplete decomposition of precursors. For sample 700-35, the N content was found to be as high as 11.3 wt%, apparently due to the residual precursor, as to be discussed in the following XPS analysis. From this point of 700-35, either the elevated temperature or prolonged duration resulted in complete decomposition of the precursor. As a consequence, the N content was stabilized a very low level around 1-2 wt%. Accordingly, the Fe content in the catalysts is more or less constant, which is found to be ca. 12-13 wt% of the total solid powder, also in good consistence with the total amount of iron contained in the precursor. The rest is balanced by carbon. As a rough estimation, the typical compositions of these catalysts are about 12-13 wt% Fe, 68-80 wt% C, 2-11 wt% N and the rest balanced by oxygen and probably some hydrogen as well.

3.5. Surface Element Functionalities by XPS

Further efforts are devoted to characterization of the surface functionalities from XPS measurements. The surface element components of Fe, N and C are measured as shown in **Figures**

40 and **41**. The contents for these surface elements are also listed in Table 4. The samples are also categorized in two series of temperature and duration.

For sample 600-35, the C1s spectra contain C-C (sp^2), C-C (sp^3), C-N, HN=C (precursor), C-O and C=O. Of these is the structured carbon i.e. C-C (sp^2) band at 284.6 eV, which steadily increases with temperature. The surface carbon content reached a constant value of ca. 90 wt% at above 700 ^oC (Table 4). This indicates the formation of a conductive phase of graphitic carbon. It is also noted that the HN=C band at 287.6 eV represents the polymerized cyanimide or other pyrolytic intermediates, which exists in the 600-35 sample and was completely decomposed when the temperature was higher than 700 ^oC. The 800-35 sample revealed a small increase of the graphitic carbon and a significant decrease of the overall N content (2.3 wt%, **Table 4**), most likely indicating the formation of the highly conductive N-doped graphitic carbon. When the pyrolytic temperature was increased up to 850 ^oC, no significant change was observed for the carbon layer though a slight decrease of the overall N content (1.9 wt%, Table 4) was seen.

In the N1s spectra, there are five types of surface N components including pyridinice N, precursor N, pyridonic and/or pyrrolic N, graphitic N and oxide N. The detailed featuring structures for these surface N functionalities are shown in **Figure 19a**. The band at 399.6 eV is assigned to the precursor N or N-containing intermediates, which is denoted as Fe-Im and only identified for those samples of incomplete decomposition of precursors at low pyrolytic temperatures (e.g. 600-35). For 700-35, however, nearly complete decomposition was achieved and the corresponding precursor N band disappeared. This is accompanied with a significant decrease in the overall N spectrum intensity (**Figure 44b**). Further increasing the temperatures (800 and 850 ^oC), the surface N content further decreases and finally, only 1.9 wt% N was observed at 850-35.

For the Fe2p XPS, all the samples exhibited very weak intensity and the surface content was determined at ca.1-4 wt% lower than the bulk Fe content (12-13 wt%), which indicates most of the Fe species are encapsulated inside the carbon layer.

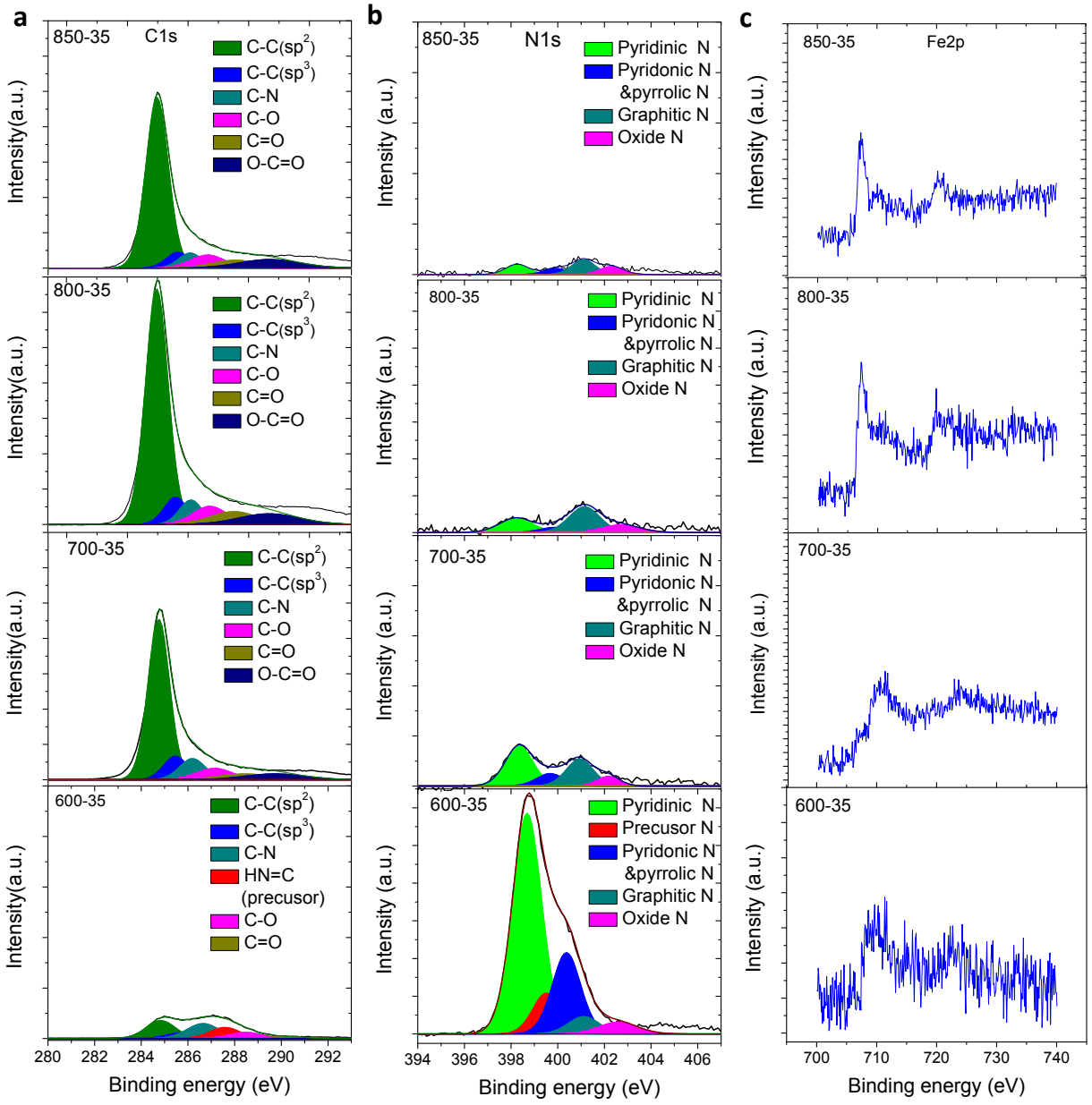

Figure 40. XPS spectra of G@Fe pyrolyzed at 600, 700, 800 and 850 °C for a duration of 35 minutes.

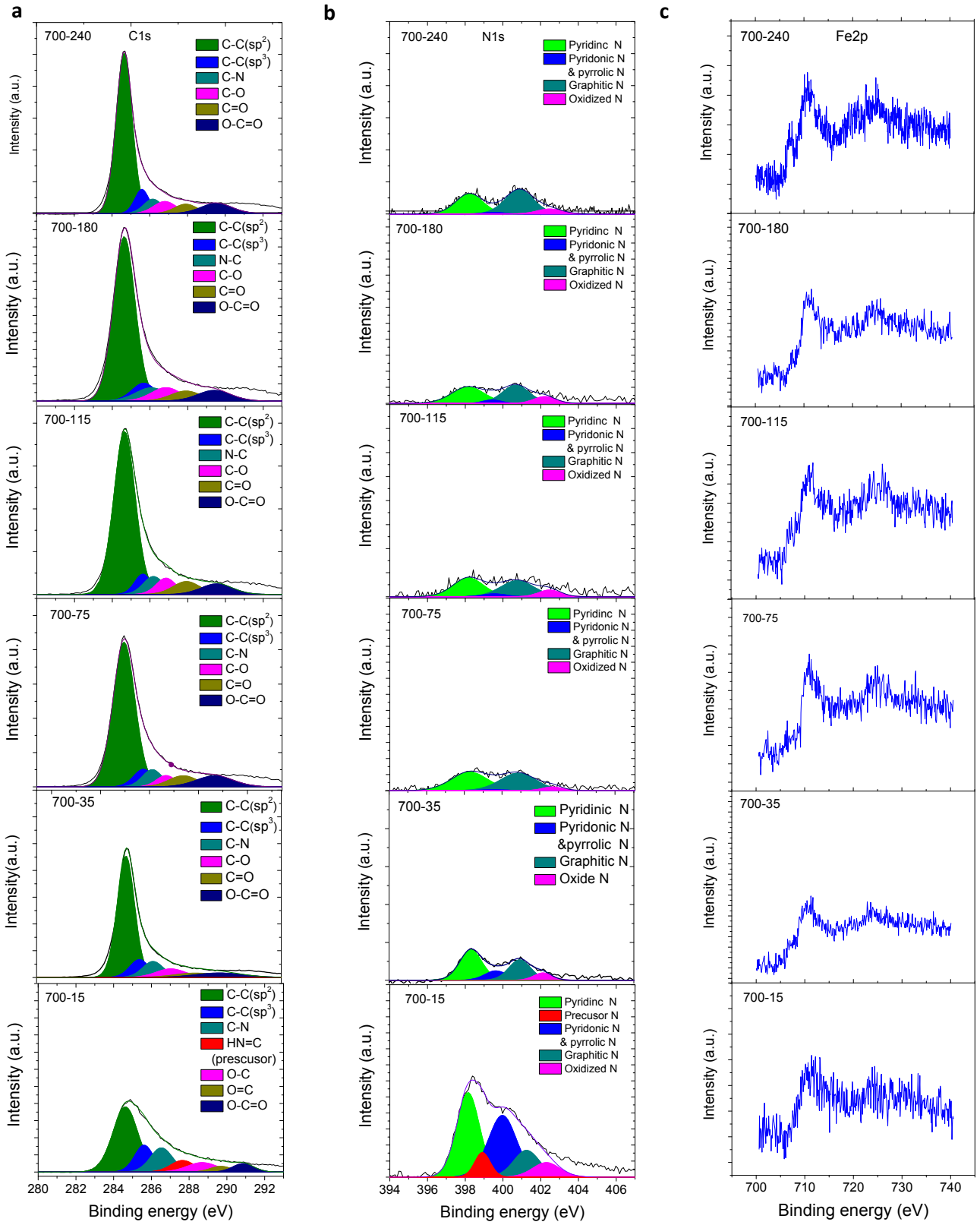

Figure 41. XPS spectra of G@Fe pyrolyzed at 15-240 minutes at 700 ^{o}C.

For the duration-dependent G@Fe samples, the overall trend of the surface XPS analysis is similar to the temperature-dependent samples. For 700-15, a small amount of the precursor N was confirmed by both C1s and N1s XPS spectra. When the duration was increased to 35 min (700-35), the precursor C and N vanished and the surface N content decreased significantly to 6.6 wt%. During the following prolong pyrolysis, the C and N XPS showed no significant changes though a slight decrease of the N content, from 4.1 wt% for 700-75 to 2.3 wt% for 700-240, was observed.

Similarly, all the Fe2p XPS disclosed very weak signals. Finally, the correlations between the surface Fe, N and C with temperatures and durations are shown in **Figure 42**. The trends are very close to that of bulk compositions (**Figure 39**). The G@Fe after complete decompositions of precursors shows the surface components 85-94 wt%C, 2-7 wt%N and 1-4 wt% Fe.

Table 4. Summary of Fe, C, N compositions of the G@Fe samples.

Catalysts	Fe (bulk)%	N (bulk)%	C (bulk)%	Fe (suf.)%	N (surf.)%	C (surf.)%	Yield%
600-35	6.5	41.1	49.2	4.4	42.3	50	45.5
700-15	9.1	22.1	63.0	1.1	20.2	71.8	32.5
700-35	12.7	11.3	68.1	3.8	6.6	85.6	26.7
700-75	12.9	5.0	73.9	3.0	4.1	88.6	26.7
700-115	13.8	4.7	75.6	2.9	3.0	91.1	27.1
700-180	13.8	4.2	76.2	3.2	2.9	90.2	24.2
700-240	13.9	4.1	74.5	1.9	2.3	92.0	24.0
800-35	12.6	2.1	79.6	1.1	2.1	94.0	25.0
850-35	12.8	1.6	80.1	1.3	1.9	92.0	24.2

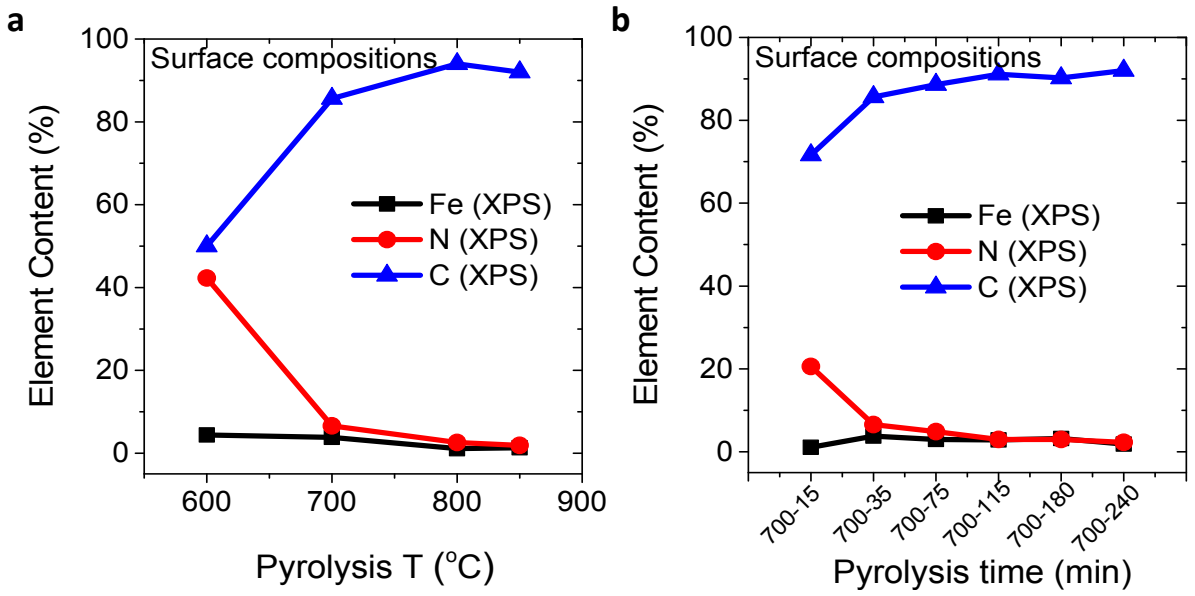

Figure 42. The contents of surface Fe, N, C from XPS quantitative analysis.

3.6. Catalysts Pyrolyzed from Nitrogen Free Precursors

To clarify the roles of surface nitrogen, we attempted to repeat the syntheses with the nitrogen-free precursors, ferrocene and durene for a comparison. **Figure 43**a&b show typical TEM images of the obtained powders of the N-free G@Fe at 700 and 800 °C, respectively. At 700 °C, there is no well-defined morphologies while the CNT dominated structure was observed in samples at 800 °C. XRD patterns of samples exhibited the primary metallic components of α-Fe (**Figure** 44).

The samples were then heat-treated a flowing ammonia atmosphere at 850 °C for 1h. It seems that both morphologies for N-free G@Fe were destroyed to some extent, as shown in the TEM images in **Figure 43**c&d. Likely due to this effect, the Fe containing phases disappeared in the XRD patterns and new peaks emerged likely due to formation of inorganic nitrides (Fe_4N) (**Figure 44**). The possible reason for the Fe_4N the formation is due to ammonia destroying the carbon structure, reaction of with iron particles. The resulted materials showed poor ORR activity (discussed in the next Chapter) indicating the importance of in-situ pyrolysis of precursors in the presence of N resources.

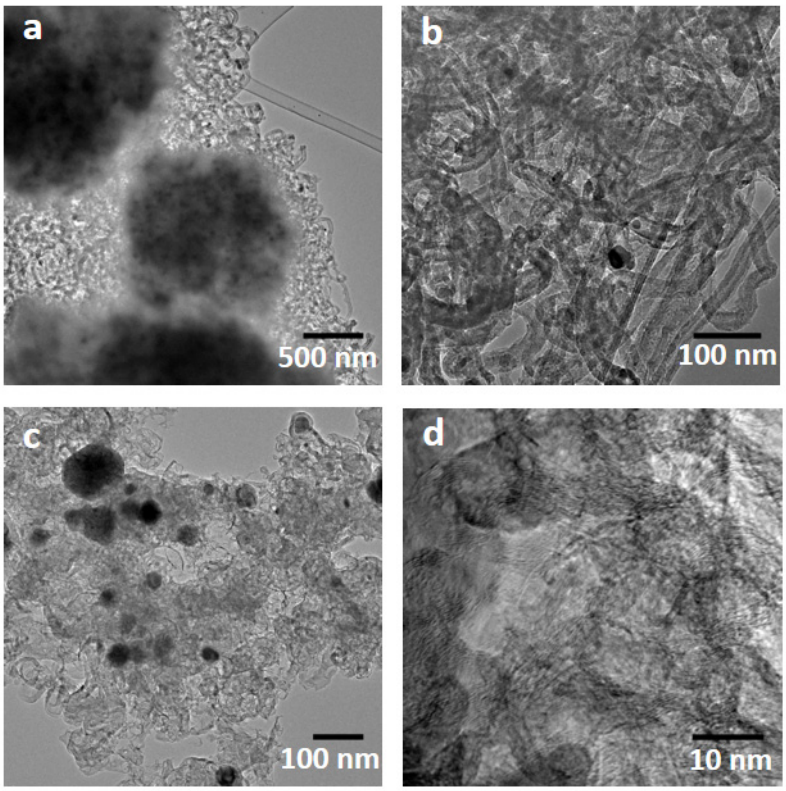

Figure 43. (a, b) Representative TEM images of catalysts pyrolyzed by nitrogen-free precursors. (c, d) TEM images of NH_3-treatment N-free catalyst samples.

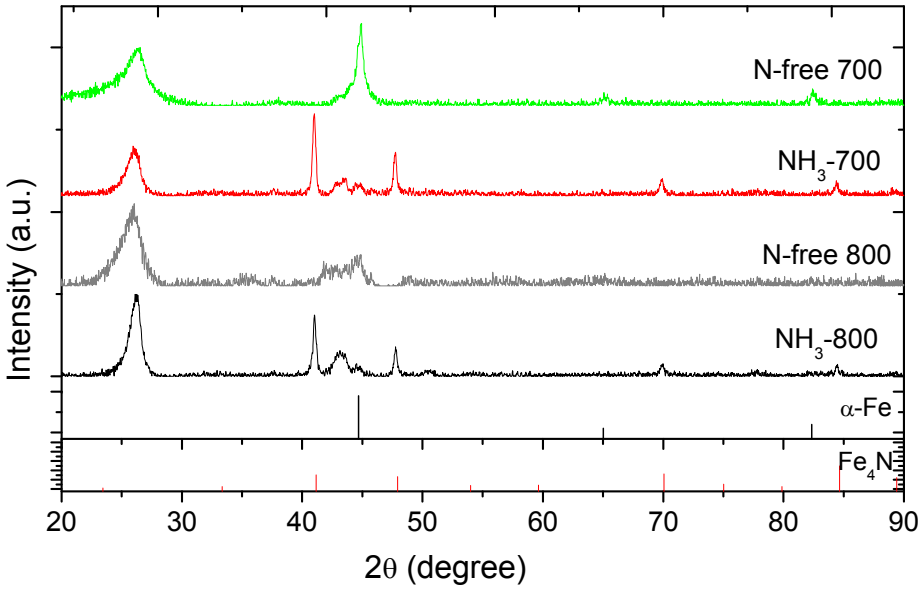

Figure 44. XRD for the N-free and NH_3-treated catalysts and corresponding comparison with standard Fe species.

3.7. Conclusions

Three series of G@Fe catalysts were prepared by the dry autoclave method in this Chapter:

a) Series one at fixed pyrolytic duration of 35 minutes but varied temperatures from 600, 700, 800 and 850 ^{o}C;
b) Series two at fixed pyrolytic temperature of 700 ^{o}C but varied durations of 15, 35, 75, 115, 180 and 240 minutes;
c) Series three at temperatures of 700 and 800 ^{o}C and duration of 35 minutes with N-free precursors.

The following are the conclusive remarks of the study in this Chapter.

1) Morphologies

Temperature effect (600-850 ^{0}C for 35 minus). Before 600 ^{o}C, cyanamide polymerized into melamine-rich spheres in the high pressure environment while ferrocene decomposed into amorphous species and dispersed evenly in the sphere. At 700 ^{o}C, the melamine phase decomposed gradually into nitrogen-rich carbon (C–N) species while the amorphous iron species developed into crystalline Fe containing nanoparticles, meanwhile the formation of graphitic layers, most likely catalyzed by the metallic phases and eventually encapsulating the uniformly distributed metal containing nanoparticles. High temperatures above 700 ^{o}C resulted in (i) smaller spheres and less regular in shape; (ii) crumpled spherical morphology, loose CNTs and encapsulated larger nanoparticles eventually at 850 ^{o}C. Overall, spherical morphology dominated at 600-800 ^{0}C while CNT morphology was resulted at high temperature of 850 ^{0}C.

Duration effect (15-240 minutes at 700 ^{o}C). For a short duration of 15 min, the Fe containing nanoparticle formed. Compared with lower temperature and even longer duration (600-35), 700 was further demonstrated as the cutting-off temperature for Fe containing nanoparticles formation. For further duration between 35-240 minutes, the morphology was dominated in the sphere and little morphological changed though slightly smaller in the sphere size.

High-resolution structure and element distribution. For the sphere dominated G@Fe (e.g, 700-75*),* carbon, nitrogen and iron were uniformly distributed throughout the whole spheres. For the CNT dominated G@Fe (e.g., 850-35), C and N were uniformly distributed while Fe nanoparticles locally concentrated in the center of CNTs. HRTEM demonstrated an encapsulated structure by a few carbon layers of which the thickness of the carbon layer was determined at ca. 2-4 nm.

2) Crystalline phases

At 600 ^{o}C (600-35), the main components are the polymeric melamine with some crystallinity. No Fe containing species were formed at this temperature. The graphitic carbon and Fe_3N were formed for 700-15. For 700-35, Fe_3N decomposed and the components were identified to graphitic carbon, α-Fe, γ-Fe and Fe_3C. At higher temperatures (800-35 and 850-35) or longer duration (35-240 minutes at 700 ^{o}C), similar components were resulted compared with 700-35. In addition, there is no apparent variation for the crystalline phases. Overall, XRD demonstrated that G@Fe was mainly constituted by graphitic carbon, two metallic Fe (α-Fe and γ-Fe) and Fe carbide (Fe_3C).

3) Solid yields and bulk compositions

About 25% yield of G@Fe was obtained after complete decomposition of precursors, of which is about 12-13 wt% iron, 68-80 wt% carbon and 2-11 wt% nitrogen with the rest balanced by oxygen and some hydrogen as well for the bulk compositions.

4) Surface functionalities

The surface functionalities of Fe, N and C were examined by the XPS measurements. *The C1s spectra* identified several types of components including C-C (sp^2, graphitic carbon), C-C(sp^3), C-N, C-O, C=O and O-C=O functional groups. The precursor carbon (e.g., HN=C) was detected in 600-35 and 700-15, which vanished at 700-35, in agreement with the XRD results. After complete decomposition, the surface carbon content maintains 85-94 wt% and the surface carbon layer is dominated by the graphitic structure (C-C, sp^2). *The N1s spectra* disclosed four main types of surface N components including pyridinic N, pyridonic and/or pyrrolic N, graphitic N and oxide N. Similar to the precursor carbon observed in C1s XPS of 600-35 and 700-15, precursor N was either observed in the N1s spectra in both samples. The surface N content after complete decomposition of precursors is around 2-7 wt% and the overall trend is a decrease of the surface N content with increasing the pyrolytic temperature and duration. The Fe2p spectra for all samples are clearly visible but with very weak intensity by considering a fact that, its bulk content is as high as 12-13 wt%. This may indicate the encapsulated structure.

5) N-free G@Fe samples

The N-free G@Fe was synthesized by ferrocene and durene at both 700 and 800 ^{o}C. There were no well-defined morphologies for the N-free G@Fe or even after post N-doping by the NH_3 treatment. XRD demonstrated that the reduced state α-Fe was the main Fe component and inorganic nitrides (Fe_4N) might be formed after the NH_3 treatment. This result suggests that the N resource of cyanmide play an important role for producing the specific encapsulated nanostructured G@Fe.

Chapter 4

Mössbauer Spectra and Electrochemical Evaluation

This chapter is a continuation of characterization of the three series of catalysts prepared in Chapter 3. ^{57}Fe-Mössbauer spectroscopy is used to distinguish and quantify different iron phases in G@Fe catalysts. The iron-containing components include α-Fe, γ-Fe, γ-Fe_2O_3, and Fe_3C as well as a minor coordinated component, most likely corresponding to the well identified FeN_x/C species in literature. The catalytic activities and mechanisms for ORR are evaluated by RDE and RRDE. The optimized catalysts were obtained from pyrolysis at 700 ^{o}C and 75 min, which exhibited a high onset potential of 0.85 V at 0.1 mA cm^{-2} and stability of a 25 mV shift after 10,000 potential cycles in acidic media. In terms of the mass specific kinetic current density, the electrochemical activity is found to be positively correlated with the Fe_3C content as well as with the assumed FeN_x/C content.

4.1. Introduction

The three series of catalysts were characterized in terms of morphology, XRD, XPS, solid yield and bulk compositions, as discussed in Chapter 3. This chapter is devoted to the further identification and quantitative determination of metal phases by Mössbauer spectra, a special tool for investigation of the valence state of iron and the type of coordination polyhedron occupied by iron atoms. In combination with the Mössbauer spectroscopy, the electrochemical activity of the materials towards the ORR is systematically evaluated. Finally, an attempt was made to correlate

the electrochemical performance of the catalysts with the content of varied iron containing phases for exploration of the active sites of the catalysts.

4.2. Experimental

^{57}Fe Mössbauer spectra were measured at both room temperature (295 K) and low temperature (18 K) using a ^{57}Co source embedded in a rhodium matrix and a constant accelerator spectrometer. The isomer shifts were given relative to that of α-Fe at room temperature. The samples for Mössbauer spectroscopy were prepared by pressing ca. 100 mg of the sample powder into pill-shapes with 15 mm in diameter and 2 mm thick.

Electrochemical measurements. Electrochemical tests were carried out in a standard three-electrode cell. A glassy carbon disk substrate of diameter 5.0 mm and a carbon rod were used as the working and counter electrode, respectively. The reference electrode was a saturated calomel electrode (SCE). The measured potentials between the working and the reference electrodes were throughout this thesis converted into values versus the reversible hydrogen electrode (RHE) afterward. All the electrochemical experiments were performed using a Versa STAT3 (Princeton Applied Research) and 760C Bipotentiostat (CH Instruments) in N_2 or O_2-saturated 0.1 M $HClO_4$ solution with a potential range between 1.15 V and 0.05 V vs RHE at a scan rate of 10 mV s^{-1}.

Catalyst ink was prepared by dispersing 10 mg of catalysts into a mixed solution of 514 µL ethanol and 80 µL of 5% Nafion. The commercial Johnson Matthey 20% Pt/C on Vulcan 72R support was chosen as the contrast catalyst. An ink was prepared by dispersing 5 mg 20% Pt/C in a solvent containing 400 µL Mill-Q water, 600 µl ethanol and 50 µl 5% Nafion. All inks were dispersed by mean of the ultrasonic bath for 3h in order to obtain a good dispersion. The catalyst-coated electrode was obtained by dispersing the catalyst ink on the glassy carbon rotating disk electrode (RDE) or rotating ring-disk electrode (RRDE) followed by drying in air. The catalyst loading of the Pt/C catalysts for RDE was 0.25 mg cm^{-2}. The catalyst loading of G@Fe for both RDE and RRDE was 0.65 mg cm^{-2}.

4.3. Mössbauer Spectra and the Assignment

The ^{57}Fe-Mössbauer spectra were recorded at both room temperature (295 K) and low temperature (18 K). Mössbauer spectra for typical samples (700-35, 700-75, and 700-240) are shown in **Figure 45** and the rests are represented in **Figure 46**.

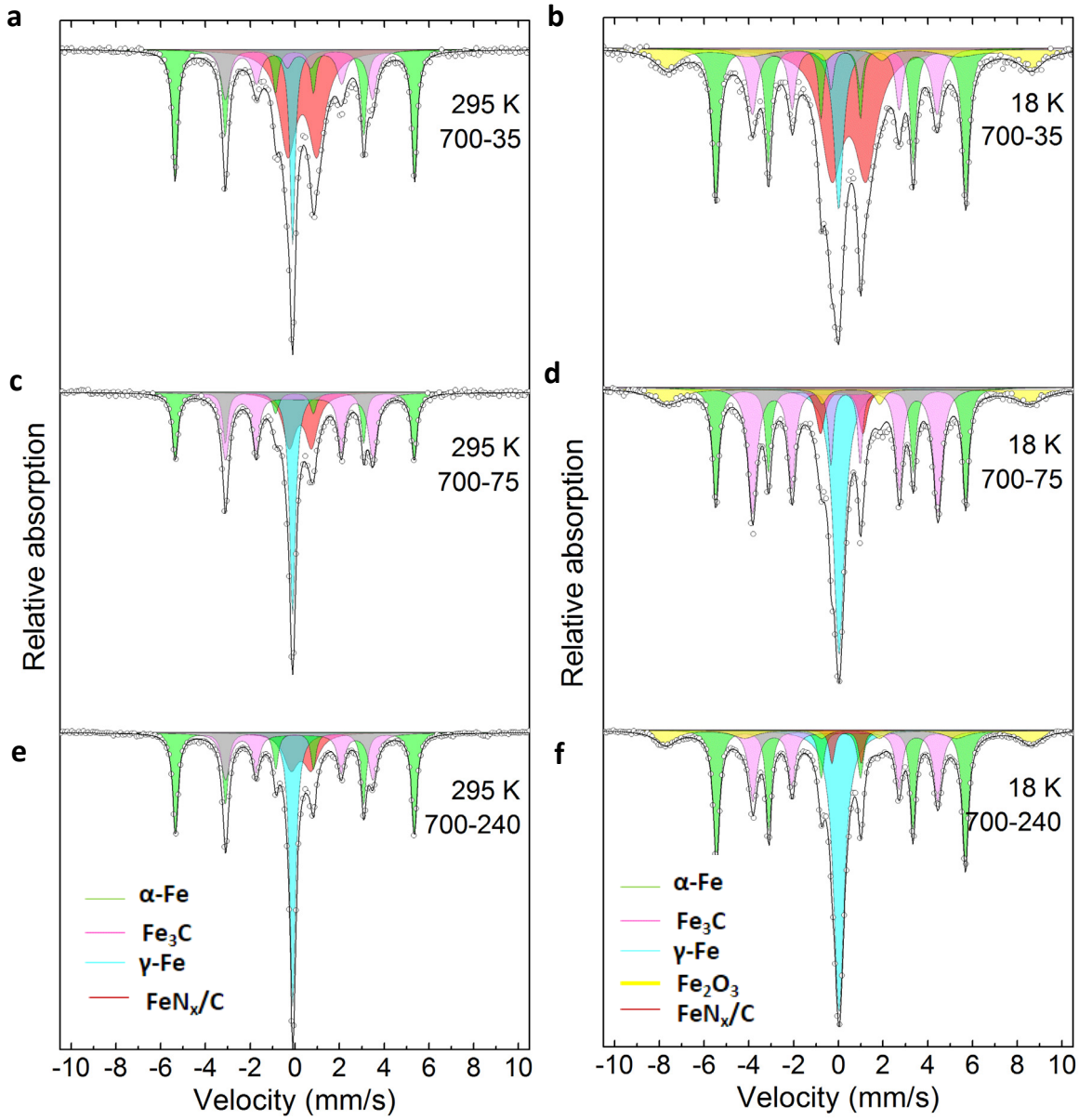

Figure 45. Representative ^{57}Mössbauer spectra for three G@Fe catalyst samples obtained at 298 K and 18 K.

The spectra were fitted with sextets and doublets, and the parameters, estimated at 18 K and 295 K from the spectra of 700-35, 700-75, and 700-240, are given in Table 5. More details are shown in Appendix Table 1. Because of the strong overlap of the spectroscopic lines, it was necessary to make some constraints of the parameters. For the sextet fit, the line widths and the line intensities were constrained to be pairwise identical and the relative areas were constrained to be 3:2:1:1:2:3. In the fits of the doublets, the widths and intensities of the two lines were constrained to be identical. The parameters of sextet 1 are in accordance with those of α-Fe[95,96] both at 18 K and 295 K and the parameters of sextet 2 are in accordance with those of Fe_3C.[95,97] The isomer shift and the magnetic hyperfine field of sextet 3 show that this component can be assigned to Fe^{3+}. Similar components are found in samples of Fe nanoparticles that have been exposed to air and these components have been assigned to a passivation layer consisting of poorly crystalline maghemite (γ-Fe_2O_3).[98,99] At 295 K this sextet has disappeared, presumably because it has transformed to a quadrupole doublet because of fast superparamagnetic relaxation. The singlet component is assumed to be due to γ-Fe[95], which is paramagnetic at room temperature but antiferromagnetic with a very small magnetic hyperfine field at low temperatures. This small hyperfine field explains the increased line width at 18 K.

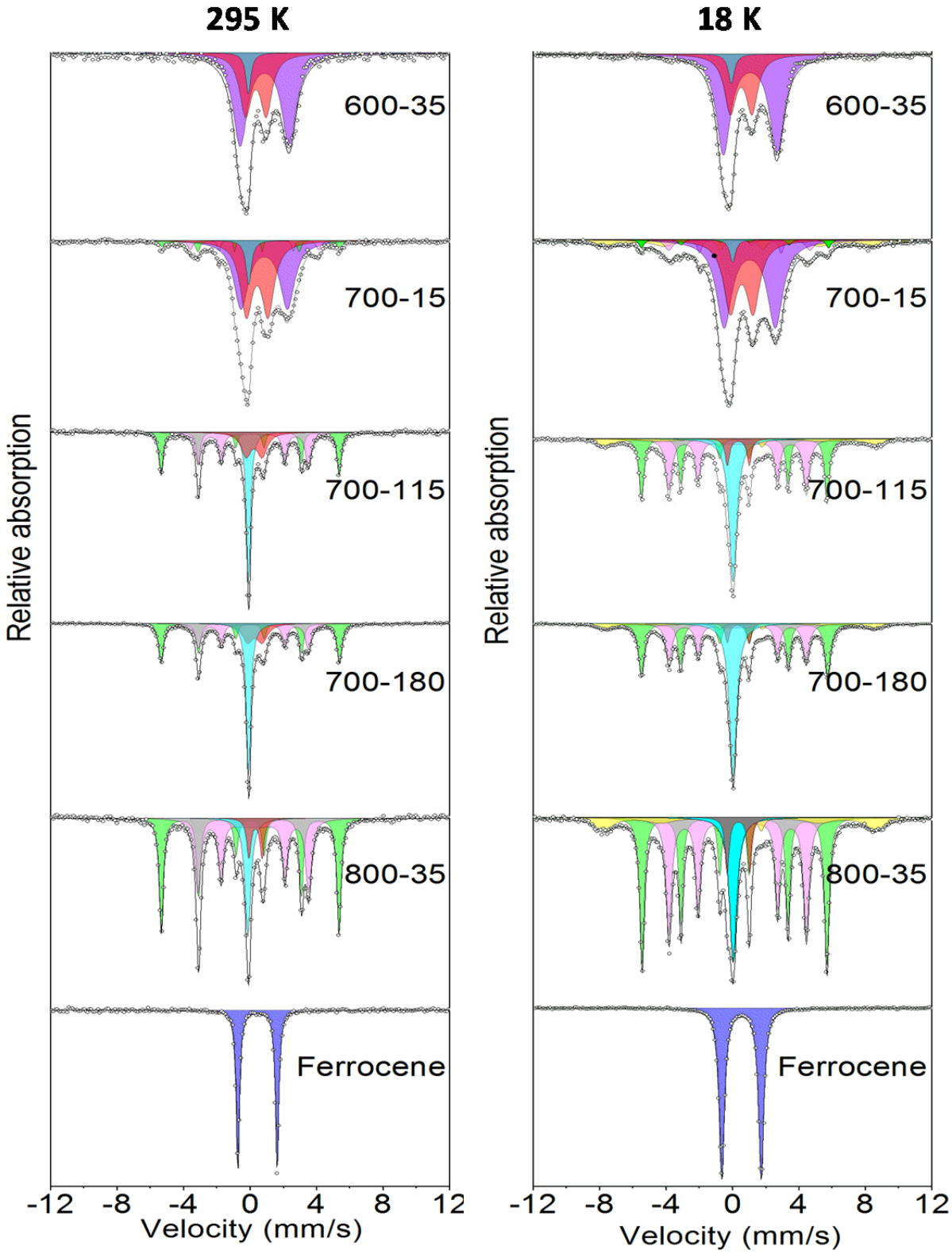

Figure 46. [57]**Mössbauer spectra at 298 K and 18 K for G@Fe samples obtained under varied pyrolytic conditions as indicated in the Figure. The precursor ferrocene is also included for a comparison.**

Table 5. Mössbauer parameters and assignments at 298 K and 18 K for the spectra of samples 700-35, 700-75, and 700-240.

Components	T K	B_{hf} T	δ mms^{-1}	ε mm s^{-1}	Δ mm s^{-1}	FWHM mm s^{-1}	Assignment
Sextet-1	295	33.1-33.2	-0.01-0.00	0.00		0.29-0.32	α-Fe[95,96]
	18	34.1-34.6	0.11-0.12	0.00		0.32-0.34	
Sextet-2	295	20.4-20.6	0.18-0.19	0.01-0.02		0.45-0.65	Fe_3C[95,97]
	18	25.2-25.7	0.31-0.32	0.00		0.44-0.47	
Sextet-3	295		-		-	-	Fe_2O_3[98,99]
	18	50.2-50.6	0.43-0.55	-0.10-0.02	-0.053	1.10-1.75	
Doublet	295		0.25-0.34		0.91-1.30	0.57-0.87	FeNx/C[96, 97,100,101]
	18		0.28-0.36		1.25-1.51	0.18-1.14	
Singlet	295		-0.09-0.10		-	0.31-0.32	γ-Fe[95]
	18		0.00-0.04		-	0.46-0.58	

B_{hf} is the magnetic hyperfine field. δ is the isomer shift. ε is the quadrupole splitting in the sextets. Δ is the quadrupole splitting of the doublets and FWHM is the line width of lines 1 and 6 in the sextets and the line width of the lines in the doublets and the singlet. The data for other G@Fe catalysts are shown in Appendix Tables 1 and 2.

One doublet (purple color in **Figure 46**) with δ_{iso} of 0.63 mm s^{-1} and high ΔE_Q of 3.00 was only observed in 600-35 and 700-15, which is attributed to formation of intermediates from the decomposition of precursors.[102] The very high content (66%) of this component for 600-35 and its disappearance at higher temperatures (e.g. 700-35) seem supporting this assignment. In the following discussion, this is denoted as Fe-Im.

Another doublet exhibits δ_{iso} of 0.26 mm s^{-1} and ΔE_Q of 1.00 mm s^{-1} for 700-75 (Table 5). For other samples from 700-115 to 800-35 (except for 700-15 and 700-35), δ_{iso} and ΔE_Q are concentrated at 0.23-0.30 mm s^{-1} and 0.89-1.00 mm s^{-1} (Table 5). The isomer shifts and quadrupole splitting indicate that it is due to Fe^{3+} in the high spin (HS) state and/or Fe^{2+} in the low spin (LS) state. However, these values are very close to the well-recognized $Fe^{2+}N_4/C$ (low spin, LS) in literature for the FeN_x/C type of catalysts[96,97,100,101]. Small shifts of δ_{iso} and ΔE_Q in different samples must result from their electronic environments.

There are more assignments for similar doublet configurations in literature but they do not seem to be relevant to the present discussion because of the large difference in ΔE_Q, for example, molecular (or distorted) iron phthalocyanine (FePc) ($Fe^{2+}N_4$, ΔE_Q>2.6 mm s^{-1})[103-106], molecular FePc ($Fe^{3+}N_4$, ΔE_Q<0.5 mm s^{-1})[103], $Fe^{3+}N_4$ (immediate spin (MS) with axial ligands, ΔE_Q~3.9 mm s^{-1}), C-Fe-N_2 (ΔE_Q>1.6 mm s^{-1})[104,105], $Fe^{2+}N_{2+2}$/C (MS, ΔE_Q>2.4 mm s^{-1}) and N-$Fe^{2+}N_{2+2}$…N_{prot}/C (high spin(HS), ΔE_Q>2.2 mm s^{-1})[107] . This doublet of the present work cannot either be assigned to Fe nitrides as suggested in literature [105-108]. A possible interruption might be a ferric iron porphyrin (oxygenated hemi) associated with CN^- ligand, denoted as oxygenated $Fe^{3+}N_4$-CN. This structure was reported in the early study of the Mössbauer effect of hemoglobin in NaCN/HCl solution (δ_{iso} of 0.17 mm s^{-1} and ΔE_Q of 1.39 mm s^{-1}, 195K)[109]. However, this CN^- ligand association occurs at room temperature. During the pyrolysis of the present work, CN^- should be decomposed at such high temperatures, which seems to be confirmed by the C1s and N1s XPS results where no C≡N bonds were observed (**Figures 40** and **41**). In brief, this doublet, associated with Fe^{2+} in the low spin (LS) state, is suggested, to be a species similar to the literature recognized FeN_x/C without further specification.

Herein, it should be noted for 700-15/700-35 samples that the doublet showed δ_{iso} of 0.43/0.30 mm $s^{-1}$and ΔE_Q of 1.32/1.24 mm s^{-1}, higher than the above average values (**Table 5**). These differences might be attributed to the formation of Fe-Im (44% precursor for 700-15) and the highly N-doped carbon. Another possible reason could be the presence of the crystalline Fe_3N phase, as identified in the XRD for sample 700-15 in **Figure 38**b. The Fe_3N often exhibits a sextet on Mössbauer spectra at both room and low temperatures. The doublet combined with weak sextet was also observed by reduction of hematite nanoparticles in NH_3 with high δ_{iso}.[110] These two additional components, the formed intermediates and iron nitrides, might be the reason for these relatively high δ_{iso} and ΔE_Q values.

4.4. Quantitative Analysis of Iron Components

As a summary of the long discussion above, six types of Fe components are assigned including α-Fe, γ-Fe, Fe_3C, Fe_2O_3, Fe-Im (precursor/intermediates) and most likely FeN_x/C. The relative amounts of iron in different phases were then calculated from Mössbauer spectra obtained at 18 K.

Figure 47 shows the relationships between the content of various iron components, expressed at percents of the total iron amount, and the pyrolysis temperature (a) and duration (b). In **Figure** 47 the reduced Fe forms (α-Fe and γ-Fe) are steadily increasing with the pyrolytic time from 15 to

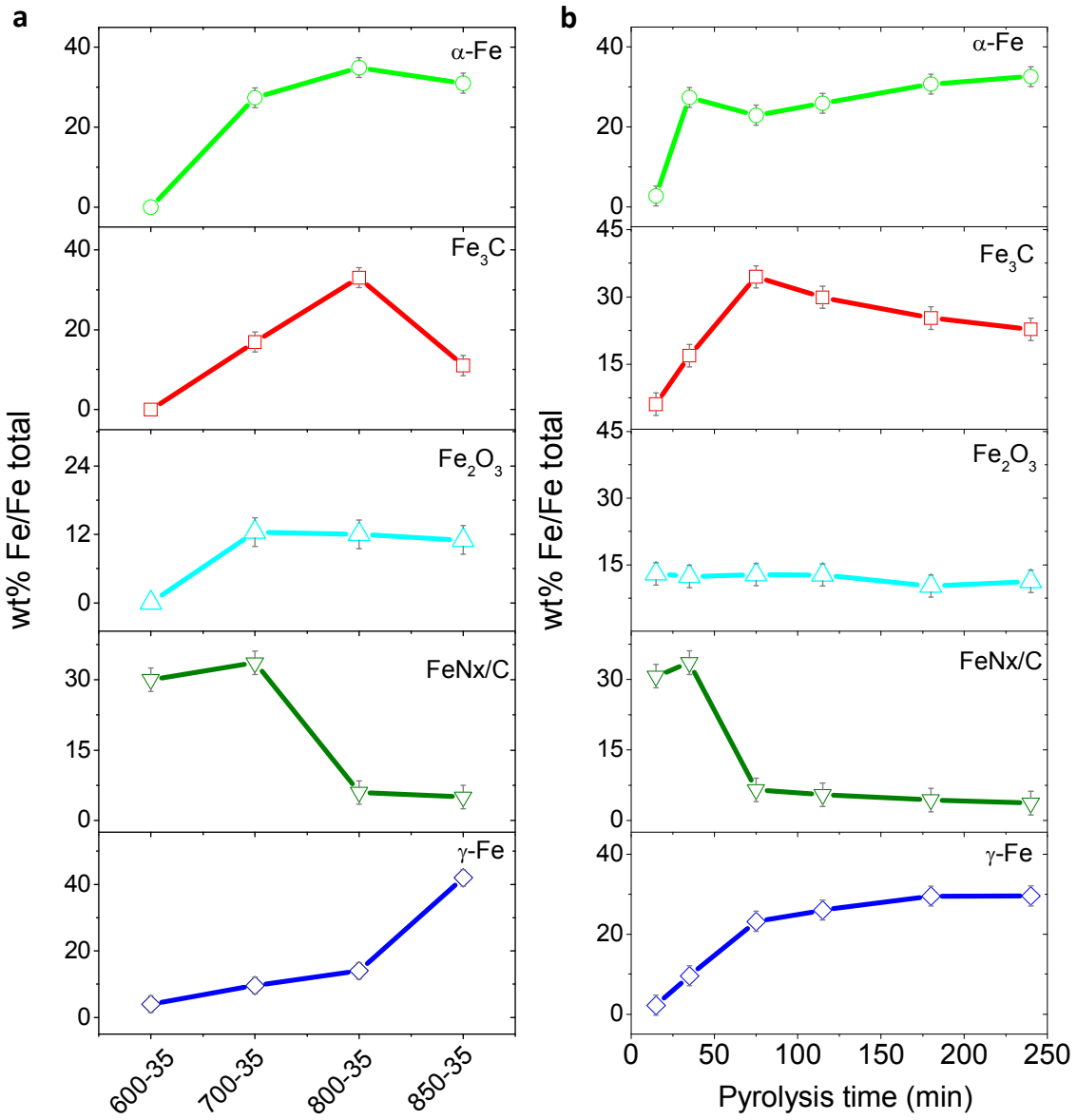

Figure 47. The Fe content of various Fe components in G@Fe obtained from low temperature Mössbauer spectra (18 K). (a) Content of Fe components for the temperature series sample (600-850 ^{o}C, 35min). (b) Content of Fe components for the duration series sample (15-240 min, 700 ^{o}C).

240 mins at 700^{o}C as well as with pyrolytic temperatures. The content of the FeN_x/C phase, as obtained from the 18 K spectra, was found to quickly decrease as the pyrolytic duration increases from 35 min at 700 ^{o}C. When the duration is longer than 75 min at 700 ^{o}C or even 35 min at 800 or 850 ^{o}C, the content of this phase was found to be stabilized at a very low value, around 3-6% of the total Fe.

It is of special interest that the Fe_3C content was found to peak at the pyrolytic time of 700-75 and 800-35 with fast increase before and slow decrease after this point. This suggests a fast

formation of the carbide phase, followed by a slow decomposition either at a higher temperature or during the prolonged pyrolysis.

Overall, the content of various Fe components appears to follow the following trend: (1) the content of the reduced Fe (α-Fe and γ-Fe) component steadily increases with the time and temperature, reaching in sum about 60% of the total iron amount; (2) as long as the N-containing precursor is completely decomposed, the content of the iron-nitrogen coordination is stabilized at about 3-6%, (3) the content of Fe_2O_3, either formed inside the autoclave due to the trace of oxygen/water or formed during the storage of the catalysts in air after synthesis, is almost constant at ca. 12-13%, (4) the Fe_3C shows a peak content at 700-75 or 800-35, apparently with a fast initial formation followed by slow decomposition at higher temperature or during the prolonged pyrolysis.

4.5. Electrochemical ORR Activity Evaluation

A number of NPMCs and metal-free catalysts have been reported with comparable ORR activities with Pt/C in alkaline medium. The challenge remains in acid electrolytes in which the prepared G@Fe catalysts were characterized in the present work.

4.5.1. Effects of Pyrolytic Temperatures and Durations

Two sets of RDE polarization curves are shown in **Figure 48**, one is for samples obtained at different pyrolysis temperatures for a duration of 35 minutes (a, b) and the other is for samples obtained at 700 ^{o}C for varied durations (c,d). The samples pyrolyzed at 600 ^{o}C with little formation of functionality sites showed no ORR activities, while a prominent enhancement was observed for sample 700-35. The half-wave potential ($E_{1/2}$) increased with the pyrolytic temperature peaked for sample 800-35 in the order of 600-35 < 850-35 < 700-35 < 800-35 as seen from **Figure 48**a-b.

For the series of samples prepared at 700 ^{o}C for different durations, **Figure 48**c, 700-15 showed a limited activity though much better than that of 600-35. This is in agreement with the characterizations that are the incomplete decomposition of precursors. With the increase of the pyrolytic duration, the ORR activity was found to improve in the order of 700-15 < 700-35 < 700-115 > 700-180 > 700-240 > 700-75 (**Figure 48d**). The 700-75 sample exhibited the highest onset potential of 0.83 V (at 0.1 mA cm^{-2}), which was further increased to 0.85 V at higher catalyst loadings (1.03 mg cm^{-2}, **Figure 49**). This result is very close to the recently reported encapsulated

Fe based metal organic frameworks (FePhen-MOF) in acid media[45] where an onset potential of ca. 0.88 V at 0.1 mA cm^{-2} was reported with a catalyst loading about doubled as much of the present study.

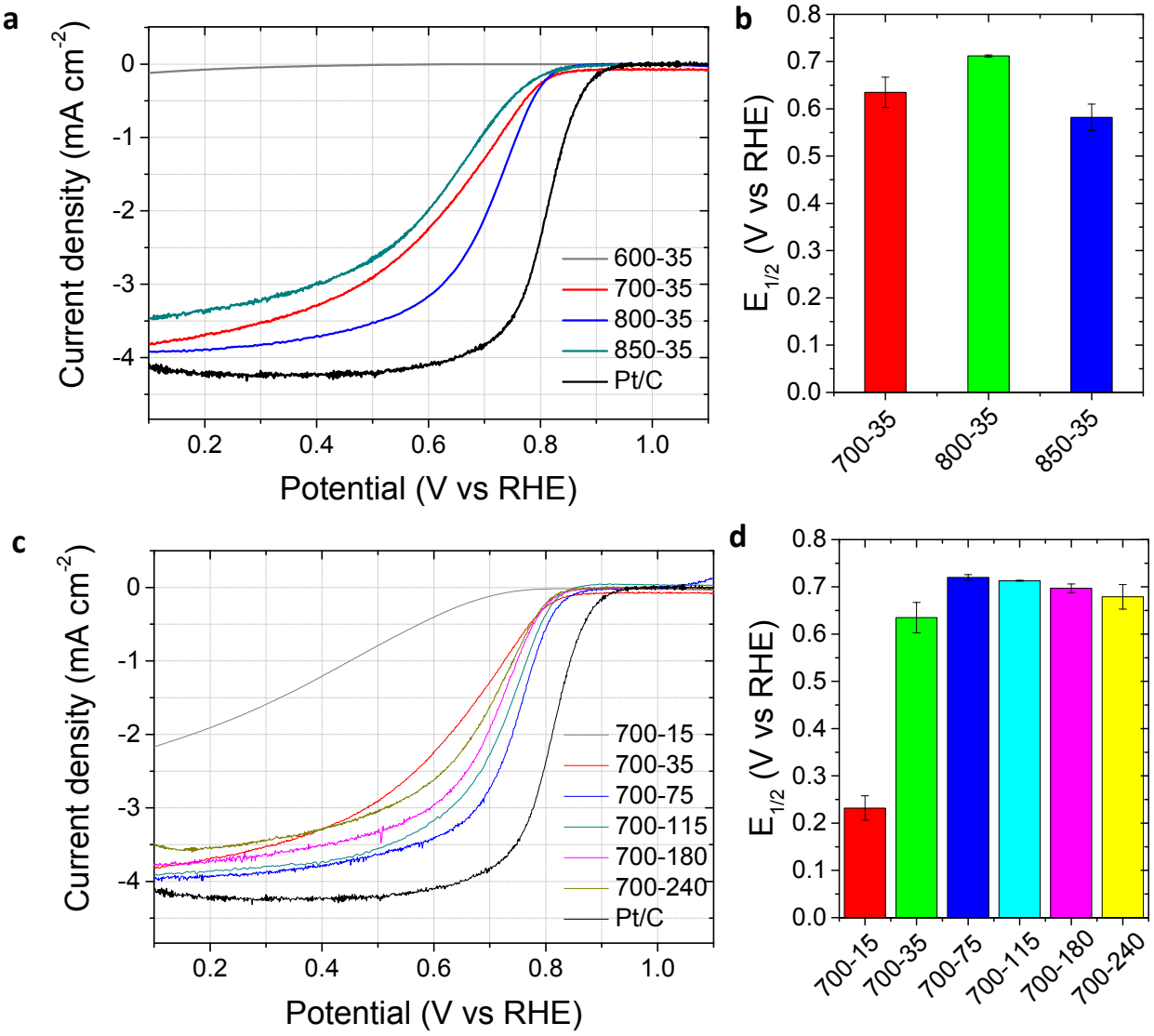

Figure 48. RDE polarization curves for G@Fe catalysts in O_2-saturated 0.1 M $HClO_4$ solution. Catalysts loading: 0.65 mg cm^{-2}. The rotating speed: 900 rpm. (a, b) samples obtained at different pyrolysis temperatures as indicated in the Figure for a duration of 35 minutes; (c, d) samples obtained at 700 ^oC for the varied duration as indicated in the Figure. The commercial (Johnson Matthey) 20 %Pt/C was used as a reference with a loading of 0.25 mg cm^{-2}.

4.5.2. Loading Effect of the Catalysts

Figure 49 shows the loading effect. The ink and film qualities are essential for the RDE test, particularly at high loadings of the catalysts. For carbon supported platinum catalysts, the Nafion

content, the catalyst or the carbon black loading have a great impact on the accuracy of kinetic current calculation in the RDE measurements, because the Koutecky−Levich equation is essentially based on smooth electrode surfaces under laminar flow hydrodynamics. With higher catalyst loadings, the mass-transport resistance through the film is increased and incomplete utilization of the catalyst applies. As seen from **Figure 49**, in the range of the catalyst loading from 0.39 to 1.03 mg cm^{-2}, a steady increase in the total current is observed, though the increase is much slower at higher loadings and the limiting currents are changing slightly. For later discussion on the catalyst performance, data from the catalyst loading of 0.65 mg cm^{-2} are used.

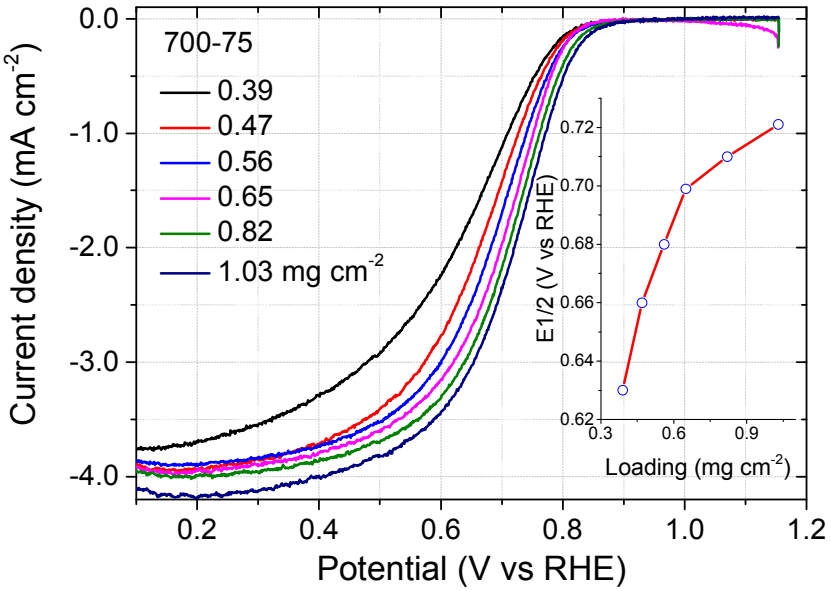

Figure 49. RDE polarization curves for 700-75 catalyst at different mass loadings in the O_2-saturated 0.1 M $HClO_4$. Scan rate 10 mv s^{-1}, rotating speed 900 rpm.

4.5.3. N-free Catalysts and the Post Ammonia Treatment

To clarify the roles of surface nitrogen, an attempt was made to pyrolyze the nitrogen-free precursors of ferrocene and durene for a comparison, as described in the last Chapter. Such materials showed some, though poor, ORR activity in acidic electrolytes (**Figure 50**). The samples from pyrolysis at 700 and 800 ^{o}C exhibited an onset potential of 0.6 and 0.55 V vs RHE, respectively. This is a clear indication that, without nitrogen functionalities, likely in form of N-doped carbon, the encapsulated metal particles possess the low ORR catalytic activity.

The samples were then heat-treated under a flowing ammonia atmosphere at 850 °C. The ammonia-treated powders showed enhanced ORR activity. The resulted materials showed an increase in the onset potential, which was about 0.62-0.68 V. though still far lower than that of 700-75 (0.83-0.85 V), the catalyst obtained from pyrolysis of ferrocene and cyanamide. The doping of nitrogen may primarily happen on the surface carbon atoms forming N_xC sites. At the same time, the N-doping may destroy the encapsulating carbon layers, resulting in direct reaction of ammonia with the originally encapsulated iron particles and therefore the formation of additional FeN_x functionalities. Considering the significant difference of the morphologies in terms of the encapsulating carbon layers and metal-containing nanoparticles, this result may hint the importance of the nitrogen as well as the catalyst structure.

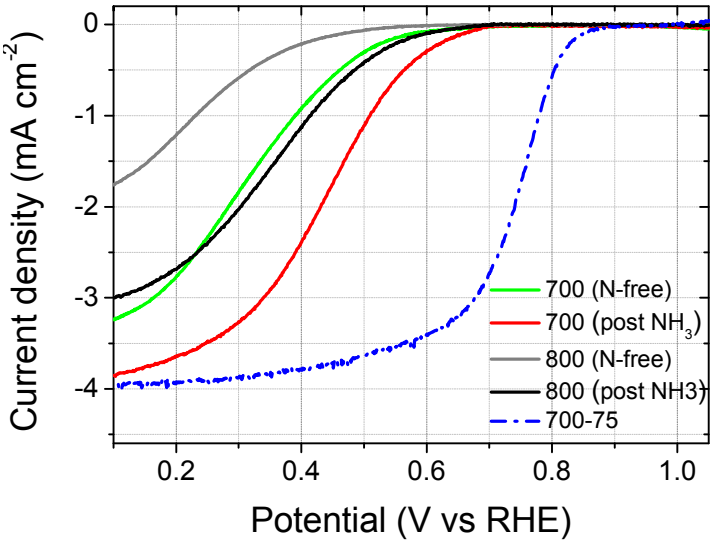

Figure 50. RDE polarization curves for the G@Fe catalysts prepared from N-free precursors at 700 and 800 °C, indicated as 700 (N-free) and 800 (N-free) in the Figure. The catalysts after post NH_3 treatment are indicated as 700 (post-NH_3) and 800 (post-NH_3). The catalyst obtained from pyrolysis of ferrocene and cyanamide at 700 °C for 75 minutes is also shown for comparison (700-75).

4.5.4. Summary of Electrochemical Performances

In terms of the Tafel slope, the 700-75 sample displayed a value of 72.4 mV dec^{-1}, which is comparable to 69.5 mV dec^{-1} for the commercial 20% Pt/C catalyst (**Figure 51**). Three to five independent measurements of polarization curves on each type of catalysts were made and the average data are listed in Table 6, which was 69.3 mV dec^{-1} for sample 700-75.

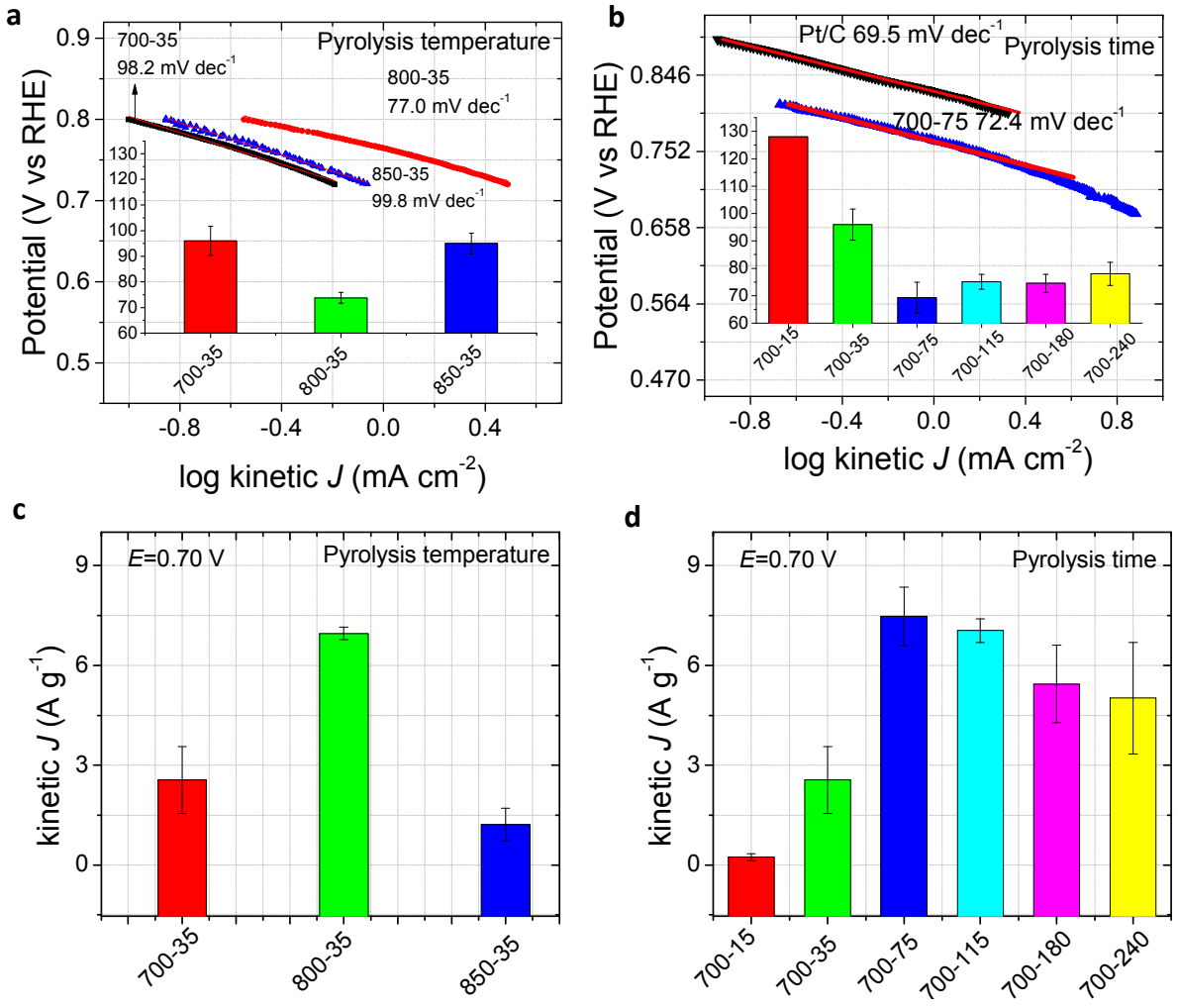

Figure 51. (a) Comparison of Tafel slopes for 700-75 G@Fe and 20% Pt/C. The inset shows Tafel slopes for all G@Fe catalysts. (b) Comparison of kinetic current density (J_k) at the potential of 0.70 V vs. RHE for all G@Fe catalysts.

In terms of mass specific kinetic current (J_K), obtained within the kinetically dominated potential region of 0.75-0.65 V, the catalyst activities are plotted in **Figure 51** as a function of pyrolytic temperature (a) and duration (b). For a pyrolysis duration of 35 minutes, the sample at 800 ^{o}C (800-35) showed the best performance while at fixed temperature of 700 ^{o}C, the pyrolysis for 75 minutes gives a peak kinetic current density.

4.5.5. H_2O_2 Yield, Electron Transfer Number, and Stability Tests

Rotating-ring-disk-electrode (RRDE) measurements were further performed, as shown in **Figure 52** and **Figure 53**. The generation of H_2O_2 is varied to a great extent for the samples, however, samples very the best catalytic activities, i.e. 700-75 and 800-35, showed a very low H_2O_2 yield of ca. 3.5%,

corresponding to an electron transfer number of 3.9, as seen from Figure 53. In addition, the stability was evaluated by potential cycling between 1.1 -0.6 V vs. RHE at a scan rate of 10 mV s^{-1} and found to have a small degradation by 25 mV shifts of the $E_{1/2}$ after 10,000 cycles (**Figure 54**). Compared with recent literatures of similar encapsulated structures[40,42-46], the present catalysts show relatively high activity and excellent stability in acid media.

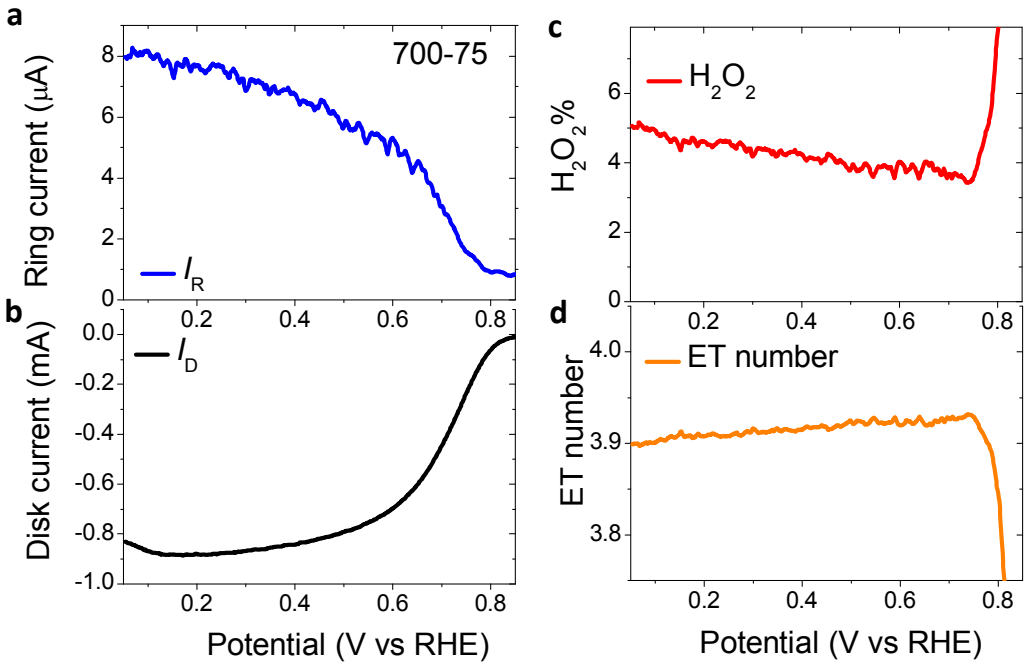

Figure 52. (a, b) RRDE Tests of representative 700-75 catalysts. (c, d) The H_2O_2 yield and ET number for G@Fe determined from RRDE tests. RRDE results for other G@Fe catalysts are shown in Appendix Figure 2. All RRDE curves were calibrated by subtracting the background current in N_2-saturated solution. The scan rates for all electrochemical tests were 10 mV s^{-1}.

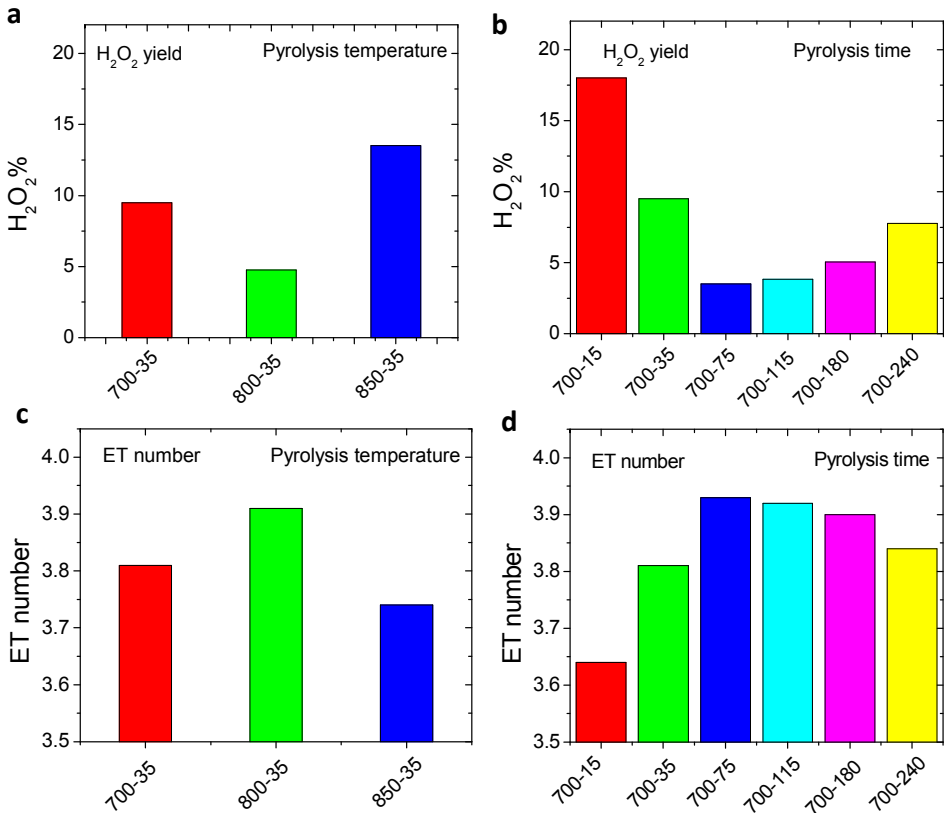

Figure 53. The H_2O_2 yield and electron transfer (ET) number for all G@Fe determined from RRDE tests.

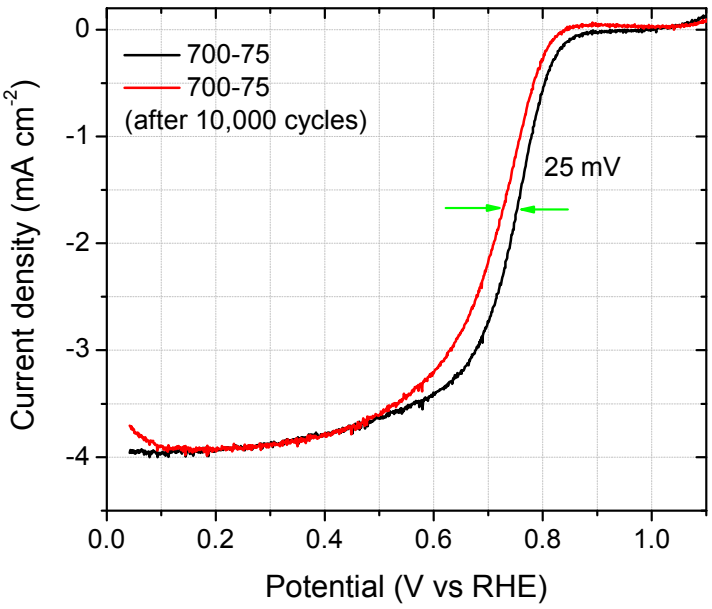

Figure 54. Stability test for the 700-75 G@Fe catalyst before and after 10,000 potential cycles at a scan rate of 10 mV s^{-1} under 900rpm in O_2-saturated 0.1M $HClO_4$ solution. Potential cycling was performed between 0.6 and 1.0 V in N_2-satureated 0.1M $HClO_4$ solution.

Table 6. Summary of contents of various Fe components (from ^{57}Mössbauer spectra at 18 K) and average electrochemical ORR activities. It should be remarked that the iron component contents are based on the total iron amount in the catalysts (not the total mass of the catalysts as sloid powders).

Samples	α-Fe	Fe_3C	Fe_2O_3	Fe-Im	FeN_x/C	γ-Fe	$^{a}E_{onset}$ (V)	$E_{1/2}$ (V)	Tafel(mV dec^{-1})	J_K(0.75V) (A g^{-1})	J_K(0.70V) (A g^{-1})	J_K(0.65V) (A g^{-1})	H_2O_2%	ET No.
600-35	0	0	0	66	30	4	-	-	-	-	-	-	-	-
700-15	3	6	13	45	30	2	0.720±0.025	0.232±0.026	121±13.1	0.11±0.05	0.24±0.1	0.46±0.16	18.0	3.64
700-35	27	17	12	-	34	10	0.828±0.020	0.635±0.032	95.9±11.0	1.10±0.43	2.56±1.01	4.97±1.92	9.5	3.81
700-75	23	35	13	-	6	23	0.826±0.007	0.720±0.006	69.3±5.6	2.65±0.48	7.84±0.97	16.78±0.84	3.5	3.93
700-115	26	30	12	-	6	26	0.832±0.003	0.713±0.001	75.1±0.8	2.55±0.22	7.05±0.35	14.91±0.22	3.8	3.92
700-180	31	25	10	-	4	30	0.827±0.011	0.697±0.009	74.6±3.3	2.00±0.53	5.44±1.16	11.42±1.73	4.8	3.90
700-240	33	23	11	-	3	30	0.823±0.015	0.679±0.026	78.0±4.2	2.06±0.77	5.01±1.68	8.98±2.71	5.1	3.84
800-35	35	33	12	-	6	14	0.827±0.002	0.712±0.002	73.8±2.1	2.38±0.10	6.96±0.19	15.23±0.94	7.8	3.91
850-35	31	11	11	-	5	42	0.787±0.017	0.582±0.028	98.1±3.8	0.30±0.12	0.79±0.32	1.80±0.75	13.5	3.74

4.6. Identification of ORR Active Sites

The Mössbauer spectra have unveiled various Fe components and their contents of G@Fe whose electrochemical ORR activities were also evaluated. An attempt is now made to establish the correlation of the catalyst composition and electrochemical activity. Here the Fe content is the total amount of the specific iron component in the catalyst samples, expressed as wt % of the total catalyst, as obtained from the Mössbauer and ICP-MS analysis.

Figure 55a shows the Fe_3C content and the corresponding mass specific current density J_K for the ORR for individual catalyst sample of both the 35 minute and 700 ^oC series. It is clearly seen that the two parameters follow the same trends and peaks in the graph. The J_K is further plotted against the Fe_3C content in **Figure 55**b. In the whole range of the Fe_3C content, a strong positive correlation of the electrochemical activity with the Fe_3C content was observed.

Similar plots to **Figure 55**b are presented for other iron containing phases in **Figure 55**c-f. From the Figures, no dependence of the ORR activity was observed for the other iron components, e.g. α-Fe, γ-Fe or γ-Fe_2O_3. It is of note that in previous literature, the iron components have not distinctly specified but often labelled as "iron-based" or Fe/Fe_3C phases[39,41-43,46,48]. The FeN_x/C component is of particular interest, as it has been widely identified as the ORR active sites. The observed overall positive trends support this conclusion (**Figure 55**e), though the overall content of this phase is in a very narrow range. It should be noted that 700-35 virtually deviates from FeN_x/C correlations (the spots in the right of **Figure 55**e) but corresponds to the Fe_3C correlations. The reason is attributed to overestimated FeN_x/C content for 700-35 (28 wt%/ total Fe) by associating with partial molecular-like or disordered FePc according to the above Mössbauer analysis. Overall, the important finding is the positive correlation of the FeN_x/C and Fe_3C content with the ORR activity, suggesting that the two metal containing components be involved in the active sites, while no ORR activity contributions from other inorganic Fe like α-Fe and γ-Fe can be concluded.

It should be noted that the sample 850-35, as described in Chapter 3, is a kind of different in morphologies. While all other samples are porous powders in the featured microspheres likely consisting of curved carbon nanotubes that are encapsulating iron-containing nanoparticles inside, this 850-35 sample seems more consisting of loose and long carbon nanotubes that are not or poorly curved into the microspheres. The carbon layer encapsulation of metal-containing nanoparticles,

however, prevails in all cases. From the catalysis point of view, the morphology of the microspheres may also play a critical role in one way or another. This should be kept in mind particularly for the sample 850-35.

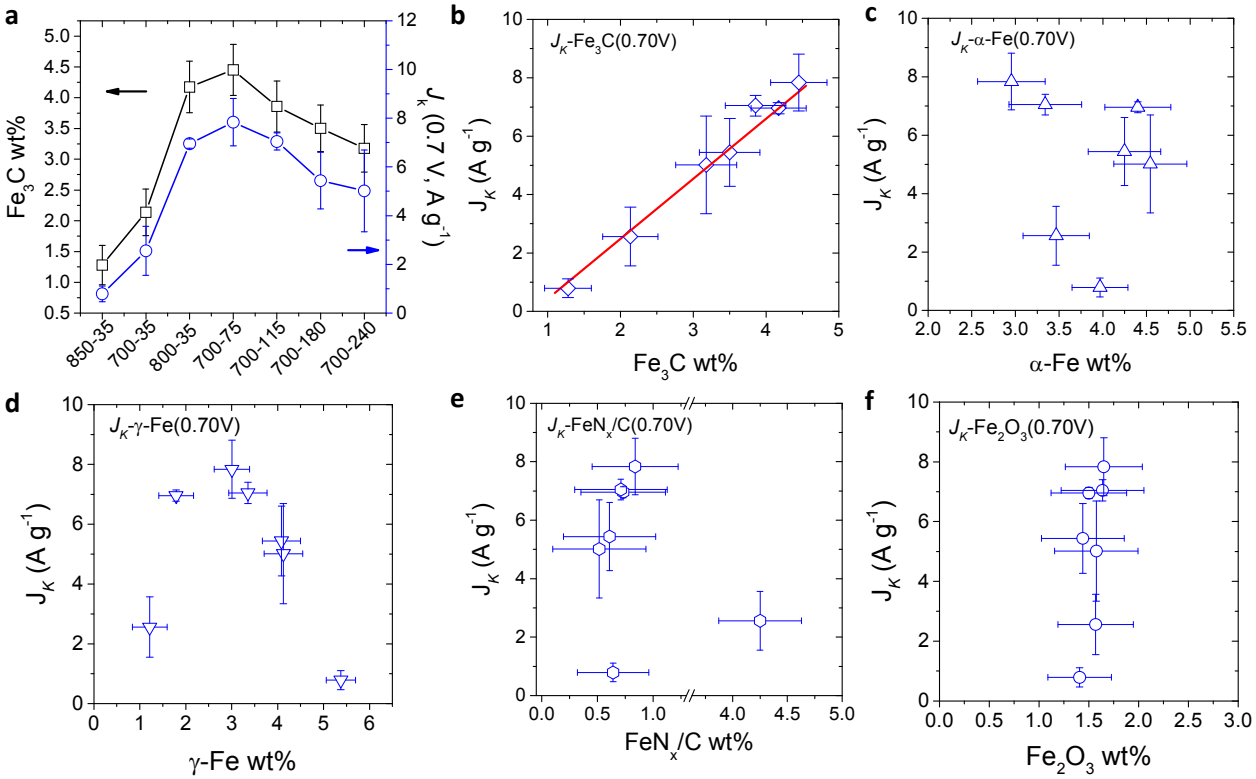

Figure 55. Identification of ORR active sites. (a) Mass specific kinetic current density J_k at 0.70 V vs. RHE and the Fe_3C content for samples prepared by pyrolysis at 700°C for varied durations, 800-35, and 850-35. (b-f) mass specific kinetic current density J_k at 0.70 V vs. RHE as a function of the content of various identified Fe components including α-Fe, Fe_3C, γ-Fe, FeN_x/C and Fe_2O_3. Error bars were obtained fromthe standard deviation of 3-5 independent RDE measurements for each catalyst.

Because of its poor chemical stability especially in acidic electrolytes, the identified Fe_3C can only exist in the subsurface to the carbon layers, in fact, more likely, the N-doped form of the carbon layers. The promoting mechanism of the ORR activity by the encapsulated Fe phase is probably via synergies with those surface functionalities[111]. The density function theory (DFT) calculations revealed that the interaction between the Fe and carbon in the CNT wall significantly enhances the activity towards the ORR[112]. Based on the in-situ element specific X-ray absorption spectroscopic results, the subsurface Fe/Fe_3C was previously demonstrated to be inactive towards the O_2 adsorption and the ORR activity predominantly appeared to arise from the N-doped carbon surface[45]. Even formation of

Fe/Fe_3C nanoparticles in the neighbourhood of the Fe-N coordination sites was found to promotes the catalytic activity[113]. The present results indicate that the Fe_3C among those complex Fe compositions is a key component for the synergies through the surface carbon layer.

4.7. Conclusions

This chapter is the continuation of the last chapter in characterization of the three series of catalysts.

^{57}Fe-Mössbauer spectra were measured at 298 and 18 K. Three sextets, two doublets and one singlet are identified in the spectra. Three sextets are assigned to α-Fe, Fe_3C and γ-Fe_2O_3. The one corresponding to γ-Fe_2O_3 disappears in the room temperature spectra and therefore care should be taken that the quantities of iron components only can be determined from the low temperature Mössbauer spectra (18 K). The singlet component is assumed to be due to γ-Fe.

One doublet is attributed to the initially formed intermediates as it disappears for samples from high temperature or long time pyrolysis. This phase has therefore little significance in the catalysis study. The other doublet, with an isomer shift δ_{iso} of 0.26-0.36 mm s^{-1} and a quadrupole splitting ΔE_Q of 0.91-1.30 mm s^{-1}, is assumed to be due to Fe^{2+} in the low spin (LS), most likely corresponding to the literature identified nitrogen-iron coordination and therefore denoted to FeN_x/C without further specification.

Quantitative determination of these metal containing components was made based on the 18 K Mössbauer spectra. The content of the reduced metal (α-Fe and γ-Fe) component was found to steadily increase with the pyrolytic time and temperature, reaching in sum about 60% of the total iron amount. For all samples after complete decomposition of precursors, the content of the iron-nitrogen coordination, i.e. the FeN_x/C phase, is stabilized at about 3-6%. The content of Fe_2O_3, either formed inside the autoclave due to the trace of oxygen/water or formed during the storage of the catalysts in air after synthesis, is nearly constant at ca. 12-13%. The most interesting finding is that the Fe_3C content shows a peak for sample 700-75 (35%) and 800-35 (33%) in the two series of catalysts samples, apparently indicating a fast initial formation followed by slow decomposition at higher temperature or during the prolonged pyrolysis. These numbers cited above are the percentage of the iron component in the total iron amount, which is about 12-13 wt% of the total solid catalyst powders as determined by the ICP-MS analysis in Chapter 3.

The catalytic activities and mechanisms for ORR are evaluated by RDE and RRDR. The best catalyst, from pyrolysis at 700 ^{o}C and 75 min, exhibited a high onset potential of 0.85 V at 0.1 mA cm^{-2}. In terms of the mass specific kinetic current density and half-wave potential, a strong correlation of the catalytic activity, was found with the Fe_3C content within the entire composition range from 1.1 wt% to 4.5 wt% of the catalyst. The FeN_x/C content, though varying in a very narrow range from 0.5 wt% to 0.85 wt% of the catalyst, showed also a linear correspondence with the catalytic activity. Other iron containing components, i.e. α-Fe, γ-Fe and Fe_2O_3, showed no association with the ORR activity.

In addition, catalysts synthesized from nitrogen free precursors showed some catalytic activities, through lower than those for catalysts from nitrogen containing precursors, confirming the active role of the carbon encapsulated metal particles in the ORR catalysis. Heat treatment of the materials under an ammonia atmosphere shows further enhancement of the ORR activity, indicating the contribution of the nitrogen functionalities**.**

Chapter 5

Anion Poisoning as a Probe to Active Sites

To further explore the possible active sites, one sample of the catalysts, 700-75, the one with best catalytic activity, is selected for the catalytic poisoning study together with other analogues, one is the commercially available Fe/N/C type catalyst and the other is the chemical grade iron phthalocyanine with well-defined structure and composition. By virtue of the strong iron coordinating anions, cyanide (CN^-) and thiocyanate (SCN^-), it was found the G@ Fe shows weak poisoning effect relative to the other analogue catalysts in both alkaline and acid media, suggesting the involvement in the ORR catalysis of both encapsulated iron containing nanoparticles as well as the well-known FeN_x/C surface functionalities.

5.1. Introduction

To understand the active origins of NPMCs, some precise spectroscopic methodologies like X-ray absorption near edge structure (XANES) and extended X-ray absorption fine structure (EXAFS) have been employed.[74] A few fine FeN_x/C structures have been identified for the so-called exposed FeN_x/C catalysts in comparison to the encapsulated or confined type of catalysts handled in the present thesis. Another simple strategy is based on complexing of e.g. cyanide (CN^-) and thiocyanate (SCN^-) with metal sites in catalysts in order to examine the involvement in ORR activities by the poising effect[114-116]. Yeager et al. seemed the first in the 1990s who reported the cyanide poisoning on metal macrocycles, e.g. iron phthalocyanine (FePc), the typical molecular type catalysts. They found that the ORR activity was remarkably inhibited to a nearly completely loss in a solution containing 1 mM CN^- [114]. Gewirth et. al. reported also the poisoning effect on the carbon-supported FePc both

before and after pyrolysis. Their results showed a less significant effect than on the pure FePc of Yeager's results, indicating that carbon supports can stabilize or partially participate in the ORR catalysis.[115] Very recently, Sun and co-workers synthesized a highly active phenylenediamine-based FeN_x/C catalyst and demonstrated by the ion poisoning in an acidic medium that the element Fe in the FeN_x coordination is involved in the active sites [116].

In this chapter, an attempt is made to explore the catalytic poisoning by the electrochemical probes towards the identification of active sites of the present catalysts. First, the possible FeN_x/C coordination as disclosed by the doublet in Mössbauer spectroscopy and its involvement in the ORR catalysis are studied by comparing with two selected analogue catalysts. One is a commercially available catalyst of the Fe/N/C type, however with ignorable encapsulation of nanoparticles. The materials were purchased from Pajarito Powder, LLC (Precious-Metal-Free Catalysts, NPC-2000). The other is the molecular iron phthalocyanine (FePc), a model system that possess a well-defined $Fe^{2+}N_4/C$ coordination structure and in a pure composition.

5.2. Characterization of the catalysts

5.2.1. Morphologies of the Representative Three-type of catalysts

The morphologies for the three types of catalysts were first examined by TEM as seen in **Figure 56**. The G@Fe catalyst has a typical structure of microspheres of 300-400 nm in diameters, consisting

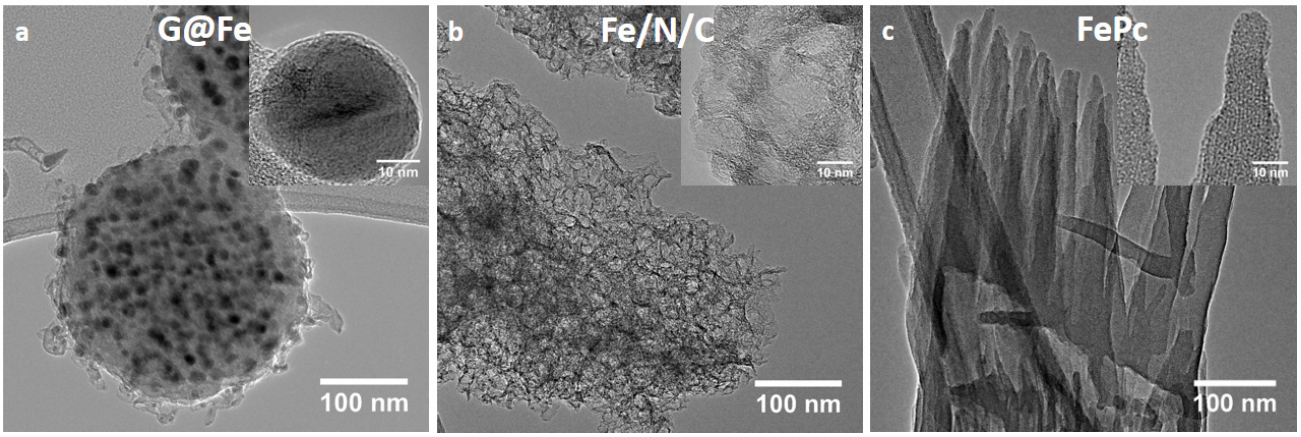

Figure 56. TEM images of the three catalyst samples, (a) the as-prepared G@Fe from the present work; (b) the commercial Fe/N/C type catalyst and (c) the molecular FePc. The insets show the HRTEM images.

of metal containing nanoparticles encapsulated within carbon layers, as already well described in Chapters 3 and 4. A high resolution TEM image (insert of **Figure 56**a) shows that the size of an individual confined nanoparticle is around 20 nm and the thickness of the graphitic layer is about 1-3 nm. For the commercial Fe/N/C catalyst (**Figure 56**b), it has a highly porous structure. The TEM images did not show any apparent Fe nanoparticles. The Fe content of this catalysts is very low (ca. 0.2 wt%), compared to more than 10 wt% of the catalysts synthesized in the present work. The Fe is assumed to be coordinated with nitrogen supported on carbon, i.e. in the FeN_x/C structure. For the molecular FePc, the TEM sample on the grid was prepared from an ethanol solution and **Figure 56**c shows a kind of self-assembled supramolecular nanobelt-like structure.

5.2.2. XRD and XPS Results

To further obtain the structural compositions, XRD and XPS were used to examine the three samples. XPD results show remarkable differences for the three samples (**Figure 57**). The G@Fe sample exhibited complex crystalline phases including graphitic carbon, α-Fe, γ-Fe, and Fe_3C while the Fe/N/C sample simply shows a graphitic carbon diffraction peak at around 2θ = 26 °C and a broad Fe pattern, indicating the essentially amorphous nature of the Fe containing phase. The FePc sample disclosed a series of diffraction peak, hinting formation of the self- assembled structure with poor crystallinity.

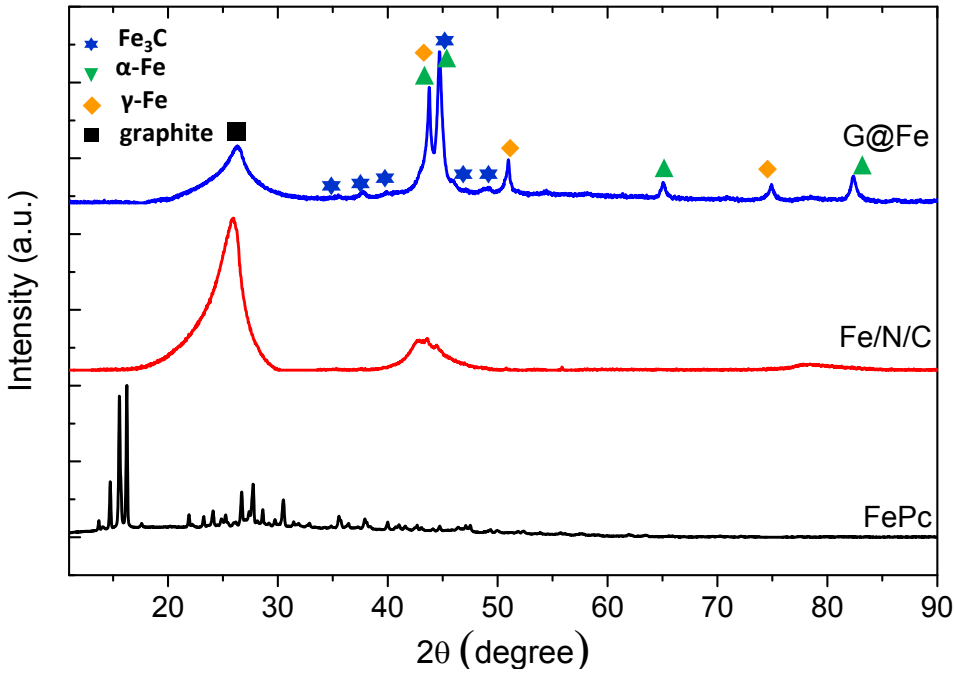

Figure 57. XRD patterns of the G@Fe, Fe/N/C and FePc samples.

Further XPS analysis is shown in **Figure 58**. The Fe2p spectra demonstrate that the G@Fe and FePc samples contain significant Fe components while the commercial Fe/N/C has nearly invisible Fe traces (**Figure 58**a). However, for the G@Fe sample as we discussed in Chapter 3, it is difficult to distinguish the XPS Fe signal either from the bulk or the surface. The N1s spectra confirm the four types of N doped on graphitic layers (N1s, **Figure 58**b) including pyridinic N (398.2eV), pyridonic N (400.3 eV), graphitic N (401.3 eV) and oxidized N (403.5eV) in both G@Fe and Fe/N/C catalysts. These four types of N are, in fact, often observed in pyrolyzed catalysts. It is natural that only the pyridinic N is observed in FePc.

In summary, the three catalysts can be described as follows. The G@Fe contains multi-Fe components encapsulated within carbon, most rightly speaking, nitrogen doped carbon layers. The commercial Fe/N/C catalyst is primarily in an amorphous structure with surface FeN_x/C and/or N_xC functional sites. The FePc is composed of pure $Fe^{2+}N_4/C$ sites and pyridinic N.

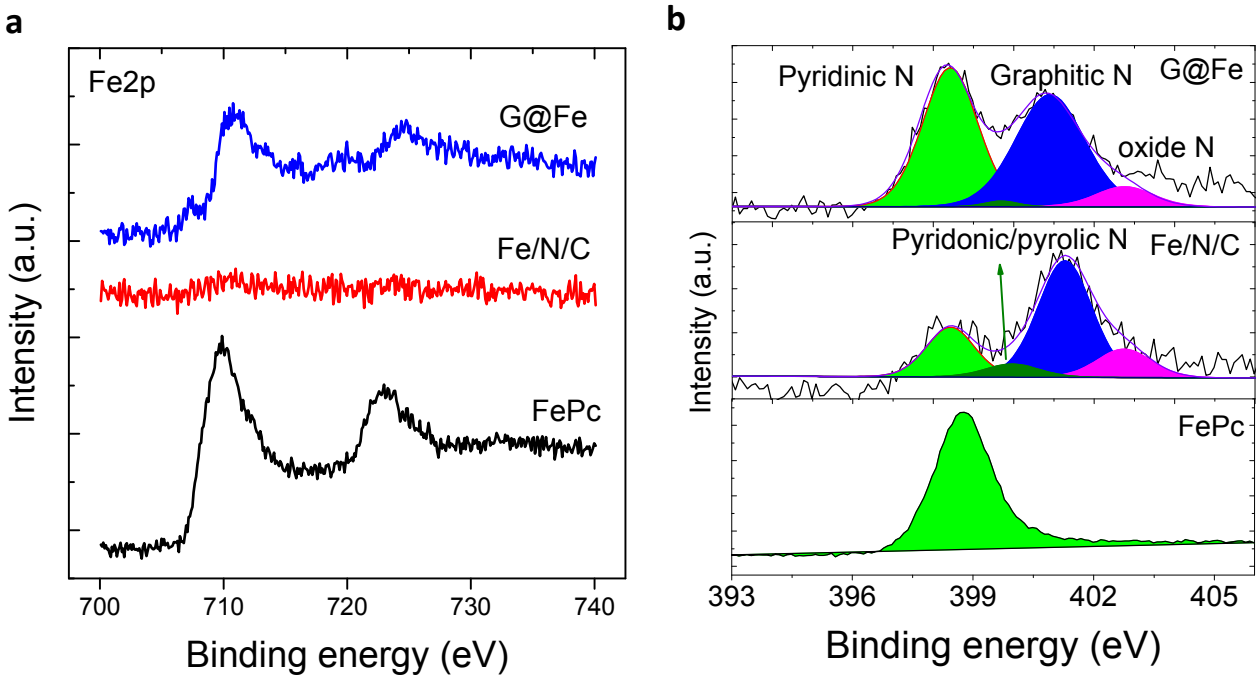

Figure 58. XPS analysis for the three catalysts (G@Fe, Fe/N/C and FePc). (a) Fe2p XPS. (b) N1s XPS.

5.3. Anion Poisoning Tests for ORR

Two strong metal-binding ions, SCN^- and CN^-, are used to form complexes with Fe. Cyanide is stable in basic media while converted to highly toxic hydrogen cyanide in acidic solutions. In the

$HClO_4$ solution, SCN^- is used instead of CN^- . All three catalysts were loaded on the RDE and line sweep voltammetry (LSV) from 1.0 V to 0.1 V (vs RHE) at a scan rate of 10 mV s^{-1} was conducted.

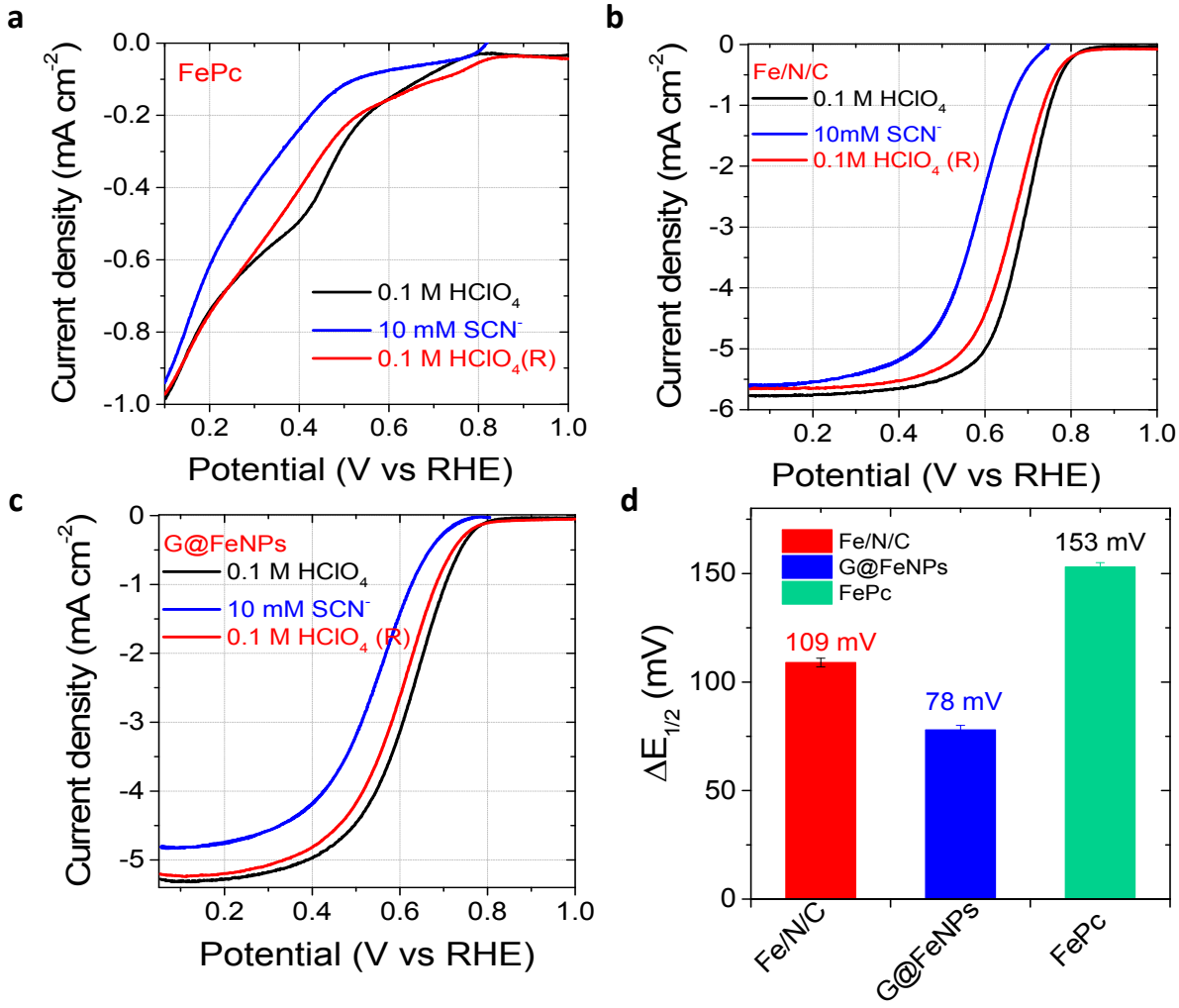

Figure 59. Anon poisoning in O_2-saturated acid media (0.1 M$HClO_4$). LSVs of (a) G@Fe, (b) Fe/N/C and (c) FePc in different electrolytes solutions. Black curves: 0.1 M $HClO_4$; Blue curves: 0.1 M $HClO_4$ and 10 mM KSCN. Red curves: the electrodes transferred back to the fresh 0.1 M $HClO_4$ solution. (d) A comparison of the shifts of $E_{1/2}$ for the three catalysts by SCN^- poisoning. Scan rate 10 mv s^{-1}, rotating speed 900rpm.

The SCN^- ion poisoning in 0.1 M $HClO_4$ is shown in **Figure 59**. First of all, both G@Fe and Fe/N/C disclosed good ORR activity initially (black lines in Figure 59a and b) while FePc exhibited relatively poor activity (black line, **Figure 59**c). After adding 10 mM KSCN into the electrolyte solution, all three catalysts showed negative shifts of LSV curves. Their shift values for the half-wave potentials are summarized in **Figure 59**d, which are in the order of 78 mV (G@Fe) < 109 mV

(Fe/N/C) < 153 mV (FePc). These results suggest the as-prepared G@Fe catalyst has the highest anti-poisoning ability. When the electrodes were transferred back to the fresh electrolyte solution

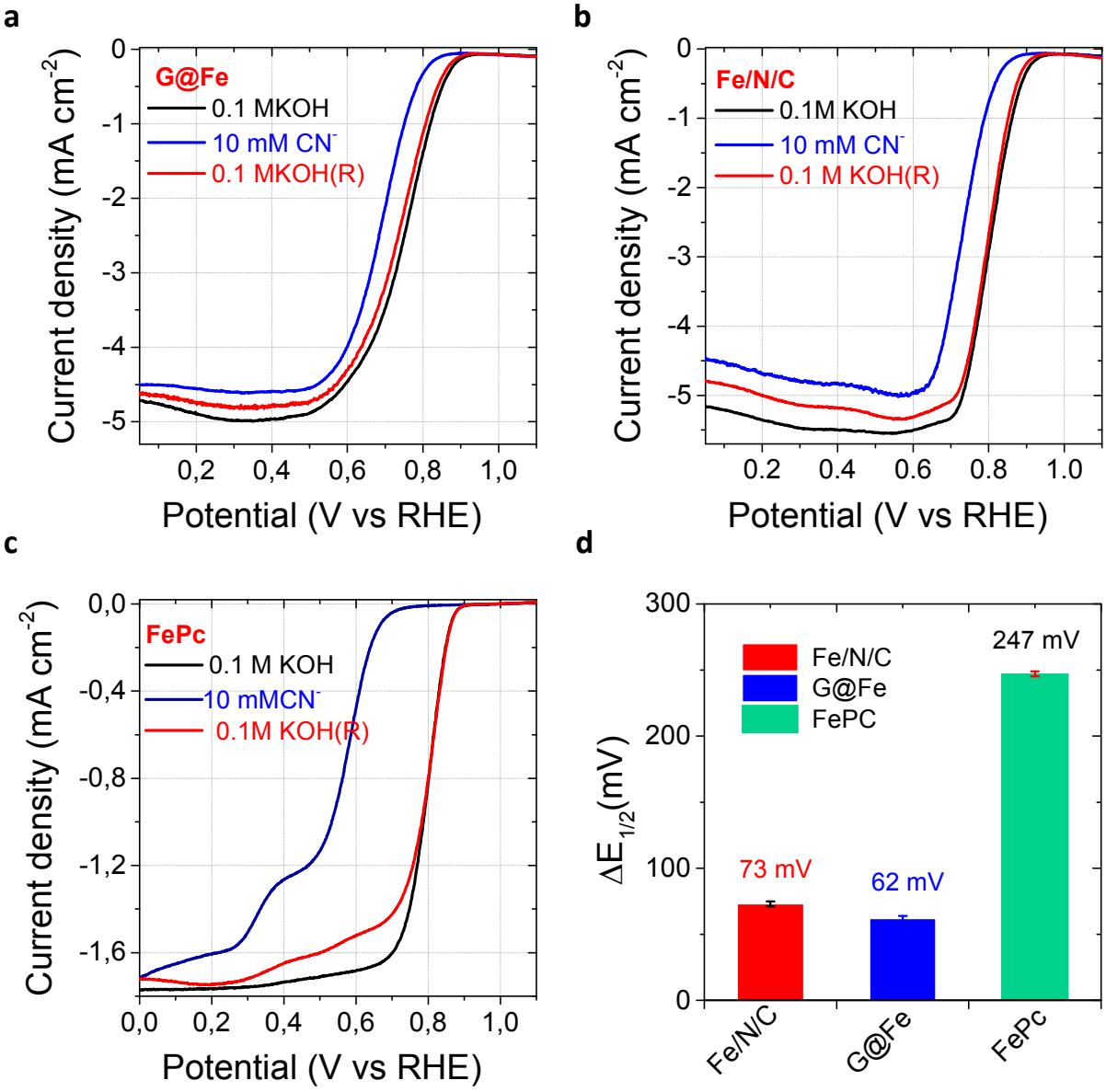

Figure 60. Ion poisoning O_2-saturated in base (0.1 M KOH). LSVs of (a) G@Fe, (b) Fe/N/C and (c) FePc in different electrolytes solutions. Black curves: 0.1 M KOH; Blue curves: 0.1 M KOH and 10 mM KCN. Red curves: the electrodes transferred back to the fresh 0.1 M KOH solution. (d) A comparison of the shifts of $E_{1/2}$ for the three catalysts by CN^- poisoning. Scan rate 10 mv s^{-1}, rotating speed 900 rpm.

(red lines in **Figure 59**), all the catalysts show partial recovery of the activity suggesting a dynamic equilibrium of the SCN^- binding.

For the anion poisoning (CN^-) in the basic solution, similar poisoning trend of G@Fe < Fe/N/C < FePc was observed (**Figure 60**). However, it should be noted that a relatively small loss of $E_{1/2}$ for both G@Fe (62 mV) and Fe/N/C (73 mV) were resulted compared with those in acidic media even though CN^- has the stronger metal-binding ability. Moreover, both of them shows close poisoning degree while more loss of Fe/N/C was observed in acid (**Figure 60**d). These results suggest the possible difference between active sites in acidic and alkaline media, which will be discussed in the next section.

5.4. Discussion of Active Sites

On the basis of recognized compositions of the catalysts, a schematic illustration of the structures of the three catalysts is suggested in **Figure 61**. The G@Fe exhibits a more complex structure with a confined multi-Fe core (α-Fe, γ-Fe and Fe_3C) and a graphitic layer shell. This shell layer contains coordinated Fe (FeN_x/C) and N-doped carbon (N_xC) (**Figure 61**). The structures of Fe/N/C and FePc are easily described as open surface functionalities (**Figure 61**b and c).

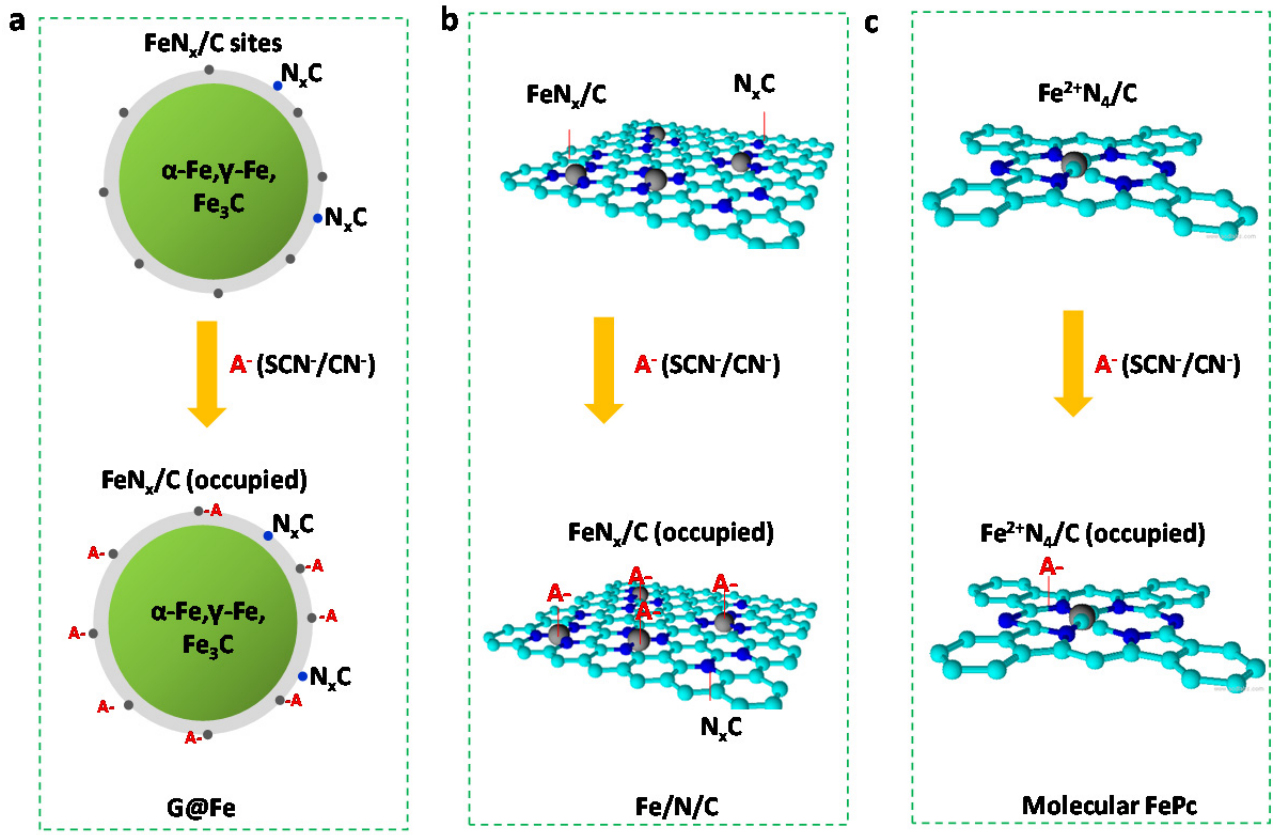

Figure 61. The proposed structure of active sites (or active contribution) in acidic and basic electrolytes for (a) G@Fe, (b) Fe/N/C and (c) FePc.

After anion binding, the surface FeN_x/C sites (or $Fe^{2+}N_4/C$ for FePc) are occupied. The anion-poisoning examination clearly shows that significant poisoning occurs on all three types of catalysts. The resultant activity loss is, however, less for the G@Fe and follows the order of G@Fe < Fe/N/C < FePc in both acid and basic solutions. In general, the poisoning effect is stronger in acid than that in base.

Based on the above structures and the loss trends of ORR activity, it can be understood that the ORR active sites for the state-of-the-art Fe based NPMCs involve three types of active sites, i.e., the nitrogen doped carbon N_xC and iron-nitrogen coordination on carbon support (FeN_x/C). In addition, the encapsulated Fe containing species also contribute. *First of all*, the activity loss for the G@Fe catalyst indicates that there exist some Fe species in the N-doped carbon layer, which can be easily associated with SCN^- and CN^-. Otherwise, there should be no ORR activity loss upon anion poisoning since other metal-free sites like N_xC cannot bind these anions. The surface Fe moiety is likely of the type FeN_x/C i.e. the well-recognized active sites for Fe/N/C type catalysts, which have not been very much considered in previous studies on the encapsulated catalysts. This result on one hand confirms the Mössbauer results of identification of FeN_x/C sites in the last Chapter, and, on the other, further clarifies the significant role of this sites. As shown in the last chapter a strong correlation between the FeN_x/C and ORR activity is observed though within a very narrow content variation of this component.

Secondly, the poisoning trend of G@Fe < Fe/N/C suggests that the encapsulated Fe containing components in the G@Fe should also play a significant role in the catalysis, which would not be considerably affected by the anion poisoning. In combination with the results in the last Chapter, the Fe_3C should be the encapsulated active sites. In addition, both G@Fe and FeN_x/C show relative low poisoning effect than that of FePc, which confirms the well-known fact that the high temperature pyrolysis increases its stability.

Finally, the stronger poisoning in acidic than in basic media suggests that different contributions of active sites are involved in catalysis in acidic or basic media. It is well known that the metal-free N_xC functionalities exhibited higher activity in basic media, which is even comparable to the noble metals. Therefore, the N_xC moiety might also play a role in the catalysis. This might be the reason why less poisoning effect is observed for G@Fe and FeN_x/C in basic media even though the FeN_x/C site is poisoned. In addition, the large activity loss in acid is probably due to the small contribution of N_xC sites in acidic media.

5.5. Conclusions

In this Chapter, the possible active sites of three types of catalysts are electrochemically probed by anion poisoning in association with iron containing moieties. The encapsulated G@Fe catalysts showed relatively low poisoning effect by cyanide (CN^-) in alkaline and thiocyanate (SCN^-) in acidic electrolytes, compared to that for the commercially available FeN_x/C catalysts and the molecular phthalocyanine. It seems that the surface N-coordinated Fe species indeed is involved in the catalysis in addition to the recognized encapsulated metal nanoparticles. The metal-free N_xC functionalities, which are not poisoned by the two anions, may also be involved in catalysis.

Chapter 6

Conclusive Remarks and Perspectives

6.1. Conclusive Remarks

Development of non-precious metal catalysts (NPMCs), as a replacement to the expensive and scarce noble metals, has been one of the most active subjects in the field of proton exchange membrane fuel cells. The most promising materials investigated thus far are transition metal-nitrogen-carbon composites MN_x/C where the transitional metals are typically Co, Fe and Ni. The widely used method for preparation of the MN_x/C catalysts is by pyrolysis of a variety of metal, nitrogen and carbon precursors. The pyrolysis is, in general, performed in open reactors under ambient pressure. A higher pressure process is investigated in the present thesis. The high pressure is achieved in a solvent-free, or in other words, a dry autoclave process. When the temperature is higher than the dissociation temperatures of the precursors, it is believed that some supercritical solid-liquid, solid-gas or gas-gas phases are formed and the autogenic high pressure is then created.

By using volatile small molecules of ferrocene and cyanamide as precursors, the dry autoclave pyrolysis leads to formation of porous powders made of micro-spheres in size of 300-400 nm diameter. The spheres are consisting of uniform metallic nanoparticles of typically 10-20 nm, encapsulated in graphitic layers in form of carbon nanotubes. The carbon nanotubes contain apparently doping nitrogen atoms on the surface. And the encapsulation structure is essential for stabilizing the metal-containing nanoparticles from the chemical dissolution in acidic solutions during the following acid leaching as well as the electrochemical evaluation.

The research work within this thesis is therefore schemed with three major objectives: 1) further optimization of the pyrolysis in order to improve the electrochemical performance of catalysts; 2) exploration of the complex Fe-containing components and 3) recognition of the possible active

sites. For doing so, three series of catalysts are first synthesized with varied pyrolytic temperatures, durations and selected precursors.

The first series of catalysts are synthesized from cyanamide and ferrocene, in a mass ratio of 9 to 1, at pyrolytic temperatures of 600, 700, 800 and 850 ^{o}C for a duration of 35 minutes. The second series of catalysts are prepared, from cyanamide and ferrocene in a mass ratio of 9 to 1 at varied pyrolysis durations from 15 to 240 minutes at a fixed temperature of 700 ^{o}C. The third series of catalysts are made from nitrogen-free precursors, i.e. durene and ferrocene at 700 and 800 ^{o}C for a duration of 35 minutes. Part of these N-fee samples are post treated under an NH_3 atmosphere at 850 ^{o}C for 1 hour.

Systematic characterization of these catalyst samples are carried out in two major categories: One is the morphological, crystalline and elemental analysis presented in Chapter 3. The other is Mössbauer spectroscopy for identification and quantification of various iron components and electrochemical evaluation of the catalytic activities, as presented in Chapter 4. Based on these results, correlation of the ORR activities with the metal containing phases is endeavored. Additional effort is finally made to investigate the anion poisoning effect on the ORR activity of three structurally defined catalysts in order to provide further information on the possible active sites of the catalysts. These results and the conclusions are summarized below.

TEM characterization reveals that pyrolysis of ferrocene and cyanamide at 600 ^{o}C involves polymerization of the cyanamide, leading to formation of melamine-rich microspheres with ferrocene dispersed evenly in the spheres. At pyrolytic temperature of 700 ^{o}C the microspheres maintain their morphologies while the precursors start to gradually decompose into graphitic carbon. Metal or metal carbide particles from decomposition of ferrocene, catalyze the carbon deposition, leading to formation of uniformly distributed metal-containing nanoparticles encapsulated by the carbon layers. At temperatures higher than 700 ^{o}C, the porous microspheres become smaller in size and less regular in shape. Eventually at 850 ^{o}C the spherical morphology of the catalysts is crumpled to a great extent, forming loose and long carbon nanotubes, still encapsulating the metal-containing nanoparticles. When the temperature is fixed 700 ^{o}C, a duration of 15-35 minutes does not seem to be sufficient to achieve complete decomposition of the precursors. After pyrolysis for longer than 35 minutes, the microspheric morphology of the catalysts exhibits little change though the size of the porous spheres becomes small.

The HRTEM and element mapping shows a uniform distribution of C and N throughout the catalyst spheres while element iron is more concentrated on the encapsulated nanoparticles with nearly invisible distribution on the surface of the carbon nanotubes.

The crystalline phases of the catalysts are revealed by the XRD. At a pyrolytic temperature of 600^{o}C little decomposition of the precursors occurs. The XRD also shows that the formed melamine-rich microspheres have some crystallinity. In sample 700-15 an inorganic, crystalline Fe_3N phase is identified, which is then decomposed during the following pyrolysis. At temperatures above 700 ^{o}C, graphitic carbon is deposited and metal-containing nanoparticles are developed within the microspheres. Little change of these phases is observed after prolonged pyrolysis.

The solid yields, defined as the collected catalyst powders in relation to the initial mass of precursors, are found to be about 23-25 wt% after complete decomposition. The element analysis is made by C/H/N for carbon and nitrogen and ICP-MS for iron. It shows that, of the solid powders, there are about 12-13 wt% iron, 77-80 wt% carbon, and 1-2 wt% nitrogen with the rest balanced by oxygen and probably some hydrogen as well.

The XPS analysis is made for the surface carbon (C1s), nitrogen (N1s) and Iron (Fe2p). From the C1 spectra, the N=C is identified for samples with remaining precursors. The presence of C-C(sp^2) indicate the deposition of graphitic carbon, which is increasing with pyrolytic temperature. The N1s spectra show five types of surface N components including pyridinic N, precursor N, pyridonic & pyrrolic N, graphitic N and oxide N. A slight decrease is observed in the total N content, from 3.2 wt% for 700-75 to 2.3 wt% for 700-240. The Fe2p spectra for all samples showed week intensity though the bulk content of the total iron in the catalyst powder is as high as 12-13 wt%, likely indicating the encapsulation of the iron containing particles by the surface graphitic layers.

The N-free catalyst samples, prepared from pyrolysis of ferrocene and durene, are not developed into microspherical morphologies, showing important of cyanamide in the sphere formation. Carbon is deposited as long nanotubes with larger metal-containing particles typically encapsulated inside the tubes. XRD shows the presence of metallic and carbide phases.

^{57}Fe-Mössbauer spectra were measured at 298 and 18 K. Three sextets, two doublets and one singlet are identified in the spectra. Three sextets are assigned to α-Fe, Fe_3C and γ-Fe_2O_3. The one corresponding to γ-Fe_2O_3 disappears in the room temperature spectra and therefore care should be taken that quantities of iron components only can be determined from the low temperature Mössbauer spectra (18 K). The singlet component is assumed to be due to γ-Fe. One doublet is attributed to the initially formed intermediates as it disappears for samples from high temperature or

long time pyrolysis. This phase has therefore little significance in the catalysis study. The other doublet, with an isomer shift δ_{iso} of 0.26-0.36 mm s^{-1} and a quadrupole splitting ΔE_Q of 0.91-1.30 mm s^{-1}, is assumed to be due to Fe^{2+} in the low spin (LS), most likely corresponding to the literature identified nitrogen-iron coordination and therefore denoted to FeN_x/C without further specification.

Quantitative determination of these metal containing components was made based on the 18 K Mössbauer spectra. The content of the reduced metal (α-Fe and γ-Fe) component was found to steadily increase with the pyrolytic time and temperature, reaching in sum about 60% of the total iron amount. For all samples after complete decomposition of precursors, the content of the iron-nitrogen coordination, i.e. the FeN_x/C phase, is stabilized at about 3-6 wt%. The content of Fe_2O_3, either formed inside the autoclave due to the trace of oxygen/water or formed during the storage of the catalysts in air after synthesis, is nearly constant at ca. 12-13 wt%. The most interesting finding is that the Fe_3C content shows a peak for sample 700-75 (35 wt%) and 800-35 (33 wt%) in the two series of catalysts samples, apparently indicating a fast initial formation of the carbide followed by slow decomposition at higher temperature or during the prolonged pyrolysis. From these numbers, i.e. the percentage of a specific iron component in the total iron amount, are used together with the total iron content of 12-13 wt% from the ICP-MS analysis, to give the content of each iron component in in the total solid catalyst powders.

The catalytic activities and mechanisms for ORR are evaluated by RDE and RRDR. The best catalyst, from pyrolysis at 700 ^oC and 75 min, exhibited a high onset potential of 0.85 V at 0.1 mA cm^{-2}. In terms of the mass specific kinetic current density and half-wave potential, a strong correlation of the catalytic activity, was found with the Fe_3C content within the entire composition range from 1.1 wt% to 4.5 wt% of the catalyst. The FeN_x/C content, though varying in a very narrow range from 0.5 wt% to 0.85 wt% of the catalyst also with a big error from the Mössbauer spectra, showed also a linear correspondence with the catalytic activity. Other iron containing components, i.e. α-Fe, γ-Fe and Fe_2O_3, showed no association with the ORR activity.

In addition, catalysts synthesized from nitrogen free precursors showed some catalytic activities, through lower than those for catalysts from nitrogen containing precursors, confirming the active role of the carbon encapsulated metal particles in the ORR catalysis. Heat treatment of the materials under an ammonia atmosphere shows further enhancement of the ORR activity, indicating the contribution of the nitrogen functionalities**.**

Two anions are used to probe the iron containing active sites towards the ORR, cyanide (CN^-) in alkaline and thiocyanate (SCN^-) in acidic electrolytes. Three types of catalyst materials are selected:

the present G@Fe catalysts containing multi-Fe components encapsulated within carbon or nitrogen doped carbon layers; a commercial Fe/N/C catalyst in an amorphous structure with surface FeN_x/C and/or N_xC surface functional sites; and the molecular phthalocyanine FePc composed of pure $Fe^{2+}N_4/C$ sites and in pure composition. The results show that the FePc exhibited the maximum poisoning effect, the Fe/N/C catalyst the intermediate while the G@Fe catalyst the minimum effect. This seems supporting the conclusions that, in the present catalysts, the recognized encapsulated iron carbide and/or the FeN_x/C/ nanoparticles are contributors to the ORR activity, in addition to the well literature identified N-coordinated Fe species.

6.2. Perspectives

Electrocatalysis of the oxygen reduction reaction (ORR) is a long-lasting subject in the electrochemsitry field and a fundamental issue in numerous types of electrochemical energy conversion and storage devices e.g. fuel cells. The core of this subject is understanding the kinetic mechanisms and developing highly active and stable catalysts to lower the intrinsic kinetic barriers. Among various developed materials, carbon supported Pt nanoparticles are the state-of-the-art catalysts, which are only practically used in the fuel cell technologies. The only fly in the ointment is the high cost and low abundance for the Pt, which prohibit the large-scale application and mass production of the technology. Recent advances in optimization of nanostructures of Pt-based materials, e.g. in form of Pt jagged nanowires[15] have shown potentials in further improving the catalytic performance and therefore reducing the metal usage.

An alternative solution is the development of non-precious metal catalysts (NPMCs). Fe-based nanomaterials represent the state-of-the-art candidate showing very encouraging activity. Recently reported Fe based NPMCs with the FeN_x/C type of active sites exhibited a performance of volumetric current density as high as 320 A cm^{-3} in real PEM fuel cells[31]. This is higher than the DOE 2017/2020 target of 300 A cm^{-3} at the cell voltage of 0.8 V (iR-free). When compared to the benchmarking Pt/C catalysts, which as a reference have a volumetric current density of 1300 A cm^{-3}, this performance can be translated into ca. 23% of that for the Pt/C, sufficiently encouraging but urgently demanding for further improvement.

From the viewpoint of fuel cell applications, this performance challenge is associated with the high catalyst loads used in real electrodes, i.e. the large thickness and therefore local mass-transport resistivity of the gas diffusion electrodes. The issue should be addressed by further increase in the

active site density of the NPMC materials, which ultimately would result in a thin catalyst layer with better characteristics of mass transportation.

Another challenge for the NPMCs is the long-term stability, which has been demonstrated in a period of a few hundred hours so far. Further improvement of the stability is the top issue of NPMCs. Graphitic layer encapsulated iron based nanoparticles, as presented in this thesis, may provide an opportunity in this connection, as part of the catalytic activity is associated with a kind of active sites that are confined by the graphitic layers and isolated from the external harsh electrolyte solution. The understanding of this catalytic mechanism is still missing.

The encapsulated nanoparticles are revealed to be composed of complex compositions including α-Fe, γ-Fe, Fe_2O_3, Fe_3C and coordinated Fe (FeN_x/C) by Mössbauer spectroscopy. Further clarification of the roles of the active phases, particularly the carbide and coordinated phases, will lead to new insights of MPNCs and therefore further optimization of the pyrolysis parameters and precursors in order to develop new active sites and high density of them, most likely the FeN_x/C and Fe_3C. In this connection, the thickness of graphitic layers should also play a critical role. In the prepared catalysts, the thickness around Fe cores remains ca. 2-4 nm, i.e. about 5-10 layers. There should be an optimized layer for accelerating the electron transfer between the graphitic layer and encapsulated sites. *In-situ* ^{57}Mössbauer spectroscopy associated with electrochemical tests should be able to provide valuable information concerning the Fe phase and graphitic layers and therefore allow for furthering exploring the ORR mechanism.

Appendix A Supplementary Data

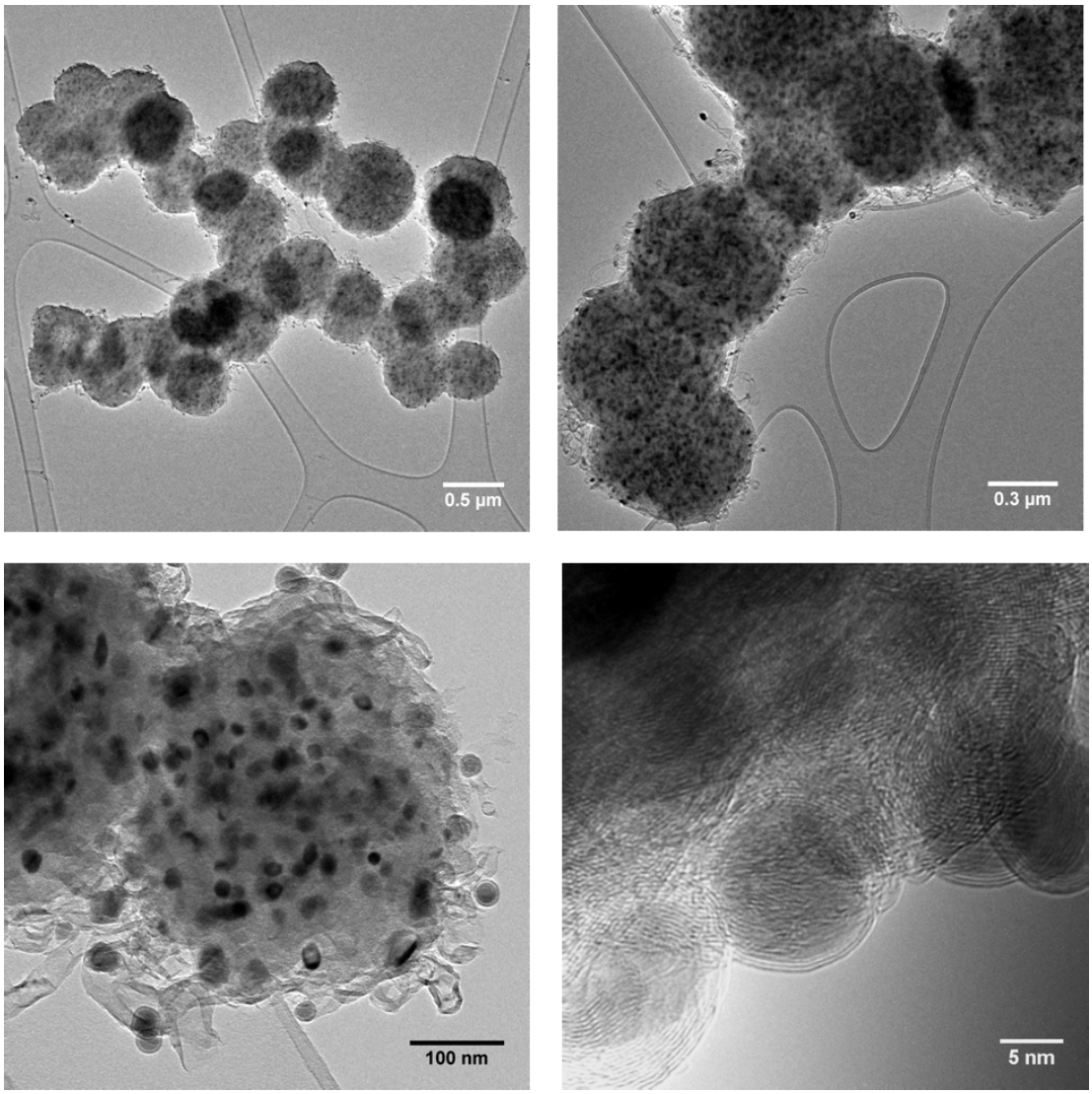

Appendix Figure 1. TEM and HRTEM images for representative G@FeNPs (700-75).

Appendix Table 1. Summary of fitted Mössbauer parameters at 295 K

Samples	Assignment	$B_{(hf)}$ Tesla	δ mm s^{-1}	ε (or Δ) mm s^{-1}	Area (%)
500-35	**γ-Fe**		-0.18	-	8
	Fe-Im		0.88	3.18	83
	FeNx/C		0.53	1.09	9
600-35	**γ-Fe**		-0.10	-	5
	Fe-Im)		0.87	2.94	63
	FeNx/C		0.34	1.24	32
700-15	**γ-Fe**		-0.08	-	6
	α-Fe	32.61	-0.02	0.07	7
	Fe_3C	23.92	0.31	-0.05	4
	Fe-Im		0.85	2.78	44
	FeNx/C		0.42	1.29	39
700-35	**γ-Fe**		-0.09	-	12
	α-Fe	33.21	-0.00	0.00	32
	Fe_3C	20.39	0.19	-0.00	19
	FeNx/C		0.33	1.29	37
700-75	**γ-Fe**		-0.09	-	21
	α-Fe	33.14	-0.00	0.00	24
	Fe_3C	20.43	0.18	0.01	35
	FeNx/C		0.25	0.99	20
700-115	**γ-Fe**		-0.09	-	24
	α-Fe	33.22	-0.00	0.00	28
	Fe_3C	20.54	0.18	0.01	30
	FeNx/C		0.24	0.96	18
700-180	**γ-Fe**		-0.09	-	28
	α-Fe	22.28	0.00	0.00	32
	Fe_3C	20.50	0.18	0.01	24
	FeNx/C		0.28	0.88	16
700-240	**γ-Fe**		-0.09	-	25
	α-Fe	33.13	0.00	0.00	35
	Fe_3C	20.43	0.18	0.01	25
	FeNx/C		0.28	0.90	15
800-35	**γ-Fe**		-0.13	-	15
	α-Fe	33.15	0.00	0.00	40
	Fe_3C	20.63	0.18	0.01	37
	FeNx/C		0.32	0.79	8

Appendix Table 2. Summary of fitted Mössbauer parameters at 18 K

Samples	Assignment	$B_{(hf)}$ Tesla	δ mm s^{-1}	ε (or Δ) mm s^{-1}	Area (%)
500-35	**γ-Fe**		-0,14	-	8
	Fe-Im		1.06	3.41	82
	FeNx/C		0.61	1.09	10
600-35	**γ-Fe**		-0.06	-	4
	Fe-Im		1.06	3.22	66
	FeNx/C		0.52	1.30	30
700-15	**γ-Fe**		0.00	-	2
	Fe-Im		1.03	3.07	45
	FeNx/C		0.55	1.37	30
	Fe_3C	26.34	0.44	-0.02	6
	α-Fe	34.97	0.14	0.00	3
	Fe_2O_3	50.00	0.50	-0.05	13
700-35	**γ-Fe**		0.01	-	10
	α-Fe	34.66	0.11	0.00	27
	Fe_3C	25.60	0.30	0.02	17
	Fe_2O_3	50.40	0.58	-0.08	12
	FeNx/C		0.47	1.52	34
700-75	**γ-Fe**		0.03	-	23
	α-Fe	34.65	0.11	0.00	23
	Fe_3C	25.68	0.31	0.00	35
	Fe_2O_3	50.28	0.50	-0.06	13
	FeNx/C		0.15	1.89	6
700-115	**γ-Fe**		0.31	-	26
	α-Fe	34.62	0.11	0.00	26
	Fe_3C	25.64	0.31	0.00	30
	Fe_2O_3	50.41	0.47	0.01	12
	FeNx/C		0.35	1.31	6
700-180	**γ-Fe**		0.03	-	30
	α-Fe	34.77	0.11	0.00	31
	Fe_3C	25.60	0.31	0.00	25
	Fe_2O_3	50.34	0.47	-0.03	10
	FeNx/C		0.35	1.31	4
700-240	**γ-Fe**		0.03	-	30
	α-Fe	34.52	0.11	0.00	33
	Fe_3C	25.61	0.31	0.00	23
	Fe_2O_3	50.62	0.49	-0.04	11
	FeNx/C		0.37	1.30	3
800-35	**γ-Fe**		0.02	-	14
	α-Fe	34.52	0.11	0.00	35
	Fe_3C	25.66	0.31	0.00	33
	Fe_2O_3	50.87	0.42	0.00	12
	FeNx/C		0.35	1.36	6

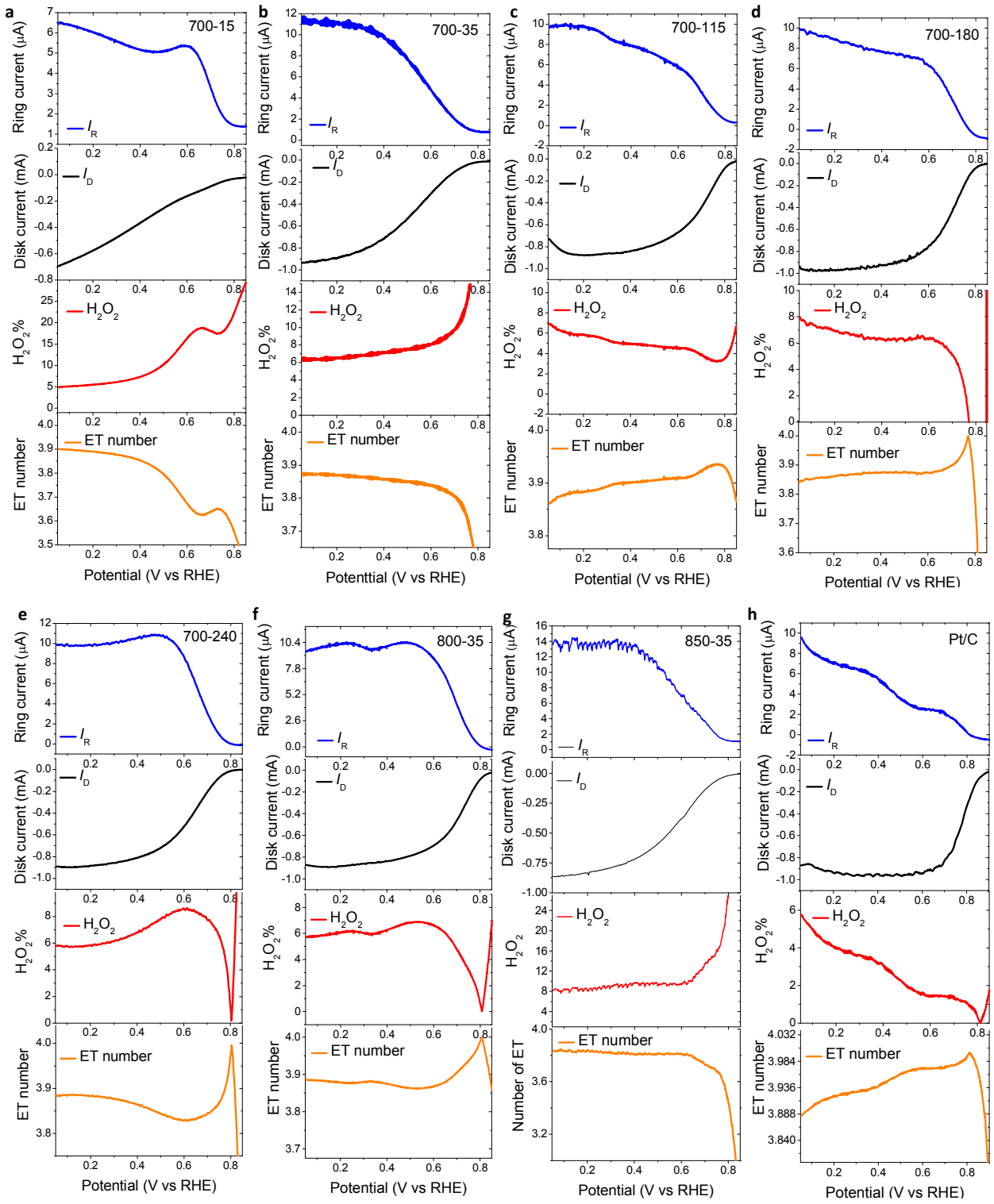

Appendix Figure 2. Ring and disk currents as well as H_2O_2 yield and electron transfer number as a function of the electrode potential (versus RHE) for various G@Fe catalysts..

Bibliography

1 He, C., Desai, S., Brown, G., Bollepalli, S. PEM Fuel Cell Catalysts: Cost, Performance, and Durability. *Interface-Electrochemical Society* **14**, 41-46 (2005).

2 Shao, M., Chang, Q., Dodelet, J.-P., Chenitz, R. Recent Advances in Electrocatalysts for Oxygen Reduction Reaction. *Chemical Reviews* **116**, 3594-3657 (2016).

3 Luo, Y., Alonso-Vante, N. The Effect of Support on Advanced Pt-based Cathodes towards the Oxygen Reduction Reaction. State of the Art. *Electrochimica Acta* **179**, 108-118 (2015).

4 Shrestha, S., Liu, Y., Mustain, W. E. Electrocatalytic Activity and Stability of Pt Clusters on State-of-the-art Supports: a Review. *Catalysis Reviews* **53**, 256-336 (2011).

5 http://energy.gov/eere/fuelcells/doe-technical-targets-polymer-electrolyte-membrane-fuel-cell-components.

6 Wang, Y.-J. *et al.* Carbon-supported Pt-based Alloy Electrocatalysts for the Oxygen Reduction Reaction in Polymer Electrolyte Membrane Fuel Cells: Particle Size, Shape, and Composition Manipulation and Their Impact to Activity. *Chemical Reviews* **115**, 3433-3467 (2015).

7 Gasteiger, H. A., Kocha, S. S., Sompalli, B., Wagner, F. T. Activity Benchmarks and Requirements for Pt, Pt-alloy, and non-Pt Oxygen Reduction Catalysts for PEMFCs. *Applied Catalysis B: Environmental* **56**, 9-35 (2005).

8 Greeley, J. Stephens, I., Chorkendorff, I., Nørskov, J. K., *et al.* Alloys of Platinum and Early Transition Metals as Oxygen Reduction Electrocatalysts. *Nature Chemistry* **1**, 552-556 (2009).

9 Nielsen, J. H., Hansen, T. W., Nilsson, A., Stephens, I., Chorkendorff, I. Mass-selected Nanoparticles of Pt_xY as Model Catalysts for Oxygen Electroreduction. *Nature Chemistry* **6**, 732-738 (2014).

10 Yoo, S. J. *et al.* Pt_3Y Electrocatalyst for Oxygen Reduction Reaction in Proton Exchange Membrane Fuel Cells. *International Journal of Hydrogen Energy* **37**, 9758-9765 (2012).

11 Escudero-Escribano, M. *et al.* Tuning the Activity of Pt Alloy Electrocatalysts by Means of the lanthanide Contraction. *Science* **352**, 73-76 (2016).

12 Wu, J., Gross, A., Yang, H. Shape and Composition-controlled Platinum Alloy Nanocrystals Using Carbon Monoxide as Reducing Agent. *Nano letters* **11**, 798-802 (2011).

13 Chen, C. *et al.* Highly Crystalline Multimetallic Nanoframes with Three-dimensional Electrocatalytic Surfaces. *Science* **343**, 1339-1343 (2014).

14 Huang, X. *et al.* High-performance Transition Metal–doped Pt_3Ni Octahedra for Oxygen Reduction Reaction. *Science* **348**, 1230-1234 (2015).

15 Li, M. *et al.* Ultrafine Jagged Platinum Nanowires Enable Ultrahigh Mass Activity for the Oxygen Reduction Reaction. *Science*, 354. 1414-1419. (2016).

16 Jaouen, F. *et al.* Recent Advances in Non-precious Metal Catalysis for Oxygen-Reduction Reaction in Polymer Electrolyte Fuel Cells. *Energy & Environmental Science* **4**, 114-130, (2011).

17 Wu, G., Zelenay, P. Nanostructured Nonprecious Metal Catalysts for Oxygen Reduction Reaction. *Accounts of Chemical Research* **46**, 1878-1889, (2013).

18 Banham, D. *et al.* A review of the Stability and Durability of Non-precious Metal Catalysts for the Oxygen Reduction Reaction in Proton Exchange Membrane Fuel Cells. *Journal of Power Sources* **285**, 334-348, (2015).

19 Hong, W. T. *et al.* Toward the Rational Design of Non-precious Transition Metal Oxides for Oxygen Electrocatalysis. *Energy & Environmental Science* **8**, 1404-1427, (2015).

20 He, W. H., Wang, Y., Jiang, C. H., Lu, L. H. Structural Effects of a Carbon Matrix in Non-precious Metal O_2-reduction Electrocatalysts. *Chemical Society Reviews* **45**, 2396-2409, (2016).

21 Higgins, D., Zamani, P., Yu, A. P., Chen, Z. W. The Application of Graphene and its Composites in Oxygen Reduction Electrocatalysis: a Perspective and Review of Recent Progress. *Energy & Environmental Science* **9**, 357-390, (2016).

22 Xia, W., Mahmood, A., Liang, Z. B., Zou, R. Q., Guo, S. J. Earth-Abundant Nanomaterials for Oxygen Reduction. *Angewandte Chemie-International Edition* **55**, 2650-2676, (2016).

23 Daems, N., Sheng, X., Vankelecom, I. F., Pescarmona, P. P. Metal-free Doped Carbon Materials as Electrocatalysts for the Oxygen Reduction Reaction. *Journal of Materials Chemistry A* **2**, 4085-4110 (2014).

24 Li, Q., Cao, R., Cho, J., Wu, G. Nanocarbon Electrocatalysts for Oxygen Reduction in Alkaline Media for Advanced Energy Conversion and Storage. *Advanced Energy Materials* **4**, doi:10.1002/aenm.201301415, (2014).

25 Dai, L. M., Xue, Y. H., Qu, L. T., Choi, H. J., Baek, J. B. Metal-Free Catalysts for Oxygen Reduction Reaction. *Chemical Reviews* **115**, 4823-4892, (2015).

26 Hu, C. G., Dai, L. M. Carbon-Based Metal-Free Catalysts for Electrocatalysis beyond the ORR. *Angewandte Chemie-International Edition* **55**, 11736-11758, (2016).

27 Zhang, J. T., Li, H. L., Guo, P. Z., Ma, H. Y., Zhao, X. S. Rational Design of Graphitic Carbon Based Nanostructures for Advanced Electrocatalysis. *Journal of Materials Chemistry A* **4**, 8497-8511, (2016).

28 Zhou, M., Wang, H. L., Guo, S. J. Towards High-efficiency Nanoelectrocatalysts for Oxygen Reduction through Engineering Advanced Carbon Nanomaterials. *Chemical Society Reviews* **45**, 1273-1307, (2016).

29 Lefèvre, M., Proietti, E., Jaouen, F., Dodelet, J. P. Iron-based Catalysts with Improved Oxygen Reduction Activity in Polymer Electrolyte Fuel Cells. *Science* **324**, 71-74 (2009).

30 Proietti, E. *et al.* Iron-based Cathode Catalyst with Enhanced Power Density in Polymer Electrolyte Membrane Fuel Cells. *Nature Communications* **2**, 416 (2011).

31 Sa, Y. J. *et al.* A General Approach to Preferential Formation of Active Fe-N_x sites in Fe-N/C Electrocatalysts for Efficient Oxygen Reduction Reaction. *Journal of the American Chemical Society* 138, 15046-15056,(2016).

32 Wu, G., More, K. L., Johnston, C. M., Zelenay, P. High-performance Electrocatalysts for Oxygen Reduction Derived from Polyaniline, Iron, and Cobalt. *Science* **332**, 443-447 (2011).

33 Jasinski, R. A New Fuel Cell Cathode Catalyst.*Nature* **201**, 1212-1213, (1964).

34 Alt, H., Binder, H., Sandstede, G. Mechanism of the Electrocatalytic Reduction of Oxygen on Metal Chelates. *Journal of Catalysis* **28**, 8-19 (1973).

35 Scherson, D. *et al.* Cobalt Tetramethoxyphenyl Porphyrin-emission Mössbauer Spectroscopy and O_2 Reduction Electrochemical Studies. *Electrochimica Acta* **28**, 1205-1209 (1983).

36 Gupta, S., Tryk, D., Bae, I., Aldred, W., Yeager, E. Heat-treated Polyacrylonitrile-based Catalysts for Oxygen Electroreduction. *Journal of Applied Electrochemistry* **19**, 19-27 (1989).

37 Jaouen, F. *et al.* Recent advances in Non-precious Metal Catalysis for Oxygen-Reduction Reaction in Polymer Electrolyte Fuel Cells. *Energy & Environmental Science* **4**, 114-130 (2011).

38 Chen, Z., Higgins, D., Yu, A., Zhang, L., Zhang, J. A Review on Non-precious Metal Electrocatalysts for PEM Fuel Cells. *Energy & Environmental Science* **4**, 3167-3192 (2011).

39 Chung, H. T., Won, J. H., Zelenay, P. Active and Stable Carbon Nanotube/nanoparticle Composite Electrocatalyst for Oxygen Reduction. *Nature Communications* **4**, (2013).

40 Deng, D. *et al.* Iron Encapsulated within Pod-like Carbon Nanotubes for Oxygen Reduction Reaction. *Angewandte Chemie International Edition* **52**, 371-375, (2013).

41 Hu, Y. *et al.* Hollow Spheres of Iron Carbide Nanoparticles Encased in Graphitic Layers as Oxygen Reduction Catalysts. *Angewandte Chemie-International Edition* **53**, 3675-3679, (2014).

42 Hu, Y. *et al.* Direct Synthesis of Fe_3C-Functionalized Graphene by High Temperature Autoclave Pyrolysis for Oxygen Reduction. *ChemSusChem* **7**, 2099-2103 (2014).

43 Liang, J., Zhou, R. F., Chen, X. M., Tang, Y. H., Qiao, S. Z. Fe-N Decorated Hybrids of CNTs Grown on Hierarchically Porous Carbon for High-Performance Oxygen Reduction. *Advanced Materials* **26**, 6074-6079, (2014).

44 Wang, J. *et al.* Synthesis of Fe/Fe_3C Nanoparticles Encapsulated in Nitrogen-doped Carbon with Single-source Molecular Precursor for the Oxygen Reduction Reaction. *Carbon* **75**, 381-389, (2014).

45 Zhu, Y., Zhang, B., Liu, X., Wang, D. W., Su, D. S. Unravelling the Structure of Electrocatalytically Active Fe-N Complexes in Carbon for the Oxygen Reduction Reaction. *Angewandte Chemie-International Edition* **53**, 10673-10677, (2014).

46 Strickland, K. *et al.* Highly Active Oxygen Reduction Non-platinum Group Metal Electrocatalyst without Direct Metal-nitrogen Coordination. *Nature Communications* **6**, (2015).

47 Yang, W., Liu, X., Yue, X., Jia, J., Guo, S. Bamboo-like Carbon Nanotube/Fe_3C Nanoparticle Hybrids and Their Highly Efficient Catalysis for Oxygen Reduction. *Journal of the American Chemical Society* **137**, 1436-1439 (2015).

48 Wang, J. *et al.* High-density Iron Nanoparticles Encapsulated within Nitrogen-doped Carbon Nanoshell as Efficient Oxygen Electrocatalyst for Zinc–air Battery. *Nano Energy* **13**, 387-396, (2015).

49 Qiu, K. et al. Highly Efficient Oxygen Reduction Catalysts by Rational Synthesis of Nanoconfined Maghemite in a Nitrogen-Doped Graphene Framework. *ACS Catalysis* 6, 3558-3568 (2016).

50 Wei, J. *et al.* A Versatile Iron-Tannin-Framework Ink Coating Strategy to Fabricate Biomass-Derived Iron Carbide/Fe-N-Carbon Catalysts for Efficient Oxygen Reduction. *Angewandte*

Chemie **128**, 1377-1381 (2016).

51 Cui, X., Ren, P., Deng, D., Deng, J., Bao, X. Single Layer Graphene Encapsulating Non-precious Metals as High-performance Electrocatalysts for Water Oxidation. *Energy & Environmental Science* **9**, 123-129 (2016)

52 Varnell, J. A. *et al.* Identification of Carbon-encapsulated Iron Nanoparticles as Active Species in Non-precious Metal Oxygen Reduction Catalysts. *Nature Communications* **7** (2016).

53 Pol, V. G., Pol, S. V., Gedanken, A. Dry Autoclaving for the Nanofabrication of Sulfides, Selenides, Borides, Phosphides, Nitrides, Carbides, and Oxides. *Advanced Materials* **23**, 1179-1190 (2011).

54 Pol, V. G., Pol, S. V., Gedanken, A. Semiconducting, Magnetic or Superconducting Nanoparticles Encapsulated in Carbon Shells by RAPET method. *Carbon Sci. Technol* **1**, 46-56 (2008).

55 Pol, S. V., Pol, V. G., Gedanken, A. Reactions under Autogenic Pressure at Elevated Temperature (RAPET) of Various Alkoxides: Formation of Metals/Metal Oxides-Carbon Core-Shell Structures. *Chemistry-A European Journal* **10**, 4467-4473 (2004).

56 Ishihara, A., Ohgi, Y., Matsuzawa, K., Mitsushima, S., Ota, K.-I. Progress in Non-precious Metal Oxide-based Cathode for Polymer Electrolyte Fuel Cells. *Electrochimica Acta* **55**, 8005-8012 (2010).

57 Lee, K., Alonso-Vante, N., Zhang, J. J, Transition Metal Chalcogenides for Oxygen Reduction Electrocatalysts in PEM fuel cells, *Non-Noble Metal Fuel Cell Catalysts* 157-182 (2014).

58 Alonso-Vante, N. Transition Metal Chalcogenides for Oxygen Reduction, *Electrocatalysis in Fuel Cells,* 417-436 (Springer, 2013).

59 Wang, T. *et al.* Size-Dependent Enhancement of Electrocatalytic Oxygen-Reduction and Hydrogen-Evolution Performance of MoS_2 Particles. *Chemistry-A European Journal* **19**, 11939-11948 (2013).

60 Singh, K. P., Bae, E. J., Yu, J. S. Fe–P: A New Class of Electroactive Catalyst for Oxygen Reduction Reaction. *Journal of the American Chemical Society* **137**, 3165-3168 (2015).

61 Zhang, X. *et al.* Catalytically Active Single-atom Niobium in Graphitic Layers. *Nature Communications* **4**, 1924, doi:10.1038/ncomms2929 (2013).

62 Gong, K., Du, F., Xia, Z., Durstock, M., Dai, L. Nitrogen-doped Carbon Nanotube Arrays

with High Electrocatalytic Activity for Oxygen Reduction. *Science* **323**, 760-764 (2009).

63 Masa, J., Xia, W., Muhler, M., Schuhmann, W. On the Role of Metals in Nitrogen-Doped Carbon Electrocatalysts for Oxygen Reduction. *Angewandte Chemie-International Edition* **54**, 10102-10120, (2015).

64 Zhang, J., Zhao, Z., Xia, Z., Dai, L. A metal-free Bifunctional Electrocatalyst for Oxygen Reduction and Oxygen Evolution Reactions. *Nature Nanotechnology* **10**, 444-452 (2015).

65 Qu, L., Liu, Y., Baek, J.-B., Dai, L. Nitrogen-doped Graphene as Efficient Metal-free Electrocatalyst for Oxygen Reduction in Fuel Cells. *ACS Nano* **4**, 1321-1326 (2010).

66 Jin, Z. *et al.* Metal-free Selenium Doped Carbon Nanotube/graphene Networks as a Synergistically Improved Cathode Catalyst for Oxygen Reduction Reaction. *Nanoscale* **4**, 6455-6460 (2012).

67 Sheng, Z.-H., Gao, H.-L., Bao, W. J., Wang, F.-B., Xia, X. H. Synthesis of Boron Doped Graphene for Oxygen Reduction Reaction in Fuel Cells. *Journal of Materials Chemistry* **22**, 390-395 (2012).

68 Yang, Z. *et al.* Sulfur-doped Graphene as an Efficient Metal-free Cathode Catalyst for Oxygen Reduction. *ACS Nano* **6**, 205-211 (2011).

69 Yao, Z. *et al.* Catalyst-free Synthesis of Iodine-doped Graphene via a Facile Thermal Annealing Process and its use for Electrocatalytic Oxygen Reduction in an Alkaline Medium. *Chemical Communications* **48**, 1027-1029 (2012).

70 Kramm, U. I. *et al.* Structure of the Catalytic Sites in Fe/N/C-catalysts for O_2-reduction in PEM fuel cells. *Physical Chemistry Chemical Physics* **14**, 11673-11688, (2012).

71 Herranz, J. *et al.* Unveiling N-Protonation and Anion-Binding Effects on Fe/N/C Catalysts for O_2 Reduction in Proton-Exchange-Membrane Fuel Cells. *Journal of Physical Chemistry C* **115**, 16087-16097, (2011).

72 Frédéric. J Lefèvre, M , Dodelet. J-P, Cai, M. Heat-treated Fe/N/C Catalysts for O_2 Electroreduction: Are Active Sites Hosted in Micropores?. *The Journal of Physical Chemistry B* **110,** 5553-5558 (2006)

73 Szakacs, C. E., Lefevre, M., Kramm, U. I., Dodelet, J. P., Vidal, F. A Density Functional Theory Study of Catalytic Sites for Oxygen Reduction in Fe/N/C Catalysts Used in H_2/O_2 Fuel Cells. *Physical Chemistry Chemical Physics* **16**, 13654-13661, (2014).

74 Zitolo, A. *et al.* Identification of Catalytic Sites for Oxygen Reduction in Iron-and Nitrogen-doped Graphene Materials. *Nature Materials* **14**, 937-942 (2015).

75 Tylus, U. *et al.* Elucidating Oxygen Reduction Active Sites in Pyrolyzed Metal–nitrogen Coordinated Non-precious-metal Electrocatalyst Systems. *The Journal of Physical Chemistry C* **118**, 8999-9008 (2014).

76 Niu. Y. L, Huang. Y. Q, Hu. W. H, Fe_3C nanoparticle decorated Fe/N doped graphene for efficient oxygen reduction reaction electrocatalysis." Journal of Power Sources **332**, 305-311 (2016)

77 Niwa, H. *et al.* X-ray Absorption Analysis of Nitrogen Contribution to Oxygen Reduction Reaction in Carbon Alloy Cathode Catalysts for Polymer Electrolyte Fuel Cells. *Journal of Power Sources* **187**, 93-97 (2009).

78 Subramanian, N. P. *et al.* Nitrogen-modified Carbon-based Catalysts for Oxygen Reduction Reaction in Polymer Electrolyte Membrane Fuel Cells. *Journal of Power Sources* **188**, 38-44 (2009).

79 Liu, R., Wu, D., Feng, X., Müllen, K. Nitrogen-doped Ordered Mesoporous Graphitic Arrays with High Electrocatalytic Activity for Oxygen Reduction. *Angewandte Chemie* **122**, 2619-2623 (2010).

80 Rao, C. V., Cabrera, C. R., Ishikawa, Y. In Search of the Active Site in Nitrogen-doped Carbon Nanotube Electrodes for the Oxygen Reduction Reaction. *The Journal of Physical Chemistry Letters* **1**, 2622-2627 (2010).

81 Kim, H., Lee, K., Woo, S. I., Jung, Y. On the Mechanism of Enhanced Oxygen Reduction Reaction in Nitrogen-doped Graphene Nanoribbons. *Physical Chemistry Chemical Physics* **13**, 17505-17510 (2011).

82 Lai, L. *et al.* Exploration of the Active Center Structure of Nitrogen-doped Graphene-based Catalysts for Oxygen Reduction Reaction. *Energy & Environmental Science* **5**, 7936-7942 (2012).

83 Ding, W. *et al.* Space-Confinement-Induced Synthesis of Pyridinic-and Pyrrolic-Nitrogen-Doped Graphene for the Catalysis of Oxygen Reduction. *Angewandte Chemie* **125**, 11971-11975 (2013).

84 He, W., Jiang, C., Wang, J., Lu, L. High-Rate Oxygen Electroreduction over Graphitic-N Species Exposed on 3D Hierarchically Porous Nitrogen-Doped Carbons. *Angewandte Chemie International Edition* **53**, 9503-9507 (2014).

85 Liang, H.-W., Zhuang, X., Brüller, S., Feng, X., Müllen, K. Hierarchically Porous Carbons with Optimized Nitrogen Doping as Highly Active Electrocatalysts for Oxygen Reduction.

Nature Communications **5** (2014).

86 Xing, T. *et al.* Observation of Active Sites for Oxygen Reduction Reaction on Nitrogen-doped Multilayer Graphene. *ACS Nano* **8**, 6856-6862 (2014).

87 Guo, D. *et al.* Active Sites of Nitrogen-doped Carbon Materials for Oxygen Reduction Reaction Clarified using Model Catalysts. *Science* **351**, 361-365 (2016).

88 Mössbauer, R. L. Kernresonanzfluoreszenz von Gammastrahlung in Ir^{191}. *Zeitschrift für Physik* **151**, 124-143, (1958).

89 Liu, K., Rykov, A. I., Wang, J., Zhang, T. Chapter One-Recent Advances in the Application of Mössbauer Spectroscopy in Heterogeneous Catalysis. *Advances in Catalysis* **58,** 1-142 (2015).

90 Gütlich, P., Bill, E., Trautwein, A. X. Mössbauer Spectroscopy and Transition Metal Chemistry: Fundamentals and Applications. (Springer Science & Business Media, 2010).

91 Dyar, M. D., Agresti, D. G., Schaefer, M. W., Grant, C. A.,Sklute, E. C. Mössbauer Spectroscopy of Earth and Planetary Materials, *Annual Review of Earth and Planetary Sciences* **34**, 83-125 (2006).

92 Hu, Y. *et al.* Fe_3C-based Oxygen Reduction Catalysts: Synthesis, Hollow Spherical Structures and Applications in Fuel Cells. *Journal of Materials Chemistry A* **3**, 1752-1760 (2015).

93 Leonhardt, A. *et al.* Synthesis, Properties, and Applications of Ferromagnetic-Filled Carbon Nanotubes. *Chemical Vapor Deposition* **12**, 380-387 (2006).

94 Barman, B. K., Nanda, K. K. Prussian Blue as a Single Precursor for Synthesis of Fe/Fe_3C Encapsulated N-doped Graphitic Nanostructures as Bi-functional Catalysts. *Green Chemistry* 18, 427-432 (2016).

95 David, B. *et al.* Iron-Based Nanopowders Containing alpha-Fe, Fe_3C, and gamma-Fe Particles Synthesised in Microwave Torch Plasma and Investigated with Mössbauer Spectroscopy. *Japanese Journal of Applied Physics* **50**, (2011).

96 Kramm, U. I., *et al*. Effect of an ammonia treatment on structure, composition, and oxygen reduction reaction activity of Fe–N–C catalysts. *The Journal of Physical Chemistry C* **115,** 23417-23427 (2011)

97 Kramm, U. I., Lefevre, M., Larouche, N., Schmeisser, D., Dodelet, J.-P. Correlations between Mass Activity and Physicochemical Properties of Fe/N/C Catalysts for the ORR in PEM Fuel Cell via ^{57}Fe Mössbauer Spectroscopy and Other Techniques. *Journal of the*

American Chemical Society **136**, 978-985, (2014).

98 Kuhn, L. T., Bojesen, A., Timmermann, L., Nielsen, M. M., Mørup, S. Structural and Magnetic Properties of Core-shell Iron-iron Oxide Nanoparticles. *Journal of Physics-Condensed Matter* **14**, 13551-13567, (2002).

99 Scrimshire, A. *et al.* Variable Temperature ^{57}Fe Mössbauer Spectroscopy Study of Nanoparticle Iron Carbides. *Croatica Chemica Acta* **88**, (2015).

100 Kramm, U. I., et al. On an Easy Way to Prepare Metal–nitrogen Doped Carbon with Exclusive Presence of MeN_4-type Sites Active for the ORR. *Journal of the American Chemical Society* **138**, 635-640 (2016)

101 Kramm, U. I., Lefevre, M., Bogdanoff, P., Schmeisser, D., Dodelet, J. P. Analyzing Structural Changes of Fe-N-C Cathode Catalysts in PEM Fuel Cell by Mossbauer Spectroscopy of Complete Membrane Electrode Assemblies. *Journal of Physical Chemistry Letters* **5**, 3750-3756, (2014).

102 Stukan, R.A., et al.,. A Mössbauer Study of Some Ferrocene Derivatives. *Theoretical and Experimental Chemistry* **2**, 581-584 (1966).

103 Melendres, C. A. Mössbauer and Raman Spectra of Carbon-supported Iron Phthalocyanine. *The Journal of Physical Chemistry* **84**, 1936-1939 (1980).

104 Koslowski, U. I., Abs-Wurmbach, I., Fiechter, S., Bogdanoff, P. Nature of the Catalytic Centers of Porphyrin-based Electrocatalysts for the ORR: a Correlation of Kinetic Current Density with the Site Density of FeN_4 Centers. *The Journal of Physical Chemistry C* **112**, 15356-15366 (2008).

105 Kramm, U. *et al.* Influence of the Electron-density of FeN_4-centers Towards the Catalytic Activity of Pyrolyzed FeTMPPCl-based ORR-electrocatalysts. *Journal of the Electrochemical Society* **158**, B69-B78 (2011).

106 Scherson, D. A., et al. In-situ Mössbauer Spectroscopy and Electrochemical Studies of the Thermal Stability of Iron Phthalocyanine Dispersed in High Surface Area Carbon. *Journal of Electroanalytical Chemistry and Interfacial Electrochemistry* **184,** 419-426. (1985):

107 Kramm, U. I. *et al.* Structure of the Catalytic Sites in Fe/N/C-catalysts for O_2 Reduction in PEM fuel cells. *Physical Chemistry Chemical Physics* **14**, 11673-11688 (2012).

108 Borsa, D., Boerma, D. Phase Identification of Iron Nitrides and Iron Oxy-nitrides with Mössbauer Spectroscopy. *Hyperfine Interactions* **151**, 31-48 (2003).

109 Lang, G., Marshali, W. Mössbauer Effect in Some Haemoglobin Compounds. *Proceedings*

of the Physical Society **87**, 3 (1966).

110 Kurian, S., Gajbhiye, N. Magnetic and Mössbauer Study of ε-Fe_yN (2< y< 3) Nanoparticles. *Journal of Nanoparticle Research* **12**, 1197-1209 (2010).

111 Zhong, G. Y., Wang, H. J., Yu, H., Peng, F. Nitrogen Doped Carbon Nanotubes with Encapsulated Ferric Carbide as Excellent Electrocatalyst for Oxygen Reduction Reaction in Acid and Alkaline Media. *Journal of Power Sources* **286**, 495-503, (2015).

112 Zheng, X. *et al.* Podlike N-Doped Carbon Nanotubes Encapsulating FeNi Alloy Nanoparticles: High-Performance Counter Electrode Materials for Dye-Sensitized Solar Cells. *Angewandte Chemie-International Edition* **53**, 7023-7027, (2014).

113 Jiang, W. J. *et al.* Understanding the High Activity of Fe-N-C Electrocatalysts in Oxygen Reduction: Fe/Fe_3C Nanoparticles Boost the Activity of Fe-Nx. *Journal of the American Chemical Society* **138**, 3570-3578, (2016).

114 Gupta, S., Fierro, C., Yeager, E. The Effects of Cyanide on the Electrochemical Properties of Transition Metal Macrocycles for Oxygen Reduction in Alkaline Solutions. *Journal of Electroanalytical Chemistry and Interfacial Electrochemistry* **306**, 239-250 (1991).

115 Thorum, M. S., Hankett, J. M., Gewirth, A. A. Poisoning the Oxygen Reduction Reaction on Carbon-supported Fe and Cu Electrocatalysts: Evidence for Metal-centered Activity. *The Journal of Physical Chemistry Letters* **2**, 295-298 (2011).

116 Wang, Q. *et al.* Phenylenediamine-based FeN_x/C Catalyst with High Activity for Oxygen Reduction in Acid Medium and its Active-site Probing. *Journal of the American Chemical Society* **136**, 10882-10885 (2014).